UNIVERSITY OF CALIFORNIA

Los Angeles

Thermodynamic and Cost Modeling of Thermal Energy Storage Systems

Using Novel Storage Media

A dissertation submitted in partial satisfaction of the requirements for the degree Doctor of

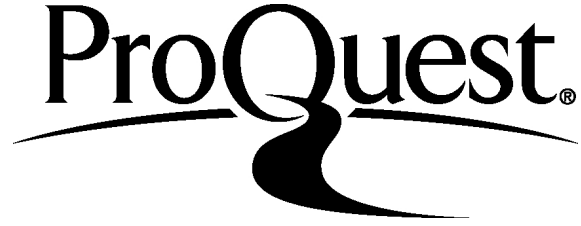Philosophy in Mechanical Engineering

by

Louis Tse

2016

ProQuest Number: 10124973

ProQuest

ProQuest 10124973

ABSTRACT OF THE DISSERTATION

Thermodynamic and Cost Modeling of Thermal Energy Storage Systems

Using Novel Storage Media

by

Louis Tse

Doctor of Philosophy in Mechanical Engineering

University of California, Los Angeles, 2016

Professor Adrienne G. Lavine, Committee Co-Chair

Professor Richard E. Wirz, Committee Co-Chair

Thermal energy storage (TES) has been widely researched across a variety of applications, and has shown promise to enable renewable energy technologies and provide the capability to shift or shave peak electricity demand. Various storage media have been successfully demonstrated for specific temperature ranges, though few candidates have been modeled for high-temperature (> 650°C) applications. The thermodynamic model and analysis described in this dissertation is aimed to contribute to this emerging knowledge base.

The numerical model investigates the transient thermodynamic and heat transfer characteristics of the TES system by coupling energy and exergy analyses with fluid property

models to calculate the spatial and temporal variations in material properties during the entire charge-discharge cycle of the TES system. Sub-models for additional system components, such as the solar field and power block in concentrating solar power (CSP) plants, are included to analyze an integrated TES system accurately. This model provides the capability to study TES design and operational parameters based upon user-defined specifications, and optimization allows the user to determine optimal plant design and dispatch control for the TES system.

The subsequent technical and economic (techno-economic) analysis considers applications, technical characteristics, market status, and recommendations for deployment of the TES system. The analysis utilizes probabilistic cost modeling to allow the user to conduct uncertainty and sensitivity analyses based upon user-specified data sets for cost indices.

Overall, the results show that it is important to consider low-cost media for future TES applications. Of the storage media evaluated, elemental sulfur showed the most promise across a wide range of operating temperatures. Some chief advantages include high thermal stability at elevated temperatures, high enthalpy of reaction, simplicity of design and operation, well-established knowledge base of handling and transportation, and low unit price. Future work is necessary to determine the material compatibility of elemental sulfur with common piping materials at high temperatures.

The dissertation of Louis Tse is approved.

Miguel A. Garcia-Garibay

Hossein Pirouz Kavehpour

Adrienne G. Lavine, Committee Co-Chair

Richard E. Wirz, Committee Co-Chair

University of California, Los Angeles

2016

iv

Dedicated to Mom and Dad.

Table of Contents

List of Figures

x

xi

List of Tables

xiv

Nomenclature

A	Helmholtz energy
A_c	Cross-sectional area
c_p	Isobaric specific heat
c_v	Isochoric specific heat
E	Energy
Ex	Exergy
FS	Safety factor
f	Fugacity
f_d	Darcy friction factor
G	Gibbs free energy
h	Heat transfer coefficient
i	Enthalpy
K	Equilibrium constant
k	Thermal conductivity
L	Length
m	Mass
M	Molar mass
n	Mole fraction
p	Partial pressure
P	Pressure

P_h	Heat transfer perimeter
Pe	Peclet number
q	Heat rate
R	Universal gas constant
r	Radius
Re	Reynolds number
S	Entropy
T	temperature
t	time
N_L	Number of tube rows
Nu	Nusselt number
u	Internal energy per unit mass
U	Internal energy
UA	Heat transfer conductance
V	Volume
W	Work
x	Axial location
Z	Compressibility factor

Acronyms

CSP	Concentrating Solar Power
DNI	Direct Normal Irradiation

xv

HTF	Heat Transfer Fluid	i	Component i
NREL	National Renewable Energy Laboratory	in	Inlet
NTU	Number of Transfer Units	out	Outlet
TES	Thermal Energy Storage	pb	Power block
		r	Reduced property

Greek Letters

		sat	Saturated state
α	Thermal diffusivity	sf	Solar field
β	Thermal expansion coefficient	$stor$	Storage
Δ	Difference between two values		
χ	Correction factor		
η	Isentropic efficiency		
ρ	Density		
ω	Acentric factor		
ψ	Exergetic efficiency		
ϕ	Fugacity coefficient		

Subscripts

0	Dead-state condition
c	Charging
cr	Critical
d	Discharging

xvi

Acknowledgments

For managing my progress, I must firstly thank the members of my Ph.D. committee (in alphabetical order).

Professor Garcia-Garibay, the care and positivity you foster with your graduate students has been a delight to observe. During my first two years, their messages of self-care were an important lesson for me to learn as I spent many nights in the laboratory running experiments until the Sun came up. I would also like to thank the Sun, although it is not on my Ph.D. committee, for being just the right distance from Earth for carbon-based life to develop.

Professor Kavehpour, your quick wit and even quicker mental access to thermodynamics has sparked many enjoyable thought experiments and conversations. I admire your brilliance as a scientist, and your firm kindness as an adviser.

Adrienne, spending the past five years under your guidance has been the happiest and most productive time of my life. It has been my greatest joy to have been under your tutelage during the long and winding road of the Ph.D. program. You have ushered in me a personal renaissance that I cannot say about many people. I only have one remaining thought: I wonder if you realize how marvelous you are (I suppose this is like saying "You, modest person; stop being so modest!). For sharing your endless humility, unwavering grace, and thought process that is equal parts silly and profound, I dedicate to you a lifetime of humble thanks.

Professor Wirz, your unquestioning trust in me as a researcher has provided me the space to grow in many directions. You actively opened opportunities for me to harness both creativity and technical knowledge to make meaningful advances in science, and to regard old problems with

a fresh, imaginative perspective. I've learned an immense amount simply by observing you manage three laboratories conducting wildly exciting research while simultaneously investing an enormous amount in all of us as emerging scientists. For all of us that benefitted from your passion, intelligence, management, and patience; thank you for everything. Speaking of which, I give sincere gratitude to my labmates for their good company throughout the graduate years and for future years to come.

To my NREL family, your unconditional kindness to this random Ph.D. student is a lasting memory I will not easily forget. To my Bruin Shelter family, I am astounded by the tremendously purposeful village we have built in less than one year. I express gratitude to the Inner Circle for believing in me when no one else would. Directors, you inspire me on a daily basis and it is a privilege to build alongside you something truly meaningful for our community, city, nation, and most importantly, for our residents. I'll see you during overnight shifts.

To my friends, I would like your reading of my acknowledgments to be different from the typical experience, where you frantically flip to and scour the few pages to determine if your name is mentioned, victorious or crestfallen over a matter of my own space, time and memory constraints that, in all truth, speaks nothing to our friendship. If you are taking the care to read this, you can rest assured that the following message is intended for you. I cannot be more grateful that you entrust your friendship with me; you have charmed me in a way that only you are capable of. If you wish, I am more than happy to expand in more detail all the wonderful things that you are, if you can sit for a coffee with me. Thank you for listening patiently, adventuring courageously, advising open-mindedly, laughing noisily, and bonding intentionally with me. You are diamonds, all of you, and I am glad we get to do life together.

And finally, I arrive at my family. Words are a difficult medium of expression for me to precisely articulate my sentiments about you. Without you, I would not be here, writing all of these words.

Vita

2016   UCLA Engineering Achievement Award for Student Welfare

2016   UCLA Edward A. Bouchet Graduate Honor Society

2015   Co-founder, Bruin Shelter

2015   Best Student Paper, Energy Sustainability Conference 2015 (American Society of Mechanical Engineers)

2015   Visiting Researcher, National Renewable Energy Laboratory

2015   UCLA Graduate Students Association Jeffrey L. Hanson Distinguished Service Award

2014   Adjunct Staff, RAND Corporation

2014   M.S., Mechanical Engineering, UCLA

2014   Department of Energy, ARPA-e Student Program (invited conference presentation)

2012   National Science Foundation Graduate Research Fellowship

2011   UCLA Mechanical and Aerospace Engineering Departmental Fellowship

2011   B.S., summa cum laude, Mechanical Engineering, Arizona State University

2010   Edson Student Entrepreneurship Initiative Award Winner, Arizona State University

2010   Undergraduate Teaching Assistant, Finite Element Analysis II, Arizona State University

2010   President, American Society of Mechanical Engineers, Arizona State University

2008   Undergraduate Researcher, Center for Environmental Fluid Dynamics, Arizona State University

Publications

Tse, L. A., Lavine, A. S., Lakeh, R. B., and Wirz, R. E., 2015, "Exergetic optimization and performance evaluation of multi-phase thermal energy storage systems," Solar Energy, 122, pp. 396-408.

Tse, L.A., and Oluwatola, O., 2014, "Evaluating renewable energy technology transfer in developing countries: enabling factors and barriers," Science Policy and Governance, Vol. 6.

Tse, L.A., Ganapathi, G. B., Wirz, R. E., and Lavine, A. S., 2014, "Spatial and temporal modeling of sub- and supercritical thermal energy storage," Solar Energy, 103(0), pp. 402-410.

Tse, L.A., and Neises, T.W., 2015, "Analysis and optimization for off-design performance of the recompression s-CO2 cycles for high-temperature CSP applications." Supercritical CO2 Power Cycle Symposium, San Antonio TX.

Tse, L.A., Wirz, R. E., and Lavine, A. S., "Optimal Operation Strategies For Thermal Energy Storage Systems In Solar Thermal Power Plants," Proc. ASME 2015 9th International Conference on Energy Sustainability collocated with the ASME 2015 13th International Conference on Fuel Cell Science, Engineering and Technology, American Society of Mechanical Engineers.

Tse, L.A., Lakeh, R. B., Wirz, R. E., and Lavine, A. S., "Exergy-Based Optimization of Sub-and Supercritical Thermal Energy Storage Systems," Proc. ASME 2014 8th International Conference on Energy Sustainability collocated with the ASME 2014 12th International Conference on Fuel Cell Science, Engineering and Technology, American Society of Mechanical Engineers.

Huang, H. P., Hunt, J., Sharma, A., **Tse, L.A.,** Fernando, H., Gunawan, A., and Thompson, M., 2011, "Axially asymmetric rotating tank experiments for thermally forced stationary waves in geophysical fluids." In APS Division of Fluid Dynamics Meeting Abstracts (Vol. 1).

Chapter 1

Introduction

1.1 Motivation

The Department of Energy has supported the advancement of thermal energy storage (TES) to efficiently balance energy demand and to provide baseload power by reducing the mismatch between thermal energy demand and supply. The improvement of TES systems has also led to the extended utilization of renewable energy sources (e.g. solar and wind), which accommodates short-term intermittency and increases dispatchability by offsetting peak energy costs. This paper addresses a proposed single-tank TES system utilizing fluids in their two-phase (liquid-vapor) to supercritical states. In particular, it explores the behavior and optimization of such a system during the discharge cycle of a CSP plant, when the storage fluid provides thermal energy to the steam generator.

This chapter describes the development of a thermodynamic model of a TES system capable of evaluating the temperature of the TES tank and HTF mass flow rate during the charging and discharging periods, when energy is stored and retrieved, respectively. The transient nature of the system, along with the spatial variation of temperature within the tank, is governed by the mass and energy balances within the TES tank and HTF loop, which are detailed in this chapter. The capability of the plant designer to analyze overall performance for specific design and operating parameters is particularly valuable given the wide range of inputs that can be studied.

www.manaraa.com

1.2 Current Status of Thermal Energy Storage

Thermal energy storage can generally be classified as one of three types: (1) sensible heat storage, usually using solid or liquid storage media, (2) latent heat storage, typically employing PCM storage media to store energy in the constant-temperature transition from one phase to another, and (3) thermochemical storage, which uses chemical reactions to store energy in the endothermic bond-breaking process. Figure 1 shows the thermodynamic process of storing and releasing energy for each category.
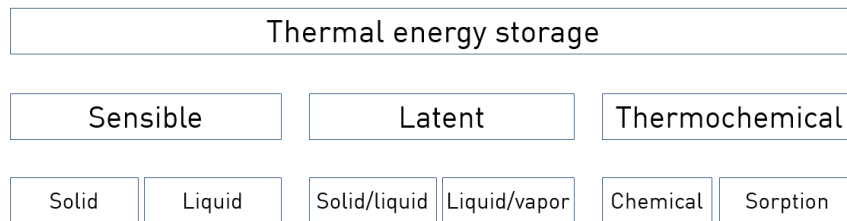
Figure 1: Broad classification of thermal energy storage media.

Due to the highly diverse TES materials and technologies that have been researched, it is not practical to define a set of global metrics to evaluate each system. Still, to understand the challenges facing TES systems, it is helpful to define common guidelines for evaluating TES systems. The main characteristics include:

- High thermal stability at the desired temperature range

- Low vapor pressure

- High specific heat and volumetric energy density

2

- Material compatibility with containment material over high number of cycles

- Minimal side reactions and byproducts, and high enthalpy of reaction and percentage yield (for TCES technologies)

- Low-cost and readily available storage media

- Integration with entire system

The general characteristics of each TES technology are provided in Table 1.

Table 1: Characteristics of thermal energy storage technologies [1].

	Sensible	**Latent**	**Thermochemical**
Volumetric energy density	~50 – 100 kWh/m^3	~ 100 – 300 kWh/m^3 of material	~ 500 – 750 kWh/m^3 of reactants
Gravimetric energy density	~0.02 – 0.03 kWh/kg of material	~0.05 – 0.1 kWh/kg of material	~0.5 – 1.0 kWh/kg of reactants
Vapor pressure	Low	Low	Low to high
Storage period	Days (thermal losses)	Days (thermal losses)	Theoretically unlimited
System complexity	Low	Medium	High
Technology maturity	Commercial	Pilot	Laboratory

Another important aspect of the TES system is the ability to operate on the timescale needed for specific applications, which encompasses both storage fluid properties and design configuration of the TES tank. Start-up times, ramp rates, and other state-dependent characteristics can be imperative to enabling TES to provide value for applications such as ancillary services to grid-connected systems, quenching processes, and combined heat and power [2-4]. Figure 2 illustrates

3

the basic operation of sensible, latent, and thermochemical storage during the charging and discharging processes.

(a)   (b)
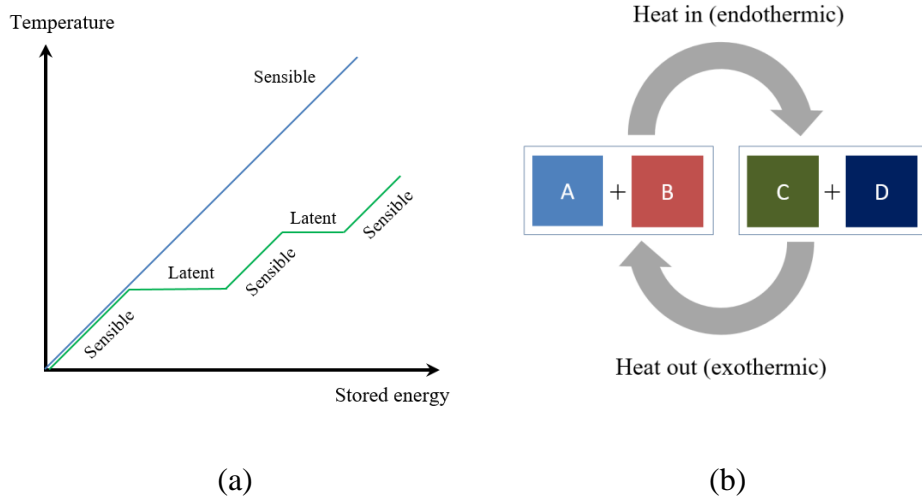
Figure 2: a) Sensible heat storage involves heating the storage fluid at single-phase, and latent heat storage utilizes the constant-temperature process of melting or vaporization. b) Thermochemical energy storage relies on altering the chemical potential of the system to store or release heat.

For TES systems, it is also imperative to maximize first- and second-law efficiency by retrieving as much energy as possible, and of the highest quality. Exergetic efficiency is a standard metric to evaluate performance of a TES system, and is defined as the ratio of the Gibbs free energy extracted during discharging, to the Gibbs free energy stored during charging. It can be expressed as:

4

$$\psi = \frac{|\Delta G_d|}{|\Delta G_c|} = \frac{\left|\left(\Delta H - T_0 \Delta S\right)_d\right|}{\left|\left(\Delta H - T_0 \Delta S\right)_c\right|} \tag{1.1}$$

Numerous reviews illustrate the value of TES systems across many energy applications and temperature ranges, including power generation, waste heat recovery, industrial applications, energy efficiency in buildings and districts, seasonal storage, among a variety of others [5-9]. Advancements in TES technology have observed considerable achievements; however, the lack of low-cost, thermally stable materials has been the common challenge across all TES technologies.

Sensible thermal energy storage (STES): This is the most common form of TES due to its simplicity. The amount of energy stored in a sensible thermal energy media is proportional to the change in temperature of the material. STES materials have been investigated for many different configurations, such as two-tank, thermocline, packed bed, and solid-state systems. In addition to the general challenges of corrosion and mechanical strength that all TES systems face, specific challenges for each configuration have been reported.

In the two-tank STES system, one tank stores the material at the designated hot temperature, and the second tank stores the material at a lower temperature after energy has been extracted. Two-tank systems are classified as either direct or indirect approaches. In direct systems, the storage fluid also acts as the HTF while for indirect systems, the storage fluid and HTF are different. The two-tank indirect configuration is the most commercially developed configuration for concentrating solar power (CSP) applications, which typically use oils or salts. The present challenge is the selection of the storage media itself. Currently used materials have limitations such as limited thermal stability at temperatures of interest, barring their ability to be integrated

5

with high-temperature power cycles or processes, or the materials have high melting points, requiring freeze protection systems to prevent solidification of the material in the piping during transport. Additionally, STES systems currently use materials with relatively high cost and would benefit from lower cost options.

Thermocline systems use a single tank and rely upon the density difference of a single fluid at hot and cold temperatures to create thermal stratification in the tank. The foremost challenge of thermocline systems is maintaining thermal stratification. Typically, there is no physical separation of the hot and cold fluid, and there exists a temperature gradient across the volume. Subsequently, heat flows from the hot section of the tank to the cold section, which degrades the quality of the energy within the system. Materials used for sensible storage systems are shown in Table 2.

Table 2: Characteristics of select published sensible storage fluids [5-7, 9, 10].

T_{cold} (°C)	T_{hot} (°C)	Material	Thermal conductivity (W/mK)	Density (kg/m^3)	Average specific heat capacity (kJ/kgK)	Volumetric specific heat capacity (kWht/m^3)	Type of medium
200	300	Sand-rock-oil	1	1700	1.3	60	Solid
200	400	Reinforced concrete	1.5	2200	0.85	100	Solid
200	400	Cast iron	37	7200	0.56	160	Solid
200	500	NaCl	7	2160	0.85	150	Solid
200	700	Cast steel	40	7800	0.6	450	Solid
200	700	Silica fire bricks	1.5	1820	1	150	Solid
200	1200	Magnesia fire bricks	5	3000	1.15	600	Solid

6

250	350	Synthetic oil	0.11	900	2.3	57	Liquid
250	450	Nitrite salts	0.57	1825	1.5	152	Liquid
270	530	Liquid sodium	71	853	1.3	80	Liquid
300	400	Silicone oil	0.1	900	2.1	52	Liquid
180	1300	Lithium liquid salt	38.1	510	4.19	-	Liquid
15	400	Dowtherm A	0.1171	867	2.2	-	Liquid
0	345	Therminol 66	-	750	2.1	-	Liquid

Efforts to mitigate this issue have been proposed to minimize diffusion of the thermocline. One of the proposed solutions is "active thermocline management", which draws HTF near the thermocline gradient, rather than the top or bottom of the tank [11]. An alternative solution is the installation of a floating, porous barrier with low thermal conductivity that is freely moving in order to maintain separation of the hot and cold fluids [12].

7

(a)
(b)
(c)
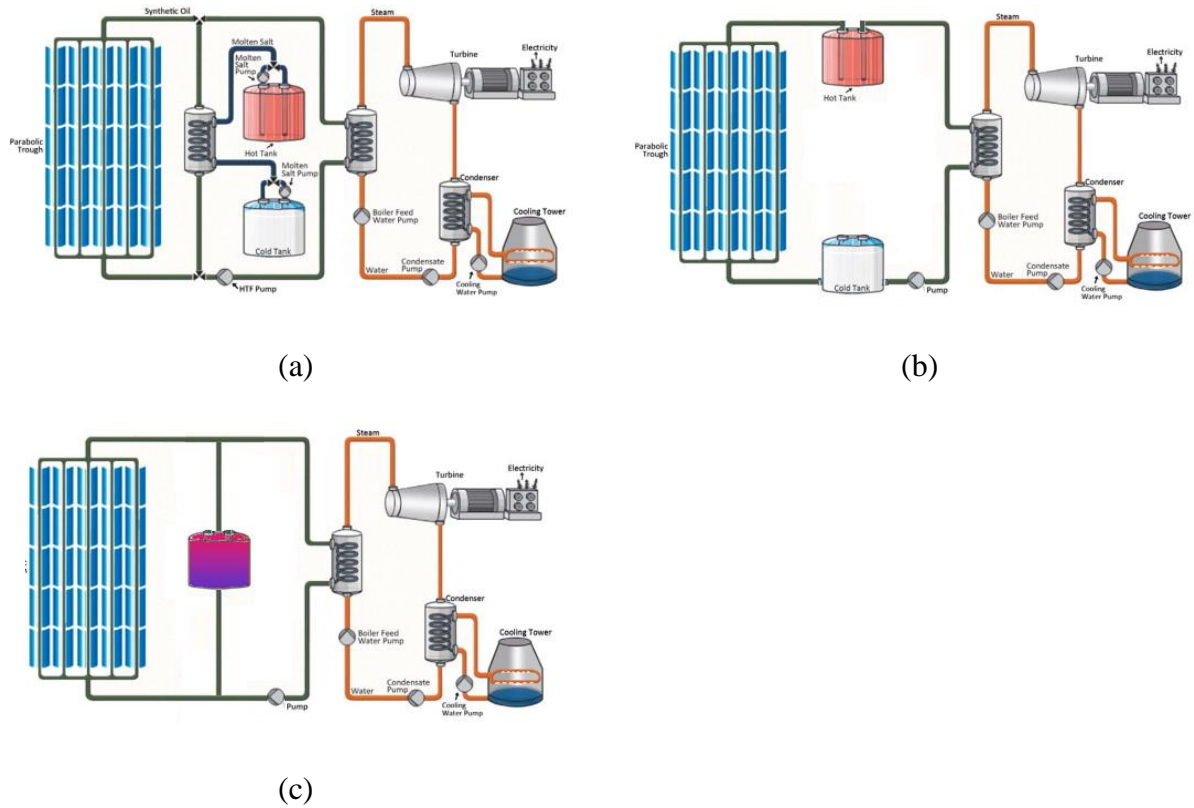
Figure 3: Schematic of a parabolic trough CSP plant with a) an indirect two-tank TES system, b) a direct two-tank TES system, and c) a thermocline TES system (adapted from source: CSP World) .

Latent heat thermal energy storage (LHTES): The storage of thermal energy by utilizing a material's heat of fusion, and to a lesser extent heat of vaporization, has been comprehensively studied and there are a handful of review articles on the topic [9, 13-19]. These materials are usually referred to as phase change materials (PCMs) because of the change in physical state they undergo.

8

Due to the challenges of storing gas, solid-to-liquid transitions are most commonly investigated. However, one of the primary challenges of PCMs is the poor thermal conductivity and subsequent heat transfer out of the system. During charging, the PCM quickly melts into a liquid layer at the interface, and convective currents enhance heat transfer throughout the PCM. In contrast, when discharging from the PCM tank, the PCM quickly forms a solid layer at the interface, which typically has a substantially lower heat transfer coefficient [20]. Therefore, heat transfer out of the system is comparatively slower. Numerous solutions have been proposed to overcome the issue regarding poor heat transfer out of the PCM system, including embedded heat pipes or thermosyphons into the PCM tank, inserting metallic matrices or flakes, or adding extended surfaces to the heat exchanger [21].

Another challenge associated with PCM systems is relatively low exergetic efficiency. Because heat storage and release by a PCM is isothermal at the material's melting point, a system employing a single PCM can only operate at the melting temperature of that PCM. However, this is not likely to coincide with the application, such as a power cycle or industrial process. Should the PCM melting temperature exceed the design-point power cycle temperature, then the PCM system will have poor exergetic efficiency. Conversely, if the PCM selected has a melting temperature lower than the desired operating temperature, the PCM cannot provide sufficient energy and the application will suffer from lower efficiency. A proposed solution to this challenge is to employ multiple PCMs with different melting temperatures in a cascaded configuration [22]. From a practical standpoint, most industrially relevant configurations employ three or four PCMs [23], based on the techno-economic consideration of balancing the increased efficiency of the TES

9

system using more PCMs with the increased cost associated with the need for a separate tank for each PCM used. Table 3 shows the properties of some latent heat storage fluids.

Table 3: Characteristics of select published latent storage fluids [9, 13, 21]

T_{melt}(°C)	Material	Latent heat of fusion (J/g)	Thermal conductivity (W/mK)
307	$NaNO_3$	177	0.5
318	77.2 mol% NaOH-16.2% NaCl-6.6% Na_2CO_3	290	-
320	54.2 mol% LiCl-6.4% $BaCl_2$-39.4% KCl	170	-
335	KNO_3	88	0.5
340	52 wt% Zn-48% Mg	180	-

Thermochemical energy storage (TCES): Thermochemical energy storage uses thermal energy to alter the chemical composition of the initial storage fluids, and store energy in chemical potential of a particular reaction. As shown in Table 1, the energy density of a thermochemical storage fluid can be up to an order of magnitude greater than the energy density of TES materials based upon sensible or latent heat approaches. One of the proposed chief advantages of thermochemical storage is the potential for the chemical components of the reaction to be stored at ambient temperature, thereby reducing thermal losses.

Some of the major techno-economic challenges associated with TCES relate to the fact that these systems typically either require or generate a gas as one component of the chemical reaction. At the operating temperatures of these systems, the gases can be very corrosive and are under very high pressures. This combination of corrosiveness and high pressure requires substantial amounts of expensive high-temperature alloys to build containment vessels. Yet another drawback to

10

pressurized gas systems is that substantial amounts of energy are required to compress these gasses. Other challenges include cycling longevity, catalyst life, reversibility of the reaction, and potentially prohibitive reaction kinetics. Materials that are proposed for thermochemical storage are presented in Table 4.

Table 4: Characteristics of select published thermochemical energy storage reactions [1, 24-26].

Compound	Temperature (°C)	Reaction	Enthalpy of reaction (kJ/mol)
Manganese oxide	530 (at 1 bar of reactant)	$MnO_2 + \Delta H \leftrightarrow 0.5Mn_2O_3 + 0.25O_2$	42
Calcium hydroxide	505 (at 1 bar of reactant)	$Ca(OH)_2 + \Delta H \leftrightarrow CaO + H_2O$	112
Calcium carbonate	896 (at 1 bar of reactant)	$CaCO_3 + \Delta H \leftrightarrow CaO + CO_2$	167
Magnesium hydride	250-500	$MgH_2 + \Delta H \leftrightarrow Mg + H_2$	75
Ammonia	400-500	$NH_3 + \Delta H \leftrightarrow \frac{1}{2}N_2 + \frac{3}{2}H_2$	67

1.3 Dissertation Overview

The primary objectives of the research presented in this dissertation are the following: (1) develop a thermodynamic model based upon first principles to accurately predict transient behavior and performance of the TES systems under study (Chapters 2 & 3); (2) determine optimal plant design using objective functions such as net annual electricity production, net thermal-to-electric efficiency, exergetic efficiency, among others (Chapter 4); and (3) evaluate techno-economic analyses to assess long-term cost effectiveness utilizing both statistical and optimization methods (Chapter 5).

11

Another key component of this dissertation is the design and optimization of the TES systems under study. The parameter space is a combination of thermophysical properties, design parameters, and operating strategies; for instance, thermal conductivity of the storage fluid, tank geometry, and maximum operating temperature all affect the dynamics of heat transfer. An overview of the parameters under investigation is given in Chapter 3.

A tertiary objective of this research is to analyze TES in various applications and integrated with various technologies, such as the supercritical carbon dioxide (s-CO_2) Brayton cycle, CSP technologies (Linear Fresnel, parabolic trough, and power tower), and combined heat and power applications. This requires development of models specific to each technology, or utilization of simplified regression models. Through technical and economic (techno-economic) analysis, the complex challenges associated with the cost-effectiveness of TES are presented. The results of this section aim to bridge the gap between technical advancements and economic considerations to develop future TES technologies and highlight opportunities for researchers pursuing solutions for cost-effective TES systems.

12
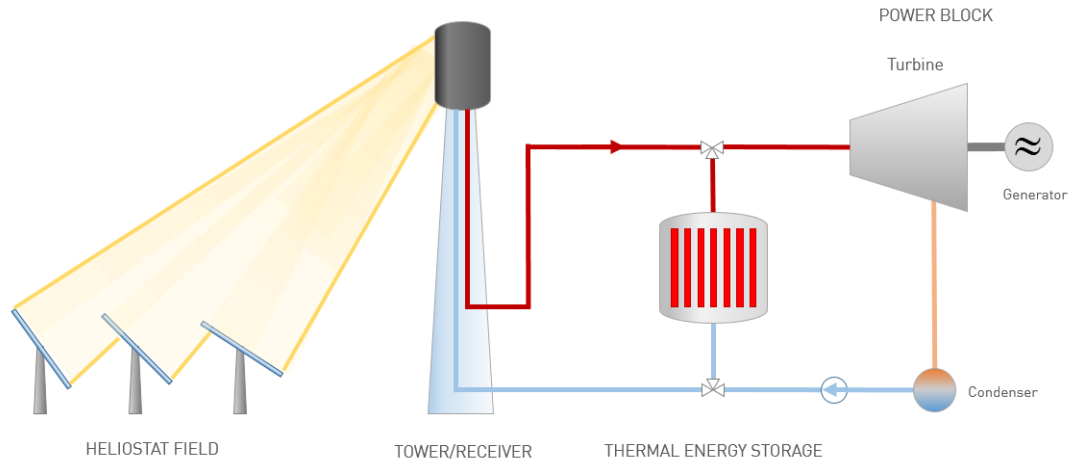
Figure 4: Basic components of a CSP plant, specifically a power tower system.

Review of TES storage fluid modeling

In order to develop design tools to simulate performance of TES systems, relevant information about the storage fluid properties must be gathered. Due to the diversity of TES technologies that exist, a wide variety of modeling methodologies have been reviewed to predict the behavior of the storage fluid, including though not limited to Boussinesq approximations, enthalpy-porosity techniques, regression fits to experimentally measured data, equations of state, fundamental thermodynamic relations, or a combination thereof [5, 7].

Well-established TES modeling tools include System Advisor Model developed by the National Renewable Energy Laboratory [27], TRNSYS developed by University of Wisconsin, Madison [28], Thermoflow [29], and numerous specialized codes developed for specific TES

13

materials and systems implemented across a range of platforms, such as Fortran, Fluent, Engineering Equation Solver, to name a few.

The general design of the TES system investigated in this research is as follows: the storage fluid is encapsulated in tubes arranged in a shell-tube single tank system, and heat is absorbed and released indirectly using an HTF. A basic diagram of the TES system integrated into a CSP power tower plant is shown in Figure 4. The potential benefits of a single tank system include lower capital costs by requiring construction of one tank instead of two, simplified HTF piping, elimination of an external heat exchanger, and smaller tank footprint. Still, there are drawbacks to this design; the most prominent one is the thermal stratification that must be maintained. The TES system must be designed to achieve sharp thermal stratification; otherwise, mixing causes the temperature of the HTF flowing to the power cycle will be reduced and axial conduction can exacerbate this issue.

The storage tubes are loaded with a certain fixed mass of the storage fluid. Since their volume remains constant, the average density, or *loading*, ρ also remains constant. Thus, both the charging and discharging processes follow an isochoric (i.e. constant specific volume) line on a *P-v* diagram, as shown in Figure 5. The discharge process begins at an initial state corresponding to high temperature, pressure, and internal energy, and ends at a state at lower temperature, pressure, and internal energy. At any instant in time, the internal energy and density can be related to the storage fluid temperature and pressure:

14

$$u_{stor} = u\left(T_{stor}, P_{stor}\right) \tag{1.2}$$

$$\rho_{stor} = \rho\left(T_{stor}, P_{stor}\right) \tag{1.3}$$

Thus with fixed density, if the storage fluid temperature is known, its pressure can be determined from Eq. (1.3) and its internal energy can then be determined from Eq. (1.2).
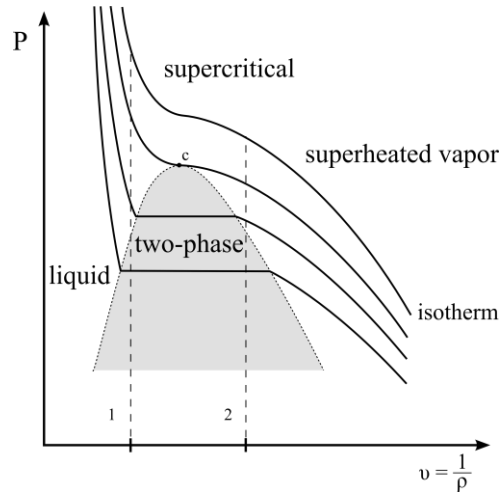
Figure 5: *P-v* diagram showing vertical lines of constant average fluid density.

Chapter 2 describes the various methodologies for evaluating fluid properties with greatly varying molecular structure and chemistry. Chapter 3 contains a review of the overall system under study, and the thermodynamic modeling approaches of the TES system. Chapter 4 presents an exergy analysis and optimization of design and operating parameters of the TES system and other CSP plant components to minimize the levelized cost of electricity. Chapter 5 discusses the statistical analysis of the combined technical and economic (techno-economic) evaluation of the TES system to assess economic feasibility and the pathway to commercialization. Conclusions and

15

recommendations for future work resulting from the research presented in this dissertation are summarized in Chapter 6.

Chapter 2

Thermodynamic Property Modeling

Thermodynamic property modeling has historically served as a necessary tool for a wide range of applications. With the advent of advanced materials, modern technologies depend more than ever upon accurate property modeling. This chapter reviews well-established methodologies for evaluating thermodynamic properties, and expands upon the existing models applied to TES systems. The description of existing methodologies aims to discuss governing concepts, current status and constraints of current property models, and the interaction between experimental data and theoretical models.

As described in the previous chapter, the governing principles of heat and mass transfer, fluid flow, and thermodynamics direct the behavior of the TES system integrated with CSP applications. In this chapter, we investigate in further detail the thermophysical properties of the modeled storage fluid, which become particularly important when investigating multiple candidates. In TES literature, many studies utilize experimental data of thermal properties as a function of temperature. In the absence of a range of experimental data, some studies invoke the assumption of constant properties, or an effective value averaged across a temperature range.

In this chapter, the methodology for obtaining thermodynamic properties of the possible storage fluids is outlined. Specifically, an equation of state is utilized to evaluate fluid properties for a given set of operating conditions (i.e. temperature, density, pressure). The objective includes fundamental calculation of vapor pressure, internal energy, and departure from ideal gas state, to name a few. This is combined with experimental data from well-established sources such as the

Design Institute for Physical Properties (DIPPR) 801 Database [30], and the National Institute of Standards and Technology (NIST) Chemistry Webbook, the latter of which aggregates thermophysical property data from various peer-reviewed journal articles.

Figure 6 shows the general structure of the fluid property program library. The program structure is easily modified to include other equations of state, additional experimental data, and even other fluid property modeling techniques.
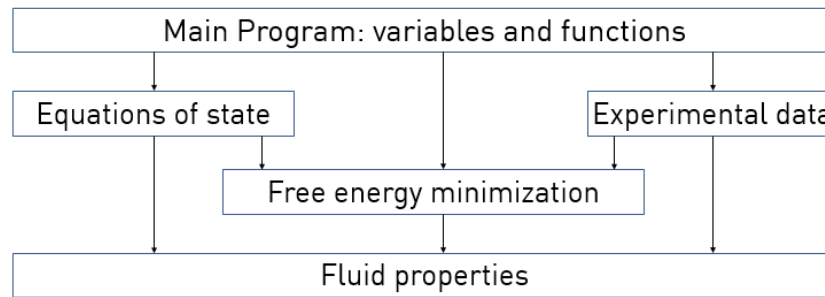
Figure 6: General structure of the fluid property program library, which can evaluate fluid properties using different methods based upon the thermodynamic state of the storage fluid.

The program enables the user to select different equations of state (EOS), experimental datasets, or thermodynamic models. The advantage of EOSs lies in that they are computationally expedient, and have high accuracy under certain conditions. For example, the Peng-Robinson EOS requires the critical temperature, critical pressure, and acentric factor and is well-suited for non-polar molecules, while the Soave-Redlich-Kwong EOS is useful for modeling hydrocarbons. The limitations of each individual EOS are highlighted as a note to the user. Additionally, the user can choose experimental datasets in the form of lookup tables, which can be selected from a stored database or entered by the user. Benefits of this method include the use of known measurements;

18

similarly, the drawback of using purely empirical models is that they can only be applied to the restricted data measured. Finally, a free energy minimization thermodynamic model can also be chosen, which is used specifically for evaluating properties of elemental sulfur. This approach enables theoretical calculation of fluid properties with high accuracy and does not have as many limitations as other models such as EOSs. However, the challenge is that it requires substantially more computing resources and may not lead to a numerically stable solution.

2.1 Supercritical Fluids

A supercritical fluid is any substance exceeding its critical temperature and pressure, when the distinction between liquid and gas phases disappears and the fluid properties of both phases combine in an intriguing fashion. Close to the critical point, small deviations in pressure or temperature result in large changes in density, enabling many supercritical fluid properties to be finely tuned for a specific need. Supercritical fluids have been developed for extraction of solids, fractionation, chromatography, particle design, and other industrial and laboratory processes [31]. The use of supercritical fluids for TES applications has been proposed [32] to take advantage of the unusual fluid properties and the combination of sensible and latent heat in the two-phase as well as the supercritical state. As an example, the isochoric specific heat of water is shown in Figure 7.

19
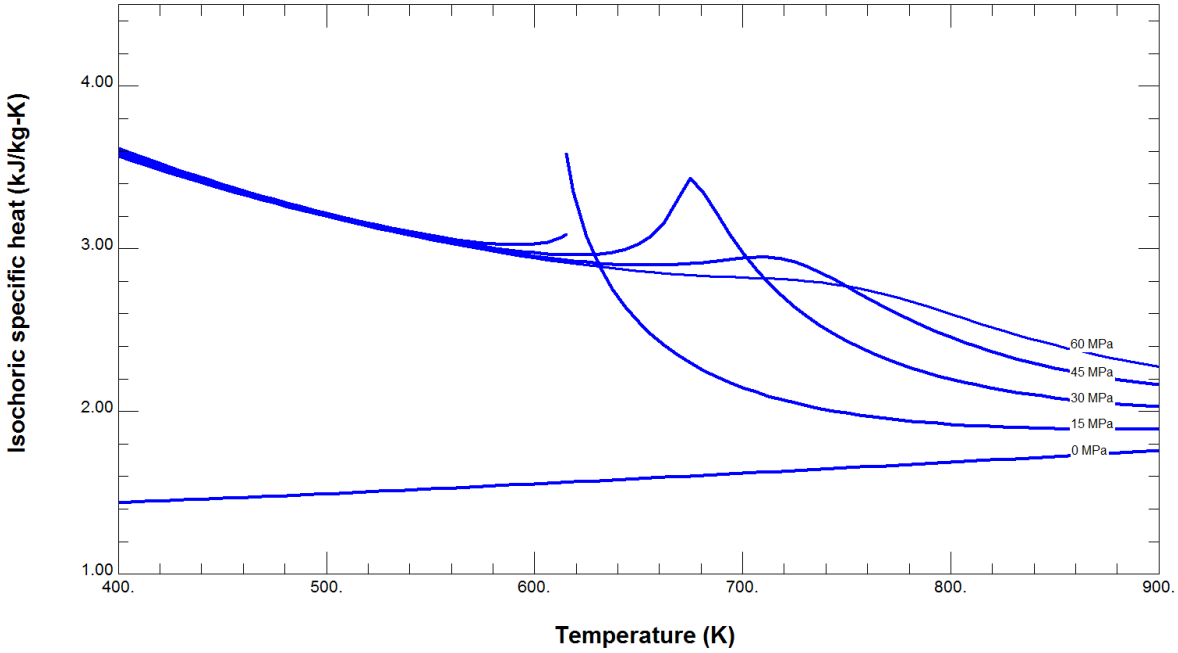
Figure 7: Isochoric specific heat of water, which has a critical temperature of 647 K and critical pressure of 22 MPa.

In addition, another cited feature is the high compressibility of the fluid in the supercritical state, which can enable high volumetric storage density. The challenge is the elevated pressure of the supercritical pressure. A rigorous fluid selection process of 400 organic fluids aims to determine a fluid candidate that exhibits high heat of vaporization, high boiling point and critical temperature, and low cost.

Section 2.1 describes the modeling process of organic fluids for any thermodynamic conditions of interest, particularly for operating temperature ranges of CSP plants. This is primarily achieved through the use of equations of state (Subsection 2.1.1) and property libraries (Section 2.3).

20

2.1.1 Equation of State

An equation of state is a mathematical formula describing the relationship between various intensive properties of a system, such as temperature, pressure, volume, and internal energy. Equations of state are useful tools to determine the properties of fluids, mixtures, and gases. The most well-known EOS is the ideal gas law, which is acceptable for low pressures and moderate temperatures, and specifically for weakly polar gases. Other equations of state have been developed to predict different ranges of temperatures and pressures, substances, and particular phenomena such as condensation. J.D. van der Waals developed the first EOS which utilizes ideal gas law and assumes a finite volume for a given molecular size [33]. His formula was a breakthrough in the development of EOSs; other major equations of state include the Redlich-Kwong equation of state [34]and the Soave modification to the Redlich-Kwong equation of state [35]. Presently, there is no single EOS that accurately predicts the properties of all substance for all conditions. Equations of state typically utilize the corresponding state, or reduced variables defined as:

$$T_r = \frac{T}{T_{cr}} \tag{2.0}$$

$$P_r = \frac{P}{P_{cr}} \tag{2.1}$$

The Redlich-Kwong EOS can adequately predict thermophysical properties given $P_r < 0.5 T_r$. It is superior to the van der Waals EOS, but does not perform well regarding the liquid phase and should not be used to accurately calculate liquid-vapor equilibria.

21

In the application of TES modeling, an EOS can provide utility of determining the transient state of the HTF and storage fluid as they undergo charging and discharging. In particular, the widely used assumption of a constant specific heat – temporally and spatially – is not necessary, and instead can be calculated from its thermodynamic definition.

Peng and Robinson developed a cubic equation of state [36] (herein referred to as PR-EOS) that is highly accurate at predicting thermodynamic properties of fluids that are characterized within a specific range of polarity. This is quantified by the acentric factor, ω, which was first introduced by Pitzer [37] and describes the degree of non-sphericity (or the centricity) of the given molecule. Also, in similar fashion to the Soave-Redlich-Kwong equation, a function α is developed as a curve fit to vapor pressure data of hydrocarbons. Solving for pressure, the generalized PR-EOS can then be written as

$$P = \frac{RT}{V_m - b} - \frac{a\alpha}{V_m^2 + 2bV_m - b^2} \tag{2.2}$$

where V_m is the molar volume, and the other parameters are defined by a general curve fit and are as follows:

$$a = \frac{0.457235R^2T_{cr}^2}{P_{cr}} \tag{2.3}$$

$$b = \frac{0.077796RT_{cr}}{P_{cr}} \tag{2.4}$$

$$\alpha = \left(1 + \kappa\left(1 - T_r^{0.5}\right)\right)^2 \tag{2.5}$$

$$\kappa = 0.37464 + 1.54226\omega - 0.26992\omega^2 \tag{2.6}$$

where ω is the acentric factor of the storage fluid, R is the universal gas constant, and Z is the compressibility factor.

22

$$A = \frac{a\alpha P}{(RT)^2} \tag{2.7}$$

$$B = \frac{bP}{RT} \tag{2.8}$$

Then, we define compressibility factor as

$$Z = \frac{PV}{RT} \tag{2.9}$$

In thermodynamics, the significance of compressibility is to evaluate the deviance of the real gas from the "ideal gas" state. Therefore, Eq. (2.2) can be written in polynomial form using compressibility factor:

$$Z^3 - (1-B)Z^2 + (A - 2B - 3B^2)Z - (ZB - B^2 - B^3) = 0 \tag{2.10}$$

The methodology of determining the deviance of the real gas from the "ideal gas" state using the compressibility factor will be used more extensively in evaluating enthalpy; this is described in a later section in the chapter.

However, in order to know the state of the storage fluid (solid, liquid, liquid-vapor mixture, vapor, or supercritical), the saturation pressure must be known. As mentioned previously, K.S. Pitzer [37] first introduced the acentric factor, which is calculated by

$$\omega = -\log_{10}(P_{r,sat}) - 1, \quad \text{at } T_r = 0.07 \tag{2.11}$$

Additionally, Pitzer developed a methodology to model ion interactions, and to determine saturation pressure of any fluid based on ion interaction and correlations with experimental data. The Pitzer relation for the reduced saturation pressure is denoted as

23

$$P_{r,sat} = e^{f_0 + \omega f_1} \tag{2.12}$$

where the coefficients f_0 and f_1 are functions of reduced temperature and given by the Lee-Kesler equation:

$$f_0 = 5.92714 - \frac{6.09648}{T_r} - 1.28862 \log(T_r) + 0.169347 T_r^6 \tag{2.13}$$

$$f_1 = 15.2518 - \frac{15.6875}{T_r} - 13.4721 \log(T_r) + 0.43577 T_r^6 \tag{2.14}$$

Thus, we introduce the fugacity coefficient, defined as

$$\phi = f/P \tag{2.15}$$

The concept of fugacity was first introduced by Lewis [38], and is likened to the thermodynamic activity of a gas. Thermodynamically, fugacity is related to compressibility: the fugacity is the pressure of an ideal gas with the same chemical potential as a real gas. Therefore, in essence, the fugacity coefficient is a correction to the actual pressure, P.

2.1.2 Departure Functions

It can be seen from previous sections that the importance of how a fluid deviates from ideal gas behavior is critical to analyzing its thermodynamic properties, such as enthalpy, entropy, and internal energy. This deviation is illustrated in Figure 8. Departure functions provide this capability, and are used to calculate properties of a real gas, namely how much it deviates from the ideal state.

24
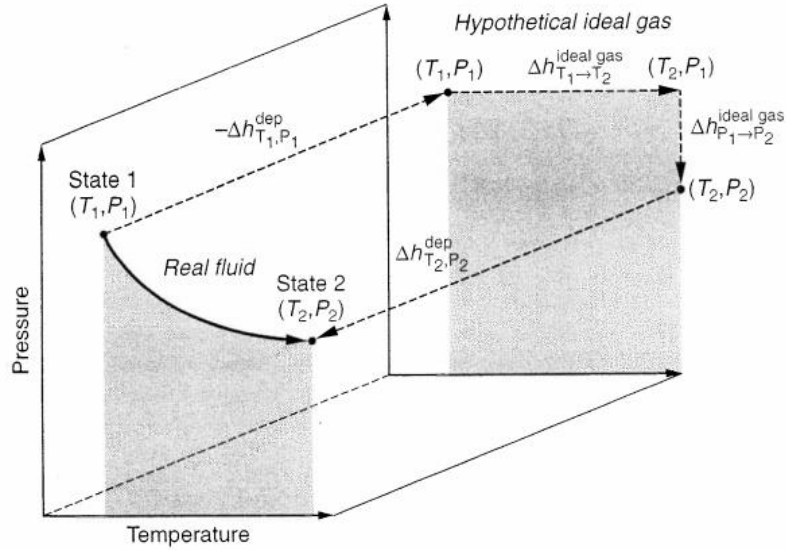
Figure 8: Paths for the change in enthalpy from State 1 to State 2 using departure functions [39].

Departure functions can be derived through integration of a derivative function defined by an equation of state. For the PR-EOS, we will start with the temperature dependent parameter *a*. By taking the derivative of *a*, we can write

$$\frac{da}{dT} = -0.45724 \frac{R^2 T_{cr}^2}{P_{cr}} \kappa \sqrt{\frac{\alpha}{T \cdot T_{cr}}} \tag{2.16}$$

Using the above equation and the computed value of compressibility in (2.10), the enthalpy departure function can calculated. First, it is derived from the Helmholtz energy and entropy departure functions:

25

$$A - A^0 = -\int_{\infty}^{V} \left(P - \frac{RT}{V} \right) dV - RT \ln \left(\frac{V}{V^0} \right) \tag{2.17}$$

$$S - S^0 = \frac{\partial}{\partial T} \left(A - A^0 \right) = \int_{\infty}^{V} \left[\left(\frac{\partial P}{\partial T} \right)_V - \frac{R}{V} \right] dV + R \ln \left(\frac{V}{V^0} \right) \tag{2.18}$$

Then from thermodynamic relations,

$$H - H^0 = \left(A - A^0 \right) + T \left(S - S^0 \right) + RT \left(Z - 1 \right) \tag{2.19}$$

$$U - U^0 = \left(G - G^0 \right) + T \left(S - S^0 \right) - RT \left(Z - 1 \right) \tag{2.20}$$

Through substitution, we can write

$$H - H^0 = RT_{cr} \left[T_r \left(Z - 1 \right) - 2.078 \left(1 + \kappa \right) \sqrt{\alpha} \ln \left(\frac{Z + 2.414B}{Z - 2.414B} \right) \right] \tag{2.21}$$

The interpretation of these departure functions can be explained simply: the changes in a state property of a real fluid is equal to that for an ideal gas experiencing the same change, plus the departure of the fluid from ideal gas behavior at the end state, and minus the departure from ideal gas behavior at the initial state.

2.2 Elemental Sulfur Dissociation

The use of elemental sulfur has previously been proposed for capturing solar energy in a direct TES configuration, in which it is pumped throughout the system as both the heat transfer and storage fluid [40]. Wirz et al. proposed using elemental sulfur in an indirect TES configuration in CSP applications, which presents many advantages [41]. Most notably, because the elemental sulfur is isolated in a containment vessel, different heat transfer fluids may be used, such as

26

synthetic oils, molten salts, liquid metals, steam, air or s-CO2 [42]. This approach also avoids the challenge of corrosiveness, leaks, and safety issues of transporting the storage fluid at high-temperatures through a receiver, extensive piping networks, and pumps as in direct TES applications, or through pumps and heat exchangers as in traditional two-tank TES systems.

One chief benefit of elemental sulfur is that it is a very inexpensive commodity; typical prices range from \$0.10/kg – \$0.16/kg. Also, sulfur vapor does not exhibit overly excessive vapor pressure at high temperatures, which eliminates the need for costly thick-walled or specially fabricated storage vessels. One of the fundamental requisites of a storage material is high thermal stability over a 30-year plant lifetime. As an element, sulfur exhibits very little, if any, thermal decomposition, which makes it an ideal candidate for high-temperature CSP operation in an environment where there are few choices for thermally stable storage fluids [23].

Additionally, sulfur is one of the few elements that can exhibit concatenation, which causes a wide variety of molecular species (primarily long chains). Elemental sulfur has a complex chemistry, and is known to exist in a variety of molecular species ranging from S_8 to S_2 as a liquid, vapor, or mixture of both. In the liquid phase, polymerization causes sulfur to form almost entirely in S_8 rings below 433 K [43, 44]. Above 433 K, the rings undergo polymerization to form long S_8 chains, which causes a dramatic increase in viscosity [45]. At even higher temperatures, the long chains begin to break into smaller chains ranging from S_{1-7}. Thus, the use of endothermic bond-breaking and exothermic bond-making reversible reactions is used as a means of energy storage [40]. The species composition as a function of temperature is shown in Figure 9.

27
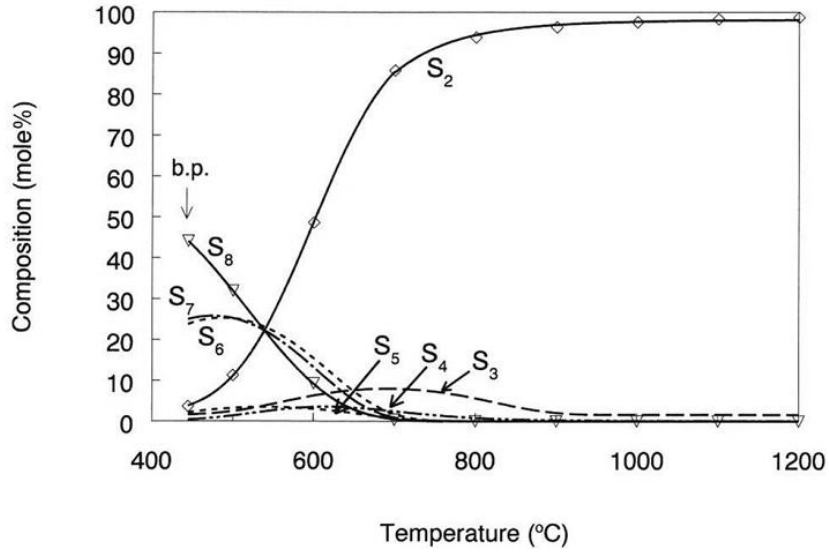
Figure 9: Species composition of elemental sulfur as a function of temperature [40].

As mentioned previously, the wide variety of molecular forms of elemental sulfur causes many thermophysical properties – such as vapor pressure, viscosity, and specific heat – to behave in ways that are difficult for traditional equations of state to numerically predict. This can be clearly concluded from the non-traditional shape of the phase diagram describing elemental sulfur, which is displayed in Figure 10.

28
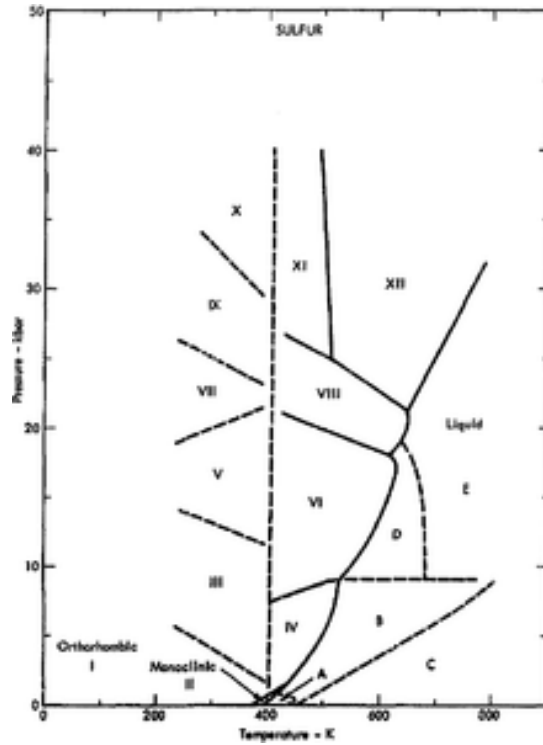
Figure 10: Phase diagram of elemental sulfur [46].

The equilibration between the various species of elemental sulfur can be described generally as the endothermic bond-breaking formation of S_2 with increasing temperature, and the exothermic bond-forming re-materialization of S_8 at lower temperatures, written as:

$$S_8 \rightleftharpoons 4S_2 \tag{2.22}$$

The standard reaction enthalpy of this conversion is $\Delta H = 414$ kJ/mol [47]. This value is an instructive metric in comparison to other reactions proposed for thermochemical energy storage, which are listed in Table 5.

29

Table 5: Chemical reactions proposed for thermochemical energy storage, adapted from [40].

Reaction	Enthalpy of reaction	Reference
$2NH_3 \rightleftharpoons N_2 + 3H_2$	92.3	Carden, 1979 [48]
$SO_3 \rightleftharpoons SO_2 + 0.5O_2$	98.9	Chubb, 1975 [49]
$CH_4 + H_2O \rightleftharpoons CO + 3H_2SO_3$	206.2	Hafele, 1974 [50]
$CH_4 + CO_2 \rightleftharpoons 2CO + 2H_2$	247.4	Wyman et al., 1980 [51]
$CaCO_3 \rightleftharpoons CaO + CO_2$	178.3	Wentworth and Chen, 1976 [52]

Moreover, the handling, storage, and transportation of elemental sulfur are well known as part of widely used technology in sulfur recovery systems in refineries and natural gas facilities. Further, this means relevant equipment and design are commercially developed [40]. Storage vessels for elemental sulfur are generally constructed from low-cost carbon steel, albeit for low operating temperatures [53].

2.2.1 Partition Functions

In statistical mechanics, partition functions describe the statistical properties of a thermodynamic system at equilibrium conditions. There are several types of partition functions, each of them dependent on state variables such as temperature, volume, or number of particles in the system. The importance of the concept is that most of the thermodynamic variables of the system, such as free energy, entropy, and pressure, can be expressed by the partition function itself or its derivatives corresponding to the different types of statistical ensembles. For example, the canonical ensemble describes a system with a fixed number of particles in the system, fixed

30

volume, and fixed absolute temperature (and is sometimes called the *NVT* ensemble). In this scenario, the system holds a fixed number of particles in a fixed volume, and is allowed to exchange heat with the environment (commonly described as a 'heat bath') at fixed temperature, which describes the canonical ensemble. Other ensembles can be constructed by fixing other thermodynamic or mechanical variables, such as the grand canonical (μVT), microcanonical (*NVE*), isoenthalpic-isobaric (*NPH*), and isothermal-isobaric (*NPT*) ensembles.
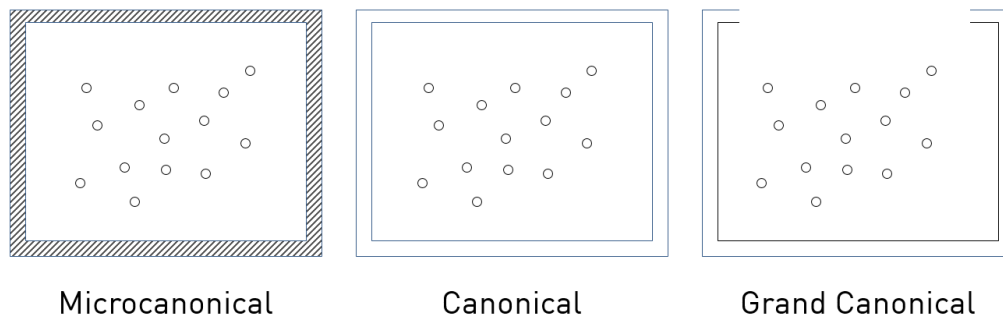
Figure 11: Diagram of microcanonical, canonical, and grand canonical ensembles.

2.2.2 Helmholtz Free Energy Minimization

Helmholtz free energy minimization techniques have been studied for numerous reactive and non-reactive systems employing various optimization methods. Overall, optimization methods must be chosen thoughtfully based upon the nature of the problem being solved; the multi-variation, non-linearity, and convexity affects the efficacy of the optimization method being implemented. Some methods used in phase and reaction equilibria modeling include linear programming, homotopy continuation algorithms, accelerated successive substitution, and deterministic and stochastic global optimization strategies [54]. Considering these complex

31

characteristics, it is understandably difficult to evaluate a global minimum of the Helmholtz free energy in phase and reaction equilibria models.

(a)   (b)
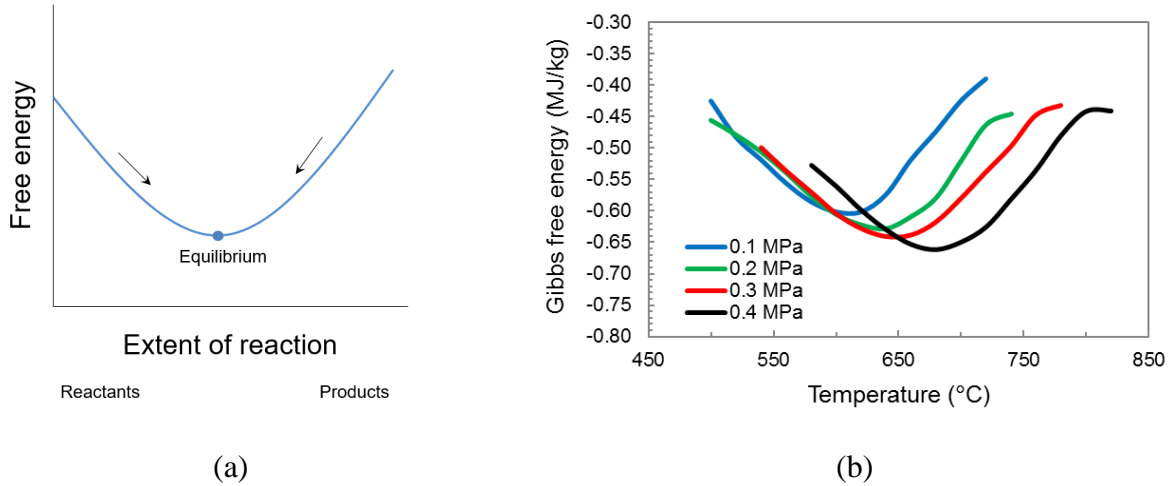
Figure 12: a) Diagram illustrating the reaction equilibrium between reactants and products, and b experimental data [55]of Gibbs free energy of elemental sulfur as a function of temperature, for various pressures.

The governing principles of free energy minimization is broadly based upon phase and reaction equilibria and fundamental thermodynamics. Knowledge of chemical reaction equilibria and multiphase equilibria is critical to understanding the behavior of thermodynamic systems, though the formulation and execution of the problem can be complex depending upon the chemical species and environmental processes under study. Nevertheless, a variety of free energy minimization methods have been reported for a wide range of chemical processes and applications. In line with the overall goal of Chapter 2, the significance and purpose of using free energy minimization is to evaluate thermodynamic properties such as pressure, entropy, and specific heat, which are defined fundamentally through Maxwell's Relations.

32

The application of the first and second law of thermodynamics can be written as

$$dU + pV \leq TdS \tag{2.23}$$

$$TdS = d(TS) - SdT \tag{2.24}$$

$$d(U - TS) \leq SdT - pV \tag{2.25}$$

The quantity $U - TS$ is known as the Helmholtz free energy, A, and we then express it as

$$dA \leq SdT - pV$$
$$\frac{dA}{dt} \leq S\frac{dT}{dt} - p\frac{dV}{dt} \tag{2.26}$$

For a closed system at constant temperature and volume,

$$\frac{dA}{dt} \leq 0, \ (\text{closed system with constant } T \text{ and } V) \tag{2.27}$$

This principle is named the Helmholtz free energy minimum principle, and it simply states that for a closed system at constant temperature and volume, the equilibrium thermodynamic state occurs at the minimum Helmholtz free energy

$$\frac{dA}{d\xi} = 0; \ \text{for equilibrium} \tag{2.28}$$

An alternative is to fix pressure instead of volume, which would describe the grand canonical ensemble, and the derivation would yield Gibbs free energy. Gibbs free energy is widely used as a criterion for phase and reaction equilibria for thermodynamic processes [56-59]. Similar analyses using Helmholtz free energy exist [59-61], but remain limited in number.

33

Consider the isothermal, isochoric chemical reaction taking place inside a rigid vessel enclosing a volume V immersed in a heat bath of temperature T. The chemical reaction initially has α moles of species A, which dissociates to β moles of species B and γ moles of species C.

$$\alpha A \rightleftharpoons \beta B + \gamma C + ... \tag{2.29}$$

The change in molar composition from one species to another can be represented by extent of reaction, ξ, defined as:

$$\xi = \Delta n_A / \alpha = \Delta n_B / \beta + \Delta n_C / \gamma \tag{2.30}$$

For a two species chemical reaction, then the extent of reaction can be written as:

$$\begin{aligned} n_A &= \alpha(1 - \xi) \\ n_B &= \beta \xi \end{aligned} \tag{2.31}$$

The assumed initial condition for the molar composition of $n_A = \alpha$ and $n_B = 0$ at $\xi = 0$, and total conversion corresponds to $n_A = 0$ and $n_B = \beta$ at $\xi = 1$. The condition of the reaction in between the two extremes is given by $0 < \xi < 1$. It should be noted that the formulation constrains the total number of molecules at any given ξ to remain constant, thereby inherently satisfying conversation of mass.

We describe the thermodynamic process in several steps, depicted in Figure 13. In order to determine the Helmholtz free energy change, we rely on the governing principle that the thermodynamic state of the system is path independent, and that only the initial and final states matter.

34

State 0

T
$P = 1\,bar$
$V = V_0$
$n_A = \alpha\,mol,\ n_B = 0\,mol$

State 1

T	T
$P = 1\,bar$	$P = 1\,bar$
$V_A = n_A RT/P$	$V_B = n_B RT/P$
$n_A = \alpha(1-\xi)\,mol,\ n_B = 0\,mol$	$n_A = 0\,mol,\ n_B = \beta\xi\,mol$

$$\Delta A_1 = \xi \Delta A^\circ$$

State 2

T
$P_A + P_B = 1\,bar$
$V_A + V_B = (n_A + n_B)RT/(P_A + P_B)$
$n_A = \alpha(1-\xi)\,mol,\ n_B = \beta\xi\,mol$

$$\Delta A_2 = RT\left[\alpha(1-\xi)\ln\left(\frac{P_A'}{P_{tot}}\right) + \beta\xi\ln\left(\frac{P_B'}{P_{tot}}\right)\right]$$

State 3

T
$P = (n_A + n_B)RT$
$V = V_0$
$n_A = \alpha(1-\xi)\,mol$
$n_B = \beta\xi\,mol$

$$\Delta A_3 = RT\left[\alpha(1-\xi)\ln\left(\frac{V_A}{V_A'}\right) + \beta\xi\ln\left(\frac{V_B}{V_B'}\right)\right]$$

Figure 13: Diagram of the thermodynamic process for the Helmholtz free energy minimization calculation, for a constant *T-V* process.

We begin at State 0 at 1 bar, a specified temperature T, and volume V with an initial extent of reaction of zero. Generally, we recognize the Helmholtz free energy change is written as

35

$$\Delta A = \Delta U - T\Delta S \qquad (2.32)$$

In State 1, the chemical reaction is advanced by an extent of reaction ξ, with each component in its own volume and undergoing isothermal ideal gas expansion. The first change in state for the thermodynamic process is simply tied to the standard state and the extent of reaction, and can be expressed as

$$\Delta A_1 = \xi \Delta A^0 \qquad (2.33)$$

where the standard Helmholtz free energy change can be related to the more available standard Gibbs free energy change and the change in moles from one species to other ($\Delta n = n_A - n_B$) at the fixed temperature by

$$\Delta A^\circ = \Delta G^\circ - RT\Delta n \qquad (2.34)$$

In State 2, the two volumes are mixed and undergo isothermal expansion by removing the wall to form a single volume at 1 bar. Returning to Eq. (2.32), we recognize the internal energy does not change during the mixing process ($\Delta U = 0$). For the reversible isothermal change in volume of an ideal gas, the entropy change is

$$\Delta S = nR \ln\left(\frac{V_{final}}{V_{initial}}\right) \qquad (2.35)$$

This quantity applies to isothermal expansion and compression equally, which we will utilize in the next step. It is also worth noting that after State 0, there is no interaction between the system and the surrounding heat bath ($\Delta S_{surroundings} = 0$). Because pressure is our iterative variable, and recognizing that volume is inversely proportional to pressure for ideal gases, we can express it in

36

terms of the partial pressure of each component (initial state), to the total pressure of the combined volume (final state). Then we can write the partial pressure for a two-species equation as

$$P_A = 1 - \xi$$
$$P_B = \frac{\beta}{\alpha} \xi$$

(2.36)

While pressure is an extensive property rather than an intensive one, we can define partial pressure of a component by Dalton's Law of Partial Pressures, which asserts that in a mixture of ideal gases, the partial pressure of component i is proportional to its mole fraction:

$$P_i' = n_i RT/V, \text{ where } \sum P_i' = P$$

(2.37)

If we assume the initial condition is at atmospheric pressure, then Eq. (2.37)can be rewritten as

$$P_i' = n_i RT/V, \text{ where } \sum P_i' = P_{tot} = 1$$

(2.38)

Then, the Helmholtz free energy change for State 2 becomes

$$\Delta A_2 = RT \left[\alpha (1 - \xi) \ln \left(\frac{P_A'}{P_{tot}} \right) + \beta \xi \ln \left(\frac{P_B'}{P_{tot}} \right) \right]$$

(2.39)

Finally, in State 3, the mixture undergoes isothermal ideal gas compression to the initial volume V_0. Following a similar process as in State 2, the Helmholtz free energy change is described by a change in volume with no contact with the surroundings which invokes Eq. (2.35). Similar to the calculation in State 2, the ideal gas partial volumes for each species can be calculated using Eq. (2.38) and solving for V. We make the transition to volume instead of pressure in order to transform the final step to compress the system from ideal gas volume V' to the initial volume V. The Helmholtz free energy change for State 3 can be written as

37

$$\Delta A_3 = RT\left[\alpha\left(1-\xi\right)\ln\left(\frac{V_A}{V_A'}\right) + \beta\xi\ln\left(\frac{V_B}{V_B'}\right)\right] \tag{2.40}$$

The total Helmholtz free energy change is expressed as

$$\Delta A = \Delta A_1 + \Delta A_2 + \Delta A_3 \tag{2.41}$$

Substituting in Eq. (2.33), (2.39), (2.40) into (2.41), we arrive at

$$\Delta A = \xi\Delta A^0 + RT\left[j\left(1-\xi\right)\ln\left(1-\xi\right) + y\xi\ln\left(y\xi/j\right)\right] \tag{2.42}$$

Recalling the equilibrium condition of Eq. (2.28), we take the derivative of Eq. (2.42), we can express the equilibrium condition as

$$\frac{\partial A}{\partial \xi} = \Delta A^0 + RT\left(y-j\right) + RT\left[-j\ln\left(1-\xi\right) + y\xi\ln\left(y\xi/j\right)\right] \tag{2.43}$$

By recognizing that the equilibrium condition occurs when Eq. (2.43) equals zero, we identify the root of the equation to determine the equilibrium extent of reaction at the specified temperature and volume.

The implementation of the Helmholtz free energy scheme outlined above is as follows. With volume (or density) specified a priori, the iteration loop enters with an initial guess value for the extent of reaction. With the guess value, the Helmholtz free energy change for States 1-3 can be calculated. The Helmholtz free energy change of State 1 can be evaluated by entering the extent of reaction in Eq. (2.33) and thermodynamic data in (2.34). Calculating the Helmholtz free energy change of State 2 requires partial pressures which are evaluated using Eq. (2.36) and should equate to unity per Eq. (2.38), which are substituted into Eq. (2.39). Finally, substituting the user-specified volume *V* and mole fraction into Eq. (2.40) yields the Helmholtz free energy change of State 3.

38

Combining the free energy changes of all states as in Eq. (2.42) yields the Helmholtz free energy change with respect to extent of reaction. This process is then repeated with another guess value of extent of reaction and the derivative in Eq. (2.43) can be calculated and must equate to zero in order to determine the equilibrium value of extent of reaction at the given temperature. The objective function given by Eq. (2.43) is optimized using the 'fmincon' function built in MATLAB. When the change in the optimal value of the objective function reaches a specified convergence tolerance, the equilibrium condition is considered satisfied, and the values for saved as the global solution.

The evaluation of thermodynamic properties using free energy minimization is generally much more computationally demanding than using EOSs or property libraries, because of the potentially high number of iterations needed for convergence and possibility of numerical instability. The modified Newton-Raphson method moves the algorithm in the direction of descent toward the minimum free energy in principle, but can still move the calculation towards non-physical solutions and numerical instability. Therefore, a procedure to constrain the algorithm is implemented to guarantee convergence by selecting a damping factor for the descent step. However, this procedure makes convergence relatively slower, though not intractably so. The higher guarantee for convergence is worth the computational cost, and computing time is dramatically reduced by considering only two species.

Through incorporating first principles, the model is by definition thermodynamically consistent and satisfies all thermodynamic relations. Several internal checks are implemented to observe conservation of mass and energy. The equilibrium model enables predictive capability into what is thermodynamically attainable; however, a model built purely upon phase and reaction

39

equilibria has its limitations – therefore, experimental data is incorporated into the model as another validity check. The availability of thermodynamic data varies for each species, and some sources provide thermodynamic properties in the form of tabulated data, correlations, and plots. JANAF thermodynamic data [62] was selected as the core data set, and other standard state property values were obtained from various sources [47, 55, 63-68]. Because only two species are being considered, the mass balance is simple to constrain. However, the sum of the partial pressures can still exceed the guess value of the total pressure (due to an erroneous compressibility factor and fugacity coefficient), which would be a violation of the First Law. Therefore, the guess value of the total pressure is adjusted until it converges to a specified tolerance.

Figure 14 - Figure 16 show model validation using thermodynamic property data available for elemental sulfur at one atmosphere from various sources.
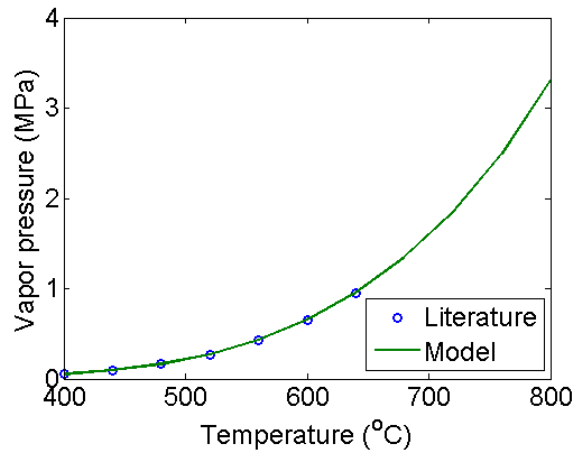
Figure 14: Vapor pressure comparison of experimental data and modeled results at 1 atm. Data for the vapor pressure of elemental sulfur is from Shuai [66].

40

From an engineering perspective, vapor pressure is arguably one of the more important properties to accurately model in order to safely design the TES system to accommodate pressure vessel standards. Figure 14a shows the value of vapor pressure as a function of temperature for 1 atm. For typical CSP plants with a maximum operating temperature of 565°C, elemental sulfur reaches 0.43 MPa, which is relatively modest. Vapor pressure becomes an exponentially increasing challenge for future CSP plants with higher operating temperature, which affects the wall thickness and the subsequent cost of the pressure vessel.

Liquid phase   **Vapor phase**

(a)   (b)
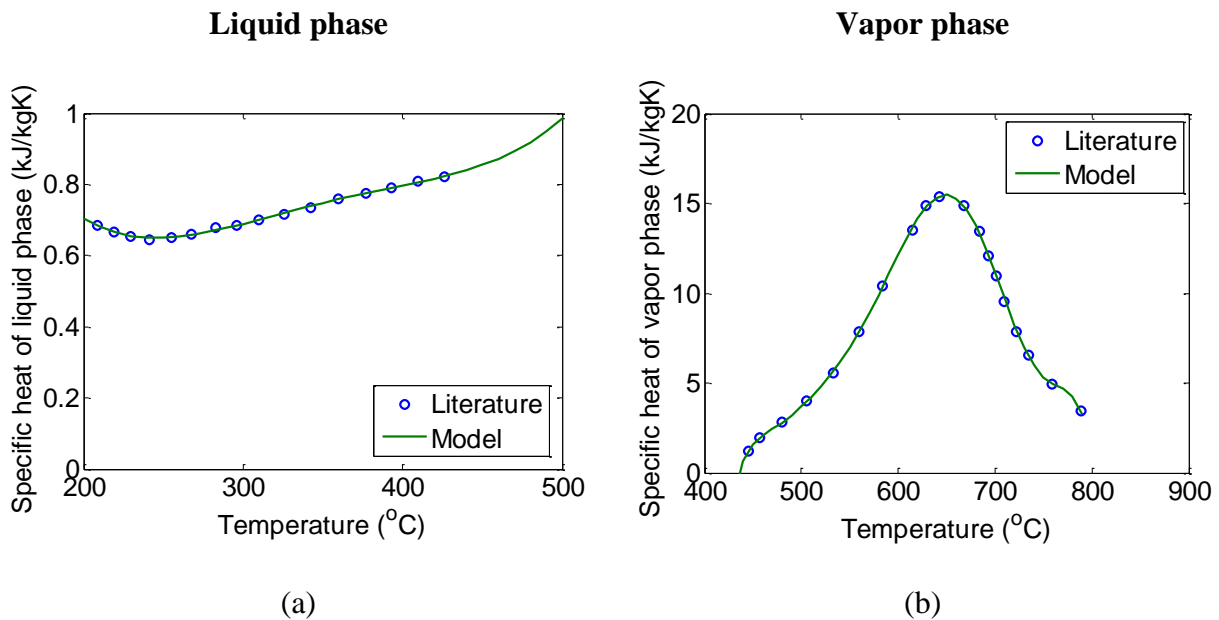
Figure 15: Specific heat comparison of experimental data and modeled results at 1 atm for a) liquid phase, and b) vapor phase. Data for the liquid specific heat and vapor specific heat of elemental sulfur is from Lewis and Randall [69], and Stull [62], respectively.

Specific heat is one of the most important properties of any storage fluid candidate. Figure 15a and Figure 15b show the liquid and vapor effective specific heat, respectively. The specific heat for

the vapor phase in Figure 15c reveals a few interesting characteristics of employing elemental sulfur as a storage fluid. As described previously, the dissociation from S_8 to S_2 enables an appreciable amount of energy to be stored in the endothermic bond-breaking process and, alongside sensible and latent heat storage, can be represented in an effective specific heat value. The vapor phase contains the majority S_2, in which dissociation primarily takes place and causes a dramatic increase in effective specific heat when the equilibrium extent of reaction increases, and then decreases as the dissociation process slow down. The liquid phase contains majority S_8 and therefore does not observe the large increase in effective specific heat.

Liquid phase   **Vapor phase**

(a)   (b)
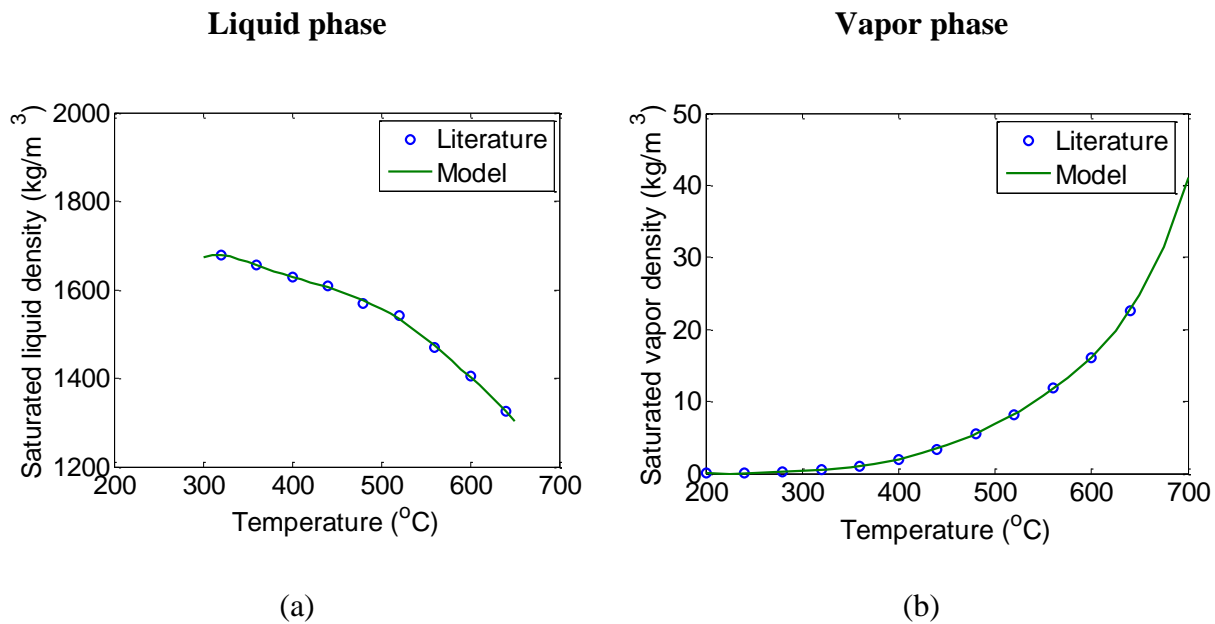
Figure 16: Density comparison of experimental data and modeled results at 1 atm for a) liquid phase, and b) vapor phase. Data for density of elemental sulfur is from Tuller [55].

Figure 16a and Figure 16b show the liquid and vapor densities, respectively. The saturated liquid density is of more importance because the elemental sulfur would likely be contained initially as

a liquid at one atmosphere. Therefore, the liquid density at the loading conditions would effectively fix the volume for the isochoric process. Both values naturally dictate the remaining fluid properties by affecting the quality of the two-phase mixture in the enclosed volume. By connecting the fluid properties modeled and validated in Figure 14 and Figure 16, the liquid-vapor dome for elemental sulfur can be represented and is shown in Figure 17 to illustrate this point.
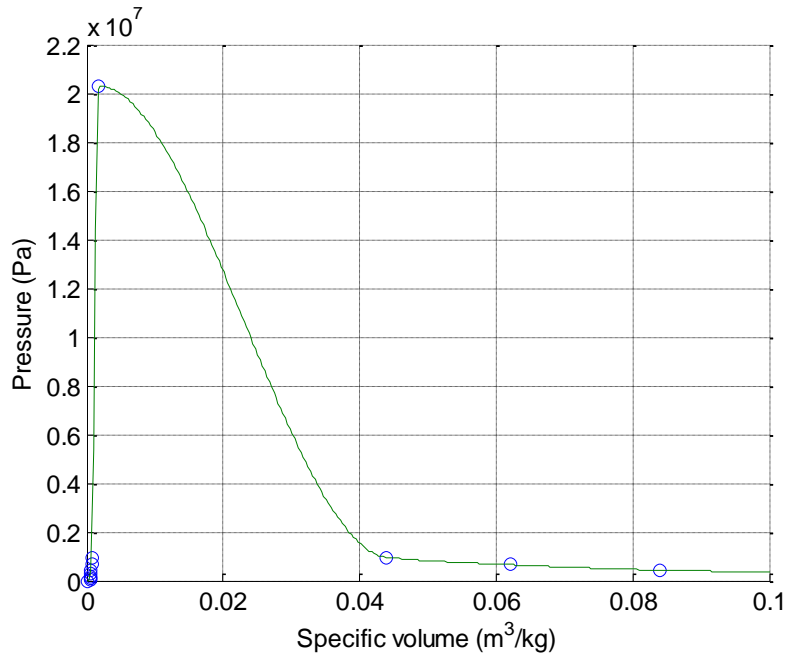
Figure 17: Elemental sulfur liquid-vapor dome.

The critical point of elemental sulfur is 1040°C and 20.7 MPa [47], and is included as a benchmark for the model. It is instructive to observe that the quality of the two-phase mixture has a direct impact on the mixture properties, which are a weighted combination of the liquid and vapor fluid properties which can vary greatly, within themselves and relative to each other.

43

The importance of modeling using Helmholtz free energy minimization is to observe the effect of high pressure upon fluid properties. Figure 18 shows the boiling point temperature as a function of pressure.
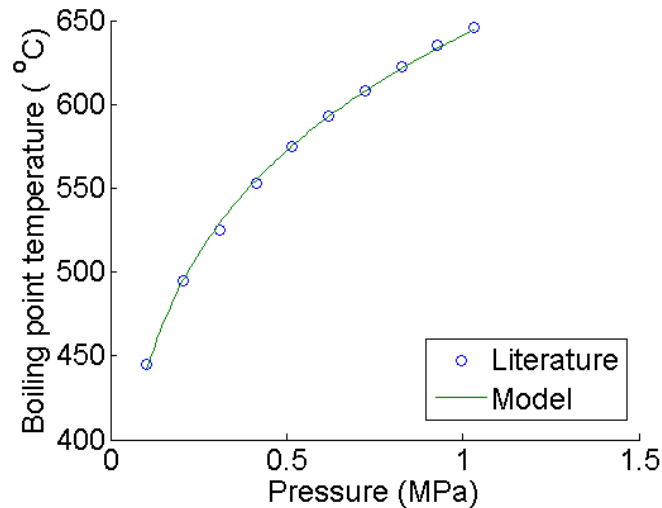
Figure 18: Boiling point temperature of elemental sulfur as a function of pressure, with literature values from Tuller [55].

Figure 18 reveals an intuitive, yet informative result. Because the boiling point of elemental sulfur increases with pressure, the dissociation reaction is consequently delayed and occurs at an increasingly slower rate as temperature increases. To illustrate this point further, the enthalpy and entropy of elemental sulfur as a function of temperature and pressure is shown in Figure 19.

44

| (a)   (b) |
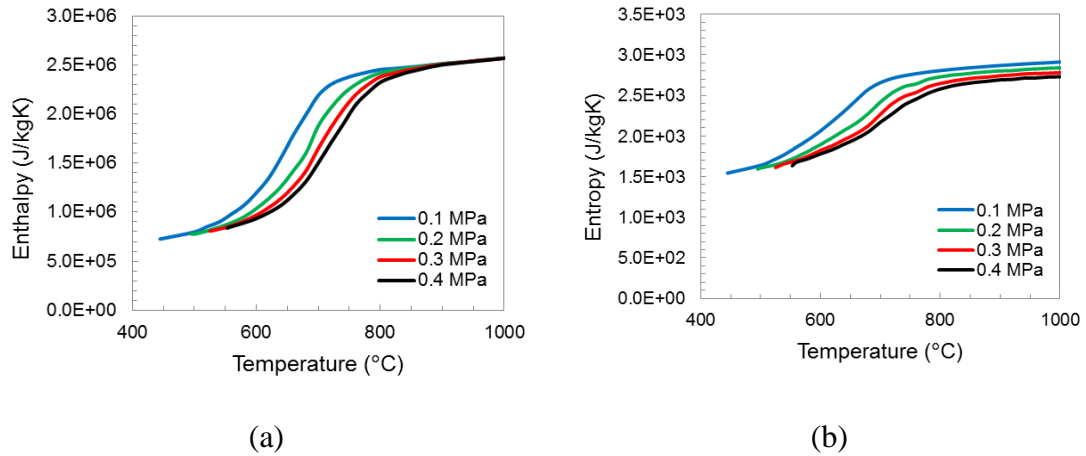
Figure 19: Thermophysical properties of elemental sulfur at saturated liquid density, as a function of temperature and pressure.

The existing literature presents elemental sulfur properties for isobaric conditions. Figure 20 shows the isochoric specific heat as a function of maximum temperature and temperature differential.

45
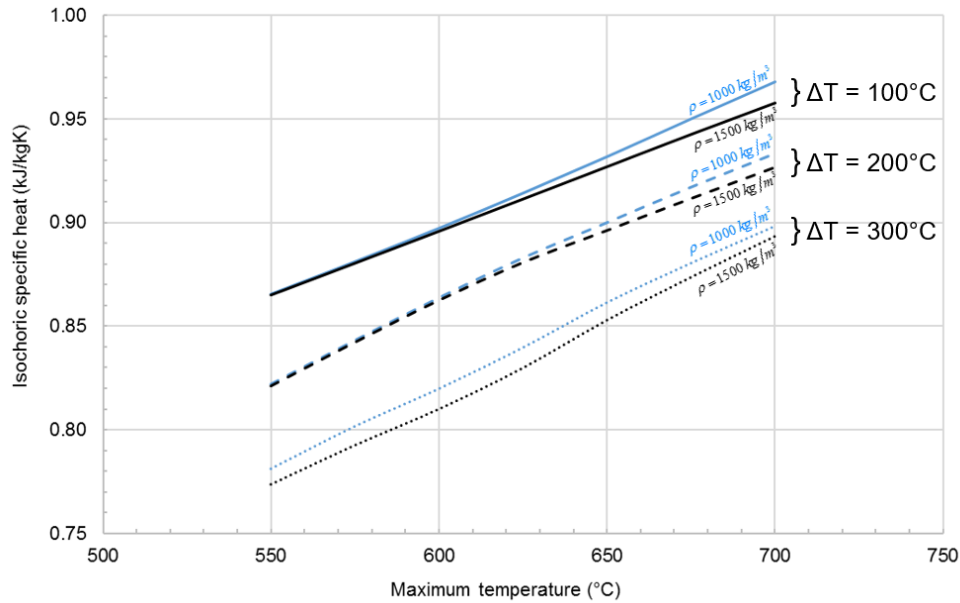
Figure 20: Isochoric specific heat of elemental sulfur as a function of maximum temperature and loading density.

Increasing the maximum temperature of the TES system increases the isochoric specific heat, in large part because it causes the quality of the two-phase mixture to increase, i.e. it contains more vapor than liquid. Because the vapor phase of elemental sulfur contains a larger molar fraction of S_2 than the liquid phase (and therefore, undergoes thermochemical dissociation to a greater degree), the isochoric specific heat increases. Conversely, increasing the loading density decreases the isochoric specific heat because it causes the quality of the two-phase mixture to decrease, i.e. it contains more liquid than vapor.

Also, it is noteworthy that Figure 20 displays the influence of each parameter relative to one another. It is clear that the maximum temperature and the temperature differential are strong drivers, whereas the loading density plays a lesser role. However, while the loading density may

46

be a weak driver for isochoric specific heat and other fluid properties, it will have a substantial impact upon other metrics, such as volumetric energy density.

This section presents the methodology of fluid properties. Thermodynamic databases and correlations for fluids of interest were collected when possible. The primary undertaking of modeling was utilizing Helmholtz energy as the fundamental state variable in an isochoric process, with temperature and density as independent variables of density and temperature. Validation and results of modeled fluid properties are shown for a range of fluid candidates. In addition, because CSP plants can experience off-design conditions on a regular basis, fluid properties are also evaluated for a wide range of varying operating conditions. A brief comparative study is conducted to give the reader a convenient glimpse into the relative difference of fluid properties of HTF and storage fluid candidates. The following section will then implement these models into an annual simulation of a CSP plant.

2.3 Property Libraries

Many thermodynamic property databases have been created and maintained for other scientific endeavors to conduct accurate analysis. Databases come in many different forms, including raw data, web interfaces with queries, and formulas. Special care must be taken when combining databases from various sources; in many cases, experimental data are combined with theoretical calculations, with some data being not available. The thermodynamic properties of interest include isobaric and isochoric specific heat, thermal conductivity, enthalpy, entropy, pressure, density, and dynamic viscosity. Other properties, such as critical temperature, critical pressure, and acentric

47

factor, are also of interest for utilizing equations of state, which is described in more detail in the Section 2.2.

The National Institute of Standards and Technology (NIST) created the Chemistry Webbook, which is available for free [70], and the Reference Fluid Thermodynamic and Transport Properties (REFPROP) program [71], for which a license must be purchased. Both databases contain thermodynamic properties for an incredibly extensive range of fluids and mixtures. The Chemistry Webbook was primarily used in this work for gathering critical properties for use in equations of state, and REFPROP was used to model storage fluid candidates such as xylene, decane, naphthalene, as well as power cycle working fluids such as carbon dioxide. Additionally, the Engineering Equation Solver program has built-in fluid property tables aggregated from various studies [72] which enables convenient analysis for thermodynamic processes employing different fluids. For this study, EES was primarily used to analyze representative Rankine and s-CO_2 power cycle models and preliminary modeling of the coolants such as steam and air. Because supercritical CO_2 properties vary widely, EES was especially useful for modeling the s-CO_2 power cycle performance with high accuracy.

Another approach to evaluating properties is to use regressions or formulas. Calling REFPROP in a subroutine to calculate properties provides the system model with highly accurate values, but is computationally expensive. Evaluating properties using regression models is much more efficient, but model assumptions and limitations must be observed and interpolation must have an adequately fine resolution to attain high accuracy. Regression models were employed to model a variety of heat transfer fluids, including Therminol 66, Therminol VP-1, nitrate salt, potassium nitrate salt, HiTec, and HiTec XL. Generally, heat transfer fluids are limited by

48

operating temperature. Therminol and other synthetic oils are typically limited to a maximum operating temperature; for instance, Therminol VP-1 is recommended not to exceed 400°C due to thermal decomposition [73]. Molten salts are a broad category that describes a widespread variety of salts with properties varying significantly for each chemical compound. Molten salts face unique challenges; often, they require mixtures with other salts to achieve desirable properties, and typically have a relatively high freezing temperature (for instance, 257°C for the 60% $NaNO_3$, 40% KNO_3 mix [42]).

49

Chapter 3

Thermodynamic Modeling of the TES System

3.1 System Definition

The primary objectives of building simulation, analysis, and design tools are to evaluate system performance, and gather insight into TES operation and opportunities for performance enhancement. Numerical modeling of TES systems has been widely studied for numerous systems. Aceves-Saborio et al. [74] presented a versatile lumped model for characterizing a wide range of latent heat storage systems, with emphasis on the potential for a wide range of applications. In Rosen's work [75], the importance of modeling spatial variations of temperature in TES systems is demonstrated and can provide significant accuracy in estimating the thermodynamic performance of such systems.

This chapter describes the development of a thermodynamic model of a TES system integrated into a CSP plant. The transient nature of the system requires detailed modeling based upon fundamental principles, which are detailed in this chapter. Additionally, for a user-specified set of operating parameters – including maximum storage temperature, storage fluid, and energy storage capacity – the model is able to calculate the required storage fluid mass, thickness of containment material, and volume of the tank, to name a few. This is achieved through thermodynamic property modeling, which was detailed in Chapter 2.

The thermal energy storage unit interacts with the charging and discharging loops, as shown in Figure 21. In the charging loop, energy collected the solar field is transferred to the tube

50

bundles containing the storage fluid via heat transfer from the HTF. The discharging loop reverses this process and extracts energy from the tube bundles to the HTF, to produce electricity from the power cycle.
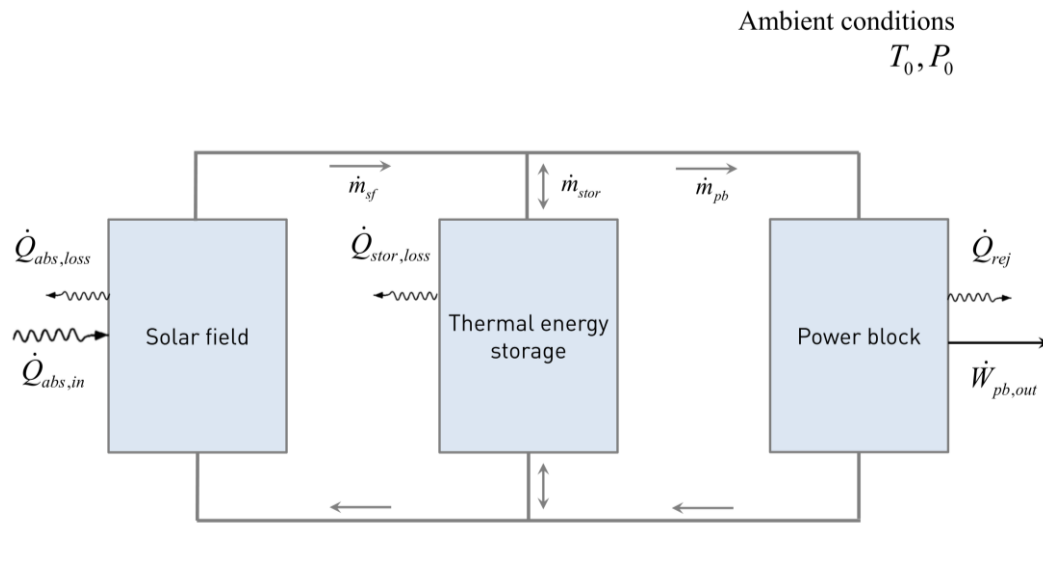
Figure 21: Basic components of a CSP plant.

.

The solar field is the subsystem of a CSP plant that converts direct normal irradiation (DNI) from the sun into thermal energy. One typical configuration uses parabolic trough collectors to focus sunlight on a cylindrical receiver. Another common configuration employs heliostats to concentrate sunlight on a central tower/receiver. In both cases, the HTF is circulated through the receiver to absorb the incident solar thermal energy, and exits the solar field to the power block for power generation, or to thermal energy storage for later use. Examples of both configurations are shown in Figure 22.

51

<div align="center">(a)   (b)</div>

Figure 22: a) Parabolic trough collector field at Kramer Junction, California (photo: NREL), and b) heliostat field with central tower/receiver of Crescent Dunes Solar Energy Project (photo: SolarReserve)

Figure 23 shows the interconnection of the models at a high level, while the following subsections provide detailed methodologies and assumptions for each model.

www.manaraa.com
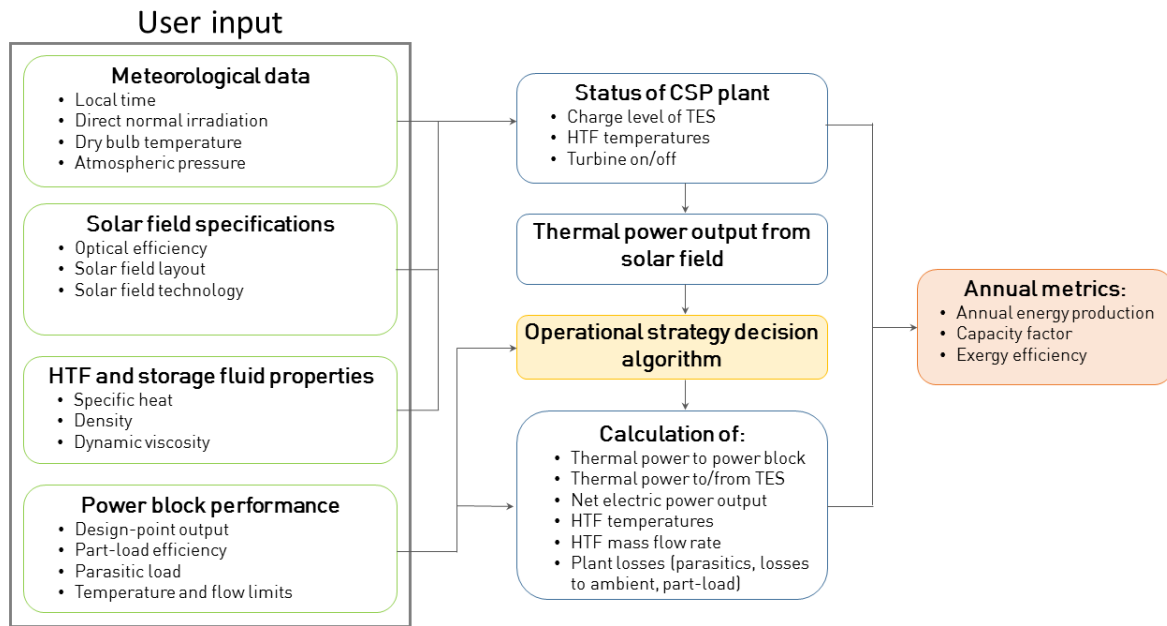
Figure 23: Schematic of the information flow for the system model.

3.1.1 Review of Modeling Tools

Engineering Equation Solver (EES) is a robust engineering analysis program, developed by the University of Wisconsin, Madison, and includes comprehensive property lookup tables, the capability to solve simultaneous equations, and built-in parametric optimization. Its System Advisor Model (SAM) is a comprehensive energy modeling program developed by NREL [27] to evaluate the performance of several renewable energy systems including CSP technologies such as parabolic trough and power tower plants integrated with TES. SAM also includes detailed financial modeling, which provides a consistent framework to compare the economic viability of various renewable energy technologies. This economic modeling framework serves as a foundation for the techno-economic analysis of this work and is described in more detail in Chapter 6. Several advanced power cycle models are also integrated into this analysis, namely Wagner [76]

53

for Rankine cycle performance, and Dyreby [77] and Seidel [78] for s-CO₂ cycle performance. This is described in more detail in the Power Block section of Chapter 2.

3.2 Solar Field

3.2.1 Parabolic Trough

The solar field consists of individual solar collector assemblies connected in series with header pipes connecting multiple loops to the TES system and power block. The solar field assumes steady-state operation, which is accurate during the majority of operating hours, but does not account for the warm-up period during the beginning of the day, which results in over-prediction of HTF temperatures. The baseline HTF in the model is potassium nitrate salt, which has a maximum allowable temperature range of 240°C - 579°C. The thermal power absorbed by the solar field at design point is given by:

$$\dot{Q}_{sf,des} = \eta_{opt} \cdot \eta_{th} \cdot DNI_{des} \cdot A_{sf} \tag{3.1}$$

where the reference for the solar plant design point is $DNI_{des} = 950 \text{ W/m}^2$ on equinox at solar noon [79], and A_{sf} is the total reflective area projected on the plane of the parabolic trough collector aperture, which is distinct from the total curved reflective area. The useful thermal power from the solar field is evaluated as the absorbed solar irradiation minus the thermal losses:

$$\dot{Q}_{sf,net} = \dot{Q}_{sf,abs} - \dot{Q}_{sf,loss} \tag{3.2}$$

The thermal loss of the solar field is modeled using an empirical correlation developed from measurements of a EuroTrough collector [80]:

54

$$\dot{Q}_{sf,loss} = \left[\left(b_1 \Delta T + b_2 \Delta T^2\right) + \dot{q}_{sf,loss}\right] A_{sf} \tag{3.3}$$

where the temperature difference is defined as:

$$\Delta T = \left(\frac{T_{sf,in} + T_{sf,out}}{2}\right) - T_{amb} \tag{3.4}$$

The mass flow rate through the solar field to achieve design-point HTF outlet temperature is evaluated by:

$$\dot{m}_{sf} = \frac{\dot{Q}_{sf,abs}}{c_{p,htf}\left(T_{sf,out,des} - T_{sf,in}\right)} \tag{3.5}$$

Solar multiple is defined as the ratio of thermal power collected by the solar field to required thermal input of the power block at design conditions.

$$SM = \frac{\dot{Q}_{sf,des}}{\dot{Q}_{pb,des}} \tag{3.6}$$

3.2.2 Power Tower

A wide range of detailed information is required to accurately evaluate the central receiver and heliostat field performance, including tower and receiver geometry, heliostat field layout, HTF piping configuration, among others. The central tower, receiver, and heliostat field are designed using the Power Tower Generator program (PTGen), developed by Wagner. It is programmed in Fortran to generate the design specifications for power tower systems and calls upon DELSOL, a central receiver and heliostat field design tool developed by Sandia National Laboratories. Several modifications to the DELSOL code were made to ensure compatibility with newer versions of Fortran and to integrate it more easily into PTGen. The model inputs include solar multiple and

55

meteorological data. The Typical Meteorological Year (TMY) database [81] is used for Daggett, CA and the reference direct normal irradiation is 950 W/m^2. The performance of the heliostat field and central receiver are assumed to be independent of other plant subsystems. Therefore, the annual thermal energy absorbed by various solar field technologies can be evaluated annually separately. The limitation of this approach involves the inflexibility of the heliostat field layout, tower height, and receiver geometry, which is likely not optimized for varying solar multiple values.

3.3 Thermal Energy Storage

3.3.1 Single-Tank Design

In modeling the transient behavior of the TES system, the storage fluid, tube wall material, and HTF are characterized individually and are in thermal communication with each other and is illustrated in Figure 24. The storage fluid, tube wall material, and HTF inside the TES tank can be envisioned with the simplified control volume in Figure 24. Equations (3.7) - (3.9) represent the individual energy balances for each component.
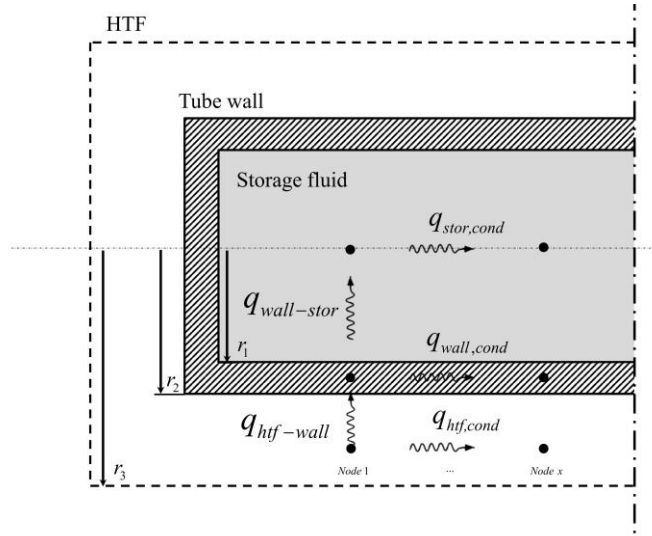
Figure 24: Diagram of the thermal energy storage components. Each component is modeled with cross-sectionally averaged temperature, and heat transfer is considered radially and axially, while circumferential is not.

Energy balance for the storage fluid:

$$\left(\rho c A\right)_{stor} \frac{\partial T_{stor}}{\partial t} = -\left(hP_h\right)_i \left(T_{stor} - T_{wall}\right) + \left(kA\right)_{stor} \frac{\partial^2 T_{stor}}{\partial x^2} \tag{3.7}$$

Energy balance for the tube wall material:

$$\left(\rho c A\right)_{wall} \frac{\partial T_{wall}}{\partial t} = \left(hP_h\right)_i \left(T_{stor} - T_{wall}\right) - \left(hP_h\right)_o \left(T_{wall} - T_{HTF}\right) + \left(kA\right)_{wall} \frac{\partial^2 T_{wall}}{\partial x^2} \tag{3.8}$$

Energy balance for the HTF:

$$\left(\rho c A\right)_{HTF} \frac{\partial T_{HTF}}{\partial t} + \dot{m}_{stor} c_{HTF} \frac{\partial T_{HTF}}{\partial x} = \left(hP_h\right)_o \left(T_{wall} - T_{HTF}\right) + \left(kA\right)_{HTF} \frac{\partial^2 T_{HTF}}{\partial x^2} \tag{3.9}$$

Equations (3.7) - (3.9) assume a constant value of h_i and h_o, the inner and outer heat transfer coefficients. The design-point value of hP_h is informed from FLUENT simulations of HTF

57

flowing in a shell-and-tube heat exchanger with tubes of radius r_i, through an outer cylindrical control volume of r_a, utilizing the values for fluid properties and mass flow rate. The equations also assume that the bulk mean and cross-sectional average temperatures are identical for the HTF; this assumption has been shown to be quite accurate from the FLUENT simulation, and the value of h_o is obtained from Zukauskas [82]:

$$\overline{Nu_o} = \frac{(hD)_o}{k_{HTF}} = CRe_{max}^m Pr_{HTF}^{0.36} \left(\frac{Pr}{Pr_s}\right)^{1/4} , for \begin{bmatrix} N_L \geq 20 \\ 0.7 \leq Pr \leq 500 \\ 1000 \leq Re_{max} \leq 2 \times 10^6 \end{bmatrix} \quad (3.10)$$

$$where \begin{cases} C = 0.35 \left(\frac{S_T}{S_L}\right)^{0.2} and\ m = 0.6 \left(for\ 10^3 \leq Re_{max} \leq 10^5\right) \\ C = 0.021\ and\ m = 0.84 \left(for\ 2 \times 10^5 \leq Re_{max} \leq 2 \times 10^6\right) \end{cases} \quad (3.11)$$

C and m are for staggered tube configuration, and Re_{max} is based on the maximum fluid velocity within the tube bank. For a staggered arrangement,

$$S_D = \left[S_L^2 + \left(\frac{S_T}{2}\right)^2 \right] < \frac{S_T + D}{2} \quad (3.12)$$

$$V_{max} = \begin{cases} \dfrac{S_T}{2(S_D - D)} \overline{V} \\ \dfrac{S_T}{S_T - D} \overline{V} \end{cases} \quad (3.13)$$

where S_T, S_L and S_D are the transverse, longitudinal, and diagonal pitch, respectively. The storage tubes and tank are assumed to be the same length, and the boundaries at the tank inlet and outlet are assumed adiabatic. With regard to initial temperature conditions, the storage tank is initially

58

assumed to be fully discharged. Then, cyclic operation is performed until the temperatures within the tank achieve a steady periodic condition.

3.3.3 Integration with CSP Plant

One notable design implementation is the addition of a bypass loop, which allows HTF from the solar field to bypass the TES system and directly flow to the power block. Then, the energy balance of the HTF loop is developed. Referring to the discharge loop in Figure 21 and assuming no losses in the piping, the energy balance for the HTF flowing within the discharge loop is:

$$\dot{m}_{pb}T_{pb,in} = \dot{m}_{sf}T_{sf,out} + \dot{m}_{stor}T_{stor,out} \tag{3.14}$$

Equality of the HTF temperature at the generator outlet and the tank inlet (assuming no losses in the piping):

$$T_{tank,in} = T_{pb,out} \tag{3.15}$$

3.3.4 TES Sizing

The sizing of the TES system is based upon user-defined TES specifications, such as the desired energy storage capacity, operating temperature range, tube geometry, and choice of HTF, tube wall material, and storage fluid. The primary output is the required mass of storage fluid and tube wall material necessary to meet the desired energy storage capacity. First, the total energy stored in the TES tank is:

$$E_{stor,tot} = \left(m\Delta\bar{u}\right)_{stor} + \left(mc\Delta\bar{T}\right)_{wall} + \left(mc\Delta\bar{T}\right)_{HTF} \tag{3.16}$$

where Δu is the difference in specific internal energy between the initial and final states of the storage fluid. Note that E_{tot} also represents the quantity of solar energy that had to be diverted to

storage during the charge portion of the cycle. Generally, TES capacity is expressed in hours. This value, Δt_{stor}, represents the number of hours that the TES system can supply thermal energy to operate the power cycle at design-point power output. The TES capacity expressed in units of energy, $E_{stor,tot}$, can be written as:

$$E_{stor,tot} = \frac{\dot{W}_{pb,des} \Delta t_{stor}}{\eta_{pb,des}} \tag{3.17}$$

where $\dot{W}_{pb,des}$ is the design-point power block output. Generally, in TES applications, a constant pressure process is assumed and therefore, the isobaric specific heat, c_p, is used. In this study, the storage fluid is encapsulated in a tube and undergoes a constant volume process. The appropriate isochoric specific heat is defined by Maxwell's Equations as:

$$c_v = \left(\frac{\partial u}{\partial T} \right)_V \tag{3.18}$$

Therefore, the value of c_{stor}, the effective specific heat of the storage fluid, is defined as

$$c_{stor} = \frac{\Delta \bar{u}}{\Delta T} \tag{3.19}$$

where $\Delta \bar{u}$ is the change in internal energy per unit mass corresponding to an incremental change in temperature, ΔT, which is operationally taken across one time step.

The required wall thickness can be determined using the expression for hoop stress in a thin-walled cylinder. The result is expressed as:

60

$$t_w = \frac{nP_{max}r_i}{F_{tu}}$$

<div align="right">(3.20)</div>

where n is the safety factor, P_{max} is the maximum pressure, and F_{tu} is the allowable tensile strength derated at the maximum operating temperature.

3.4 Power Cycle Modeling

The power cycle technologies typically used in CSP applications are the Rankine and supercritical carbon dioxide (s-CO_2) Brayton cycles. The Rankine cycle is well understood and has been widely studied. The s-CO_2 cycle was initially developed for nuclear applications [83, 84], and have recently garnered attention for integration with CSP plants because of its relatively higher thermal efficiency, attractive fluid properties and reduced turbomachinery costs [85-88].

Existing models for Rankine and s-CO_2 cycles employ fundamental thermodynamic equations; however, the need to evaluate fluid properties of the working fluid generally is computationally expensive. In contrast, regression models are dramatically faster, though special care must be taken to ensure accuracy and to avoid non-physical behavior.
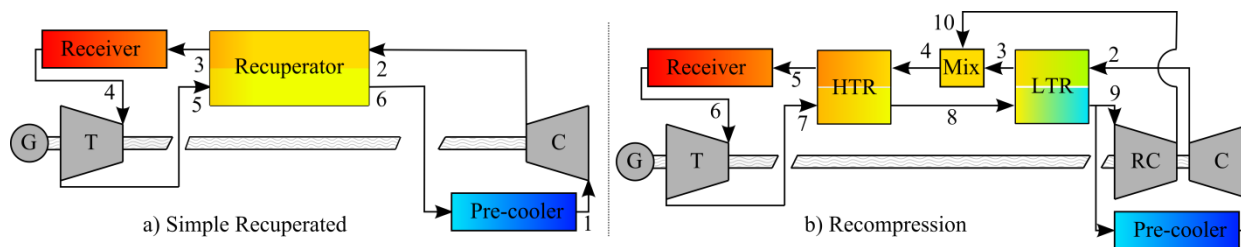
Figure 25: Component diagram of a) simple recuperated, and b) recompression s-CO_2 cycle.

61

A Rankine cycle can have a myriad of design configurations, involving evaporation, steam extraction points, multiple stages, and condensation. Similarly, a s-CO₂ cycle can have several configurations of turbomachinery, heat exchangers, and flow splitters to optimize different temperature or pressure characteristics of a specific application as shown in Figure 25. An illustrative T-s diagram of the thermodynamic process for both cycles is shown in Figure 26.
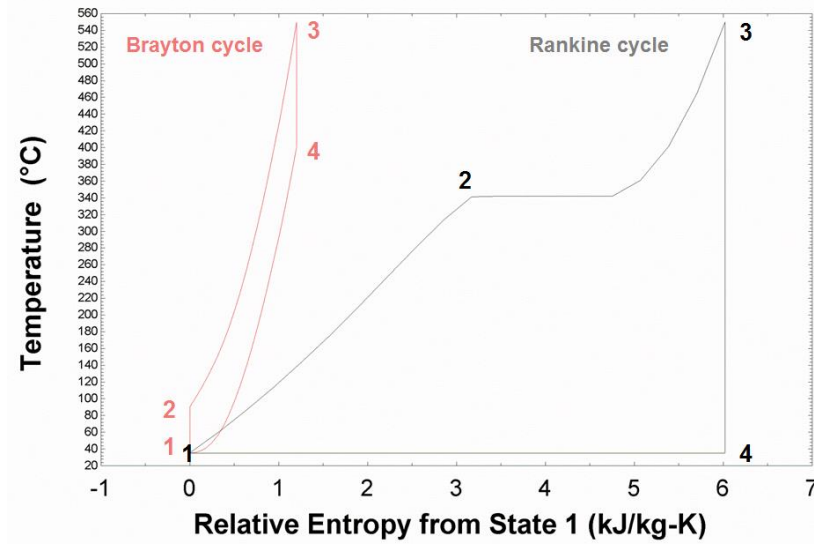
Figure 26: Temperature-entropy diagram for the Brayton and Rankine cycle used in the study.

3.4.1 Cycle Design and Performance

The current work analyzes different CSP technologies, which raises the challenge of designing a model that can be applied for multiple system designs. Similar to the TES model, various power block correlations are used to compare the performance of multiple system designs by assuming a "black box" model. This approach allows the user to design a system more easily by connecting the required power block inputs to other system components with the power block model outputs.

62

Regression models are used for sub-critical steam Rankine cycle for design point and part-load performance is modeled, which considers the efficiency reduction for operation at temperatures lower than design point. This sliding pressure operation has been evaluated empirically by Wagner [89] for steam Rankine cycles, and Seidel [78] for the s-CO$_2$ recompression cycle. The s-CO$_2$ recompression cycle model models an agnostic heat source input into the CO$_2$ stream.

With the addition of the TES model, specifically its governing principles of the tube bundle as a heat exchanger, the HTF temperature may approach a turbine inlet temperature different the design-point value, thus affecting efficiency. Subsequently, a colder turbine inlet temperature results in a power block HTF outlet temperature that deviates from design-point value. Warmer power block HTF outlet temperatures are of concern, because this effectively reduces thermal energy storage capacity (which is dependent upon a temperature differential), and impacts heat transfer and fluid flow through the solar field, and may risk venturing into unfavorable HTF property regimes. The specific design parameters for each cycle design under study are shown in Table 6. The nameplate capacity is 10 MW$_e$ by default, unless specified by the user.

Table 6: Specifications of the three power cycle configurations implemented into the system model.

Design-point parameters	Sub-critical Rankine (wet-cooled)	s-CO$_2$ Brayton (wet-cooled)	s-CO$_2$ Brayton (dry-cooled)
Nameplate capacity (MWe)	10.0	10.0	10.0
Thermal efficiency (-)	0.33	0.41	38.3
HTF mass flow rate (kg/s)	81.6	150	230

63

Hot HTF inlet temperature (°C)	565	626	626
Cold HTF outlet temperature (°C)	298	506	547
Cooling water inlet temperature (°C)	27.6	26.0	-
Cooling water outlet temperature (°C)	38.4	34.0	-

Previous studies have explored off-design behavior of the receiver [76, 89], heat exchangers [90, 91], and power cycle [77, 89] when operating parameters deviate from design-point values. This section describes the impact and relative magnitude of multiple parameters simultaneously experiencing off-design conditions on system behavior.

In the analysis, the power cycle performance is dependent upon three variables: the HTF inlet temperature, HTF mass flow fraction, and the ambient temperature. The design-point values are given in Table 6. The non-dimensional HTF temperature for the regression is defined as:

$$\hat{T}_{HTF,in} = \frac{T_{HTF,in} - T_{HTF,out,des}}{T_{HTF,in,des} - T_{HTF,out,des}} \tag{3.21}$$

The power output is assumed to scale proportionally with the HTF mass flow fraction. The mass flow fraction is defined as the ratio of the HTF mass flow rate to the design-point value:

$$\hat{\dot{m}}_{htf} = \frac{\dot{m}_{htf}}{\dot{m}_{htf,des}} \tag{3.22}$$

64

Sub-critical Rankine cycle   **s-CO₂ recompression cycle**

(a)
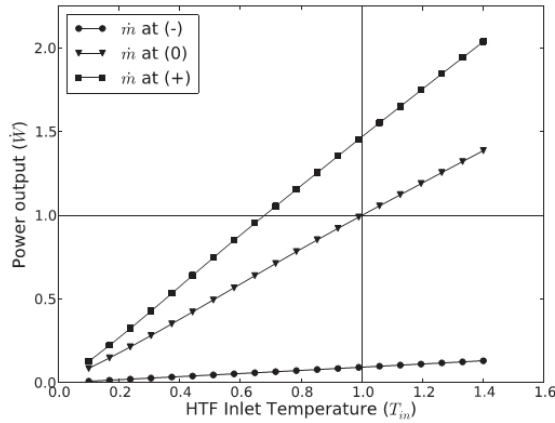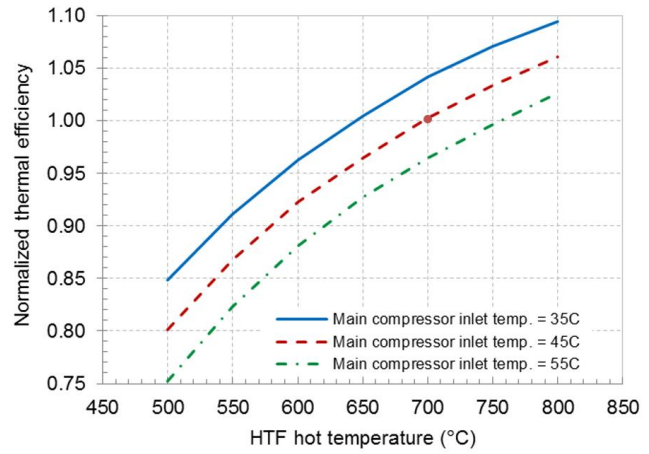
(b)
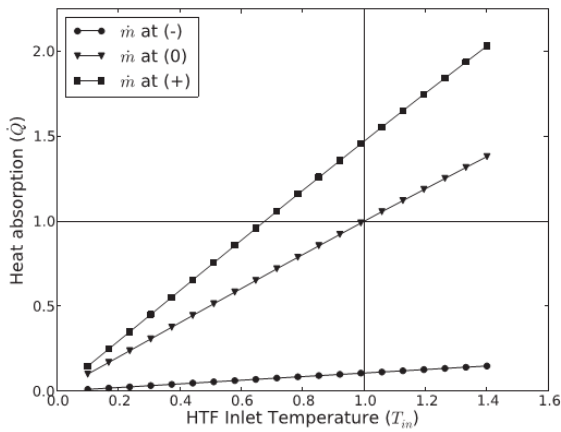
(c)
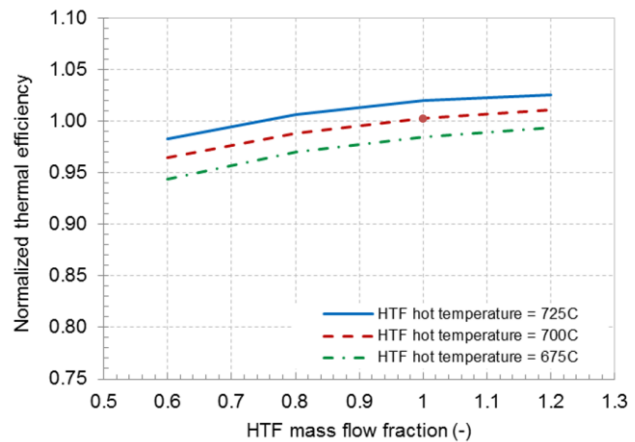
(d)

Figure 27: Off-design performance of the sub-critical Rankine cycle [89] and recompression s-CO₂ cycle.

The behavior shown in Figure 27 illustrates the performance drop of cycle power output as the HTF inlet temperature and mass flow rate vary simultaneously. Intuitively, HTF inlet temperature values lower than design-point decreases cycle power output – the importance lies in the

65

magnitude of the performance penalty. Similarly, HTF mass flow rate values lower than design-point are also detrimental, even more so than HTF inlet temperature would realistically drop.

Cooling system

Wet-cooling systems enable power plants to reject latent heat through evaporation, which is significantly more efficient than dry cooling, which rejects sensible heat to the dry-bulb temperature. Therefore, dry cooling systems require dramatically more heat transfer surface area to transfer an equivalent amount of heat and this translates to a larger, more expensive system. Because wet-cooling systems can cool to a much lower sink temperature (wet-bulb temperature), it enables greater conversion efficiency. However, the primary disadvantage of wet-cooling systems for thermoelectric power plants is the substantial water consumption via evaporation. They account for 41% of all fresh water withdrawals nationwide, making it the highest consumer of freshwater at approximately 139 billion gallons of water each day.

Dry cooling consumes virtually no water, which is especially noteworthy for potential CSP plant locations where water resources are scarce. Because CSP applications are generally installed in arid regions, a dry-cooled s-CO_2 recompression cycle is also investigated to evaluate the performance of systems where wet-cooled systems cannot be realized due to limited water availability. The trade-off between reduced thermodynamic performance and total plant water consumption is evaluated by calculating the heat rejection from the power cycle. The heat rejection is defined as:

66

$$\dot{q}_{rej} = \dot{W}_{out} \left(\frac{1}{\eta_{cycle}} - 1 \right) \qquad (3.23)$$

$$\dot{m}_{evap} = \frac{\dot{q}_{rej}}{\Delta h_{evap}} \qquad (3.24)$$

where enthalpy of evaporation is a function of ambient pressure (or temperature). The wet-cooling model assumes water consumption is through evaporation, and neglects blowdown and drift loss which are typically minimal. Parasitic load is also considered to be negligible based upon previous studies [91].

3.4.2 Regression Models

The power cycle technologies typically used in CSP applications are the Rankine and supercritical carbon dioxide (s-CO_2) Brayton cycles. The Rankine cycle is well understood and has been widely studied. The s-CO_2 cycle was initially developed for nuclear applications [83, 84], and have recently garnered attention for integration with CSP plants because of its relatively higher thermal efficiency, attractive fluid properties and reduced turbomachinery costs [85-88]. Previous efforts have modeled Rankine and s-CO_2 cycles using advanced power cycle models; however, the need to evaluate fluid properties of the working fluid generally is computationally expensive. Regression models dramatically reduce computing time, though special care must be taken to ensure accuracy and to avoid non-physical behavior.

This study adopts previously developed models for a sub-critical Rankine cycle and a recompression s-CO_2 cycle model to compare the performance of multiple system designs. Regression models for sub-critical steam Rankine cycle for both design point and part-load

67

performance are implemented, which enables the system model to consider the efficiency reduction for off-design conditions. This sliding pressure operation has been evaluated empirically by Biencinto [92] and Wagner [89] for steam Rankine cycles, and Seidel [78] for the s-CO_2 recompression cycle and each model is given in Table 7.

Table 7: Selected specifications of the power cycle models incorporated into the system-level model, with HTF temperature in Kelvin.

Power cycle	Normalized power output (-)	HTF outlet temperature (°C)	Cooling outlet temperature (°C)
Sub-critical Rankine (wet-cooled)	$\dot{W}_{out} = 4.00 \times 10^{-3} \cdot T_{HTF,in}$ -2.35×10^{0}	$T_{HTF,out} = 6.41 \times 10^{-2} \cdot T_{HTF,in}$ $+2.27 \times 10^{2}$	$T_{cw,out} = 8.98 \times 10^{-1} \cdot T_{HTF,in}$ -41.7×10^{1}
s-CO_2 (wet-cooled)	$\dot{W}_{out} = 1.53 \times 10^{-3} \cdot T_{HTF,in}$ -3.77×10^{-1}	$T_{HTF,out} = 9.27 \times 10^{-1} \cdot T_{HTF,in}$ -5.48×10^{1}	$T_{cw,out} = -1.98 \times 10^{-3} \cdot T_{HTF,in}$ $-1.21 \times 10^{-6} \cdot T_{HTF,in}^{2}$ $+3.08 \times 10^{2}$
s-CO_2 (dry-cooled)	$\dot{W}_{out} = 2.52 \times 10^{-3} \cdot T_{HTF,in}$ $-3.98 \times 10^{-7} \cdot T_{HTF,in}^{2}$ $+1.24 \times 10^{-1} \cdot T_{amb}$ $-2.22 \times 10^{-4} \cdot T_{amb}^{2}$ -1.80×10^{1}	$T_{HTF,out} = 9.46 \times 10^{-1} \cdot T_{HTF,in}$ -1.59×10^{3}	N/A

68

3.5 Operating Strategy

The operation strategy consists of different modes, and determines the net annual electricity production. While several variables can be controlled for plant operation, this study uses variable HTF mass flow rate to manage HTF temperature. This is also an important metric to control, specifically because operation outside of the tolerable range can cause degradation of the equipment or the fluid itself, in addition to other negative consequences. In addition, the mass flow rate also has an acceptable range, which causes the control strategy to differ between a clear or cloudy day. Annual weather data is utilized from the National Solar Radiation Database [81]. Following Eq. (3.5), when the solar irradiation is high enough for the calculated HTF mass flow rate to be above the minimum cut-off value, then the calculated value is adopted as the operating flow rate. If the thermal power output from the solar field exceeds the maximum allowable thermal input to the power block, the excess power is sent to the TES system if the state of charge allows. In this study, if the thermal power supplied by the solar field and TES is not sufficient to provide the design-point 100 MWe, the power block operates at part-load efficiency. The series of logical arguments for controlling plant operation are shown in Figure 28.

69

Calculate thermal input from SF
Calculate $\dot{m}_{HTF,calc}$ to achieve $T_{HTF,des}$

min $< \dot{m}_{HTF,calc} <$ max?

No — Yes

if $\dot{m}_{HTF,calc} < \dot{m}_{HTF,min}$

if $\dot{m}_{HTF,calc} > \dot{m}_{HTF,max}$

$\dot{m}_{HTF} = \dot{m}_{HTF,min}$
$T_{HTF,in} = T_{HTF,calc}$

$\dot{m}_{HTF} = \dot{m}_{HTF,max}$
$T_{HTF,in} = T_{HTF,des}$

$\dot{m}_{HTF} = \dot{m}_{HTF,calc}$
$T_{HTF,in} = T_{HTF,des}$

TES able to discharge?

TES able to charge?

TES able to discharge?

No — Yes | No — Yes | No — Yes

SF → PB | SF + TES → PB | SF → PB | SF + TES → PB | SF → PB | SF + TES → PB
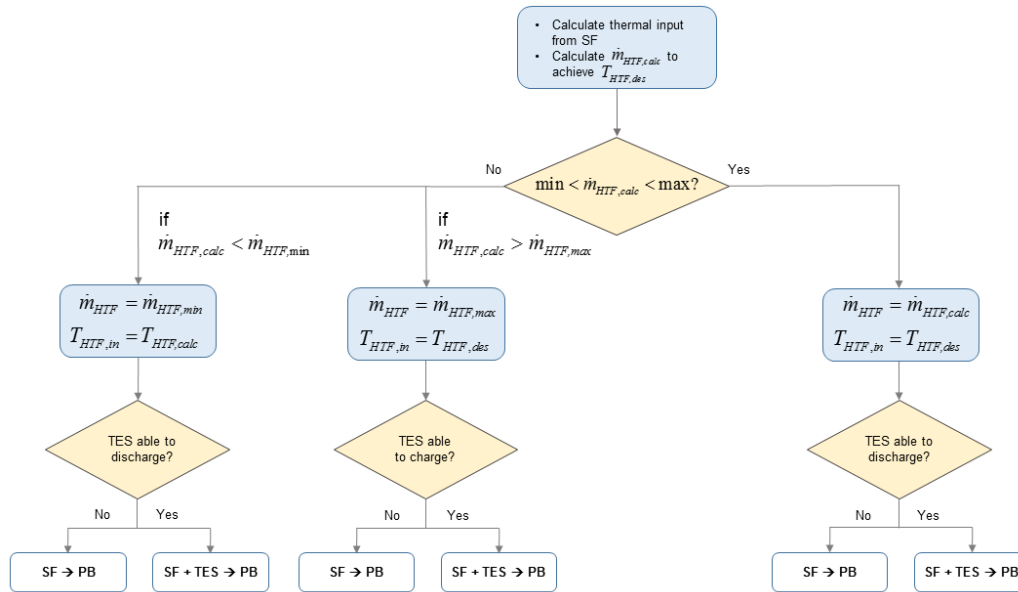
Figure 28: Operational strategy decision algorithm used to determine charging and discharging between solar field (SF), thermal energy storage (TES), and power block (PB).

It should be noted that DNI can fluctuate dramatically on a sub-hourly interval due to cloud cover, and the operational response and plant design will likely differ to handle these transient effects.

Table 8: Description of each operating mode, and the conditions that must be met.

Mode	Condition	Description
1	Calculated HTF mass flow rate from solar field is within design bounds, TES can be discharged	Power block operates from HTF supplied from solar field and/or TES
2	Calculated HTF mass flow rate from solar field is within design bounds, TES cannot be discharged	Power block operates from HTF supplied from solar field

3	Calculated HTF mass flow rate from solar field exceeds upper bound, TES can be charged	Power block operates at design-point, remainder of HTF flow charges TES, and/or solar field is partially defocused
4	Calculated HTF mass flow rate from solar field exceeds upper bound, TES cannot be charged	Power block operates at design-point, and solar field is partially defocused
5	Calculated HTF mass flow rate from solar field below lower bound, TES can be discharged	Power block operates from HTF supplies from solar field and TES
6	Calculated HTF mass flow rate from solar field below lower bound, TES cannot be discharged	Power block operates standby mode

3.6 Annual Simulation

The annual simulation is performed with 10-minute time steps using linear interpolation of the hourly weather data for a typical meteorological year (TMY3) for Daggett, CA. Several metrics for plant performance are evaluated to compare results. Firstly, it is straightforward to evaluate the annual net electricity output by computing the sum of the useful work produced by the power block of all 10-minute intervals. Also, by summing the total incident solar irradiation on the solar field, we can evaluate the energy and exergy efficiencies of the plant by computing the ratio of input energy (or exergy) to the total useful work produced.

Several checks are put in place to avoid unnecessary calculations, which improves numerical stability and computing time. During the night or times of little solar irradiation, the solar field HTF mass flow rate tends to infinity, and iteration of storage fluid properties can be reused from previous the time step while the state of the plant is relatively steady-state. Therefore, a minimum value of DNI is set to 50 W/m^2. Additionally, the model checks that the design-point power block

71

HTF mass flow rate is above the minimum solar field HTF flow rate. If not, then the model states that the solar multiple (or the reflective aperture area) is too large or the power block nameplate capacity is too small, and recommends a new plant sizing. Appendix A provides information about the model interfaces for each plant component.

3.6.1 Model Validation

Grid convergence for the TES model described in the previous section was conducted. The model was discretized with an axial length step of 2 cm and a time step of 10 s. The temperature distribution for a 50 node, 100 node, and 200 node system are shown in Figure 29.
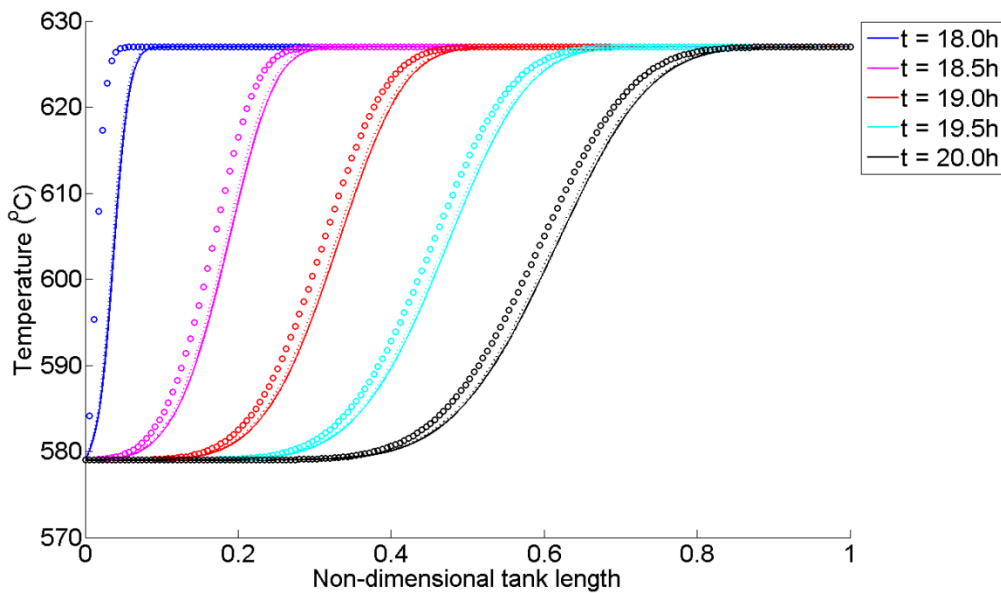
Figure 29: Grid convergence for the TES tank for a typical discharge, discretized with 50 nodes (circles), 100 nodes (dashed line), and 200 nodes (solid line).

72

The 50 node case agreed within 1.1% of the 200 node case with verified grid convergence. The temperature profile in Figure 29 for both cases show good agreement as well. The simulation requires little computational resources, and with this validation, is now extended to the system-level model in order to investigate TES performance integrated with other CSP plant components.

The results of the simulations are on a monthly or annual basis, in order to illustrate overall plant behavior and more clearly determine differences in performance. The model was validated using the System Advisor Model (SAM) developed by the National Renewable Energy Laboratory. The physical parabolic trough model was used, and sulfur properties were input for a user-defined storage fluid. Table 9 compares the monthly net energy output, which shows a maximum error of 8.87%. The single-tank model shows a comparatively slight overestimation of net energy produced, primarily due to SAM incorporating a different dispatch schedule and considering more comprehensive losses and parasitic loads for various CSP plant components. The majority of thermal losses are due to excess thermal energy dumped via defocusing. The values are compared in Figure 30 and show reasonable approximation.

Table 9: Comparison of monthly electricity production between system model and SAM. The models show a slight difference due to varying assumptions regarding thermal losses and parasitic loads.

	Monthly electricity production		Relative
	Single-tank model	**SAM with user-defined storage properties**	**error**
January	9568 MWh	8789 MWh	8.87%
April	13497 MWh	13101 MWh	3.02%
August	15959 MWh	15437 MWh	3.39%

73
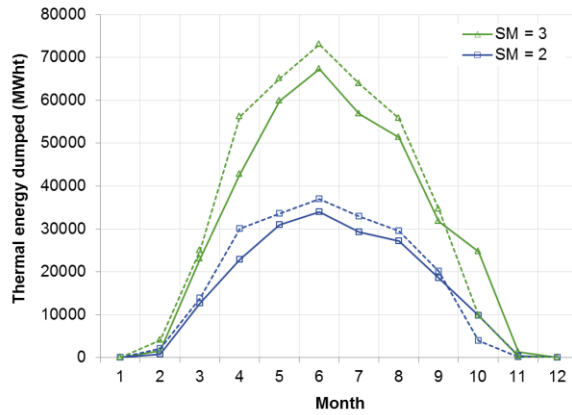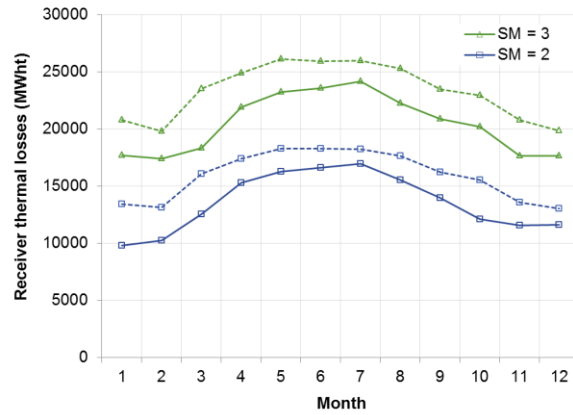
(a)   (b)

Figure 30: Validation of model (solid lines) with SAM (dashed lines) comparing (a) excess thermal power dumped via defocusing collectors and (b) receiver thermal losses.

From the baseline simulation in SAM, energy dumped due to defocusing and receiver heat loss accounted for 96% and 2% of the total thermal losses. For parasitic loads, the pumping energy required to pump the HTF through the solar field accounted for 76% of the total parasitic load requirement. Because these comprise the majority of parasitic loads and losses, the study incorporates these mechanisms while the remaining are not yet modeled.

As can be seen, the power absorbed by the solar field is highly influenced by the operating mode. It decreases with increasing HTF temperatures, which is reasonable since the heat losses of

74

the solar field increase under that condition. For constant design outlet temperature, which is assumed in the SAM model, the model matches well.

3.6.2 Performance Metrics

The overall performance of different CSP plant designs and configurations can be assessed with numerous performance metrics. The first-law efficiency and second-law (or exergy) efficiency, are widely used metrics and can be applied to subsystems or the overall CSP plant. The first-law efficiency measures the thermal losses of the system, and the second-law efficiency examines the reduction in exergy with respect to the dead-state condition. Capacity factor is the ratio of energy produced to the theoretical maximum if the power block was operating continuously at design-point. Capacity factor is defined as:

$$CF = \frac{\int_0^t \dot{W}_{PB,actual} \cdot dt}{\int_0^t \dot{W}_{PB,des} \cdot dt} \tag{3.25}$$

where the timescale is typically monthly or annually. By investigating these effects in an organized fashion, various plant designs can be compared upon equal footing.

3.6.3 Simulation Results

This section describes the annual simulation of system performance for different CSP plant designs. Specifically, we investigate different technologies across the solar field, TES, and power block subsystems. Also, TES systems employing different storage fluids are modeled on an annual basis to evaluate performance. Of all the organic fluid candidates, naphthalene showed the most promise as a storage medium, due to its relatively lower vapor pressure and higher specific heat and saturated liquid density compared to the other candidates. Based upon thermal cycling

75

experiments to observe long-term thermal decomposition, the maximum operating temperature of the storage fluid is set to 480°C. Therefore, naphthalene is modeled in a parabolic trough plant with an operating temperature of 290°C – 390°C.

Elemental sulfur also shows promise as a storage fluid. Because of its significantly lower vapor pressure, the TES system can utilize tubes with comparatively thinner wall thickness, thereby enabling a higher percentage of energy to be stored in the storage fluid itself, as opposed to the tube wall. Additionally, due to its excellent thermal stability at high temperature, it is modeled in a power tower plant with an operating temperature of 290°C – 579°C.

Figure 31 shows the average DNI values for each season in Daggett, CA. To compensate for the lower average DNI in fall and winter, plant designs typically increase solar multiple. However, this can lead to increased ″spillage″ in summer due to oversaturation of the power block during periods of high insolation. Integrating a TES system with sufficient capacity can balance this overdesign by allowing excess energy to be stored for later use.

76
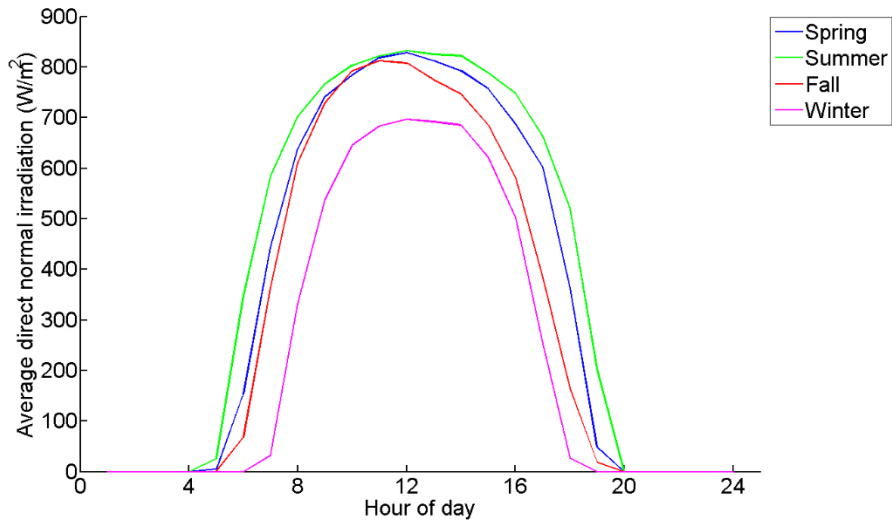
Figure 31: Hourly averaged direct normal irradiation for each season.

Spring
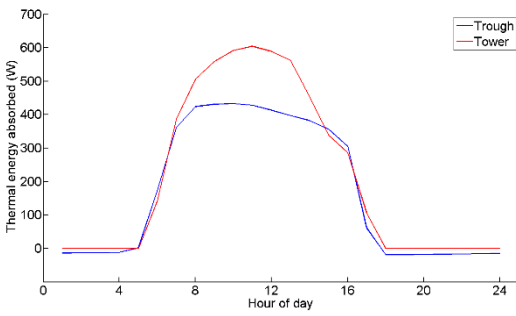
Summer
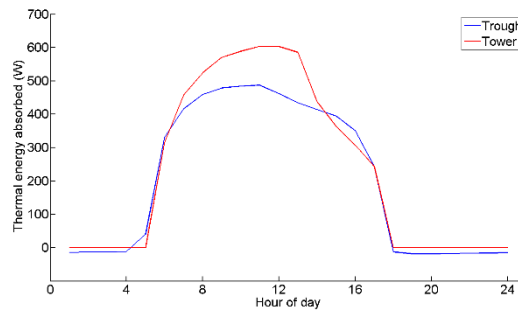
Fall
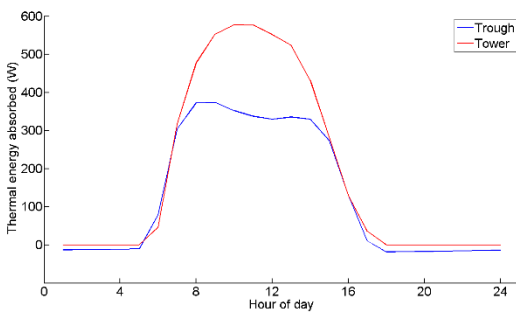
Winter
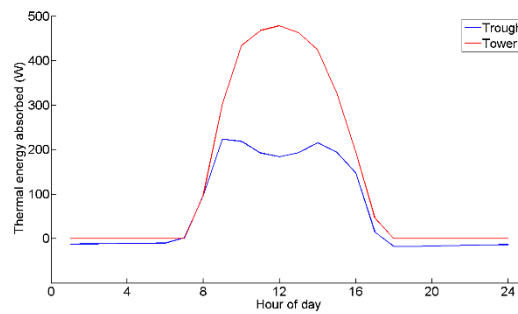
77

The total thermal power incident on the heliostat field, as well as subsequently absorbed by the receiver, is evaluated. By summing the electricity production across an annual basis, the annual thermal efficiency of the entire CSP plant can then be determined.

The temperature distribution of the TES system is shown in Figure 33. The conditions shown are for an initially fully charged TES tank during a typical nighttime discharge period with design-point HTF mass flow rate to operate the power block at full load.
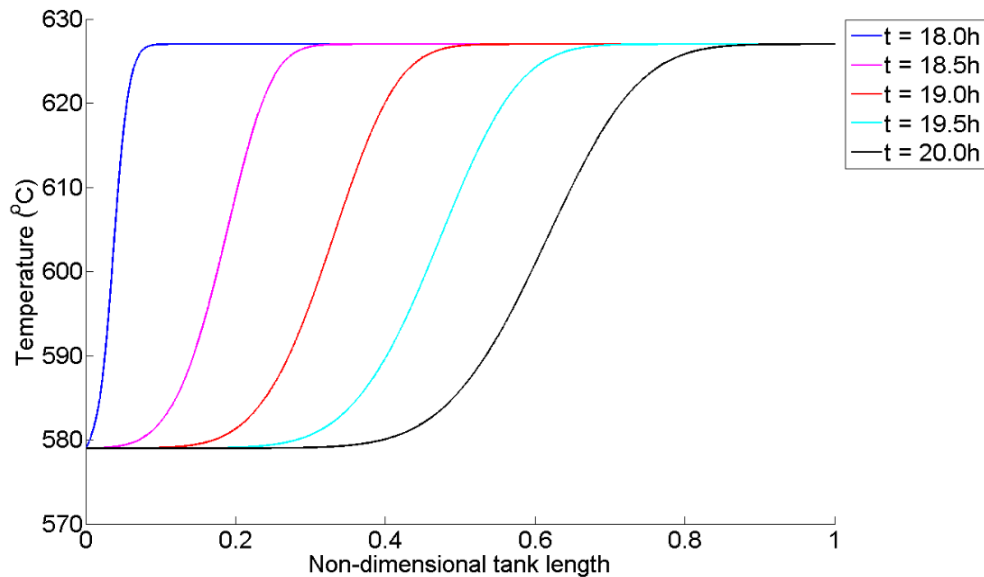
Figure 33: Temperature distribution for the elemental sulfur TES system during discharge for a typical day.

78

The results in Figure 33 reveal that the transient temperature distribution within the tank during the discharge period is sufficiently stratified. As the discharge period continues, thermal mixing begins to degrade the thermal stratification. However, this will be a function of the flow conditions and the initial condition of the TES system.

The temperature of the TES system at different tank locations during the entire day is illustrated in Figure 34. The charging and discharging periods are included and show the transient response of the TES system as thermal energy is stored and subsequently extracted.
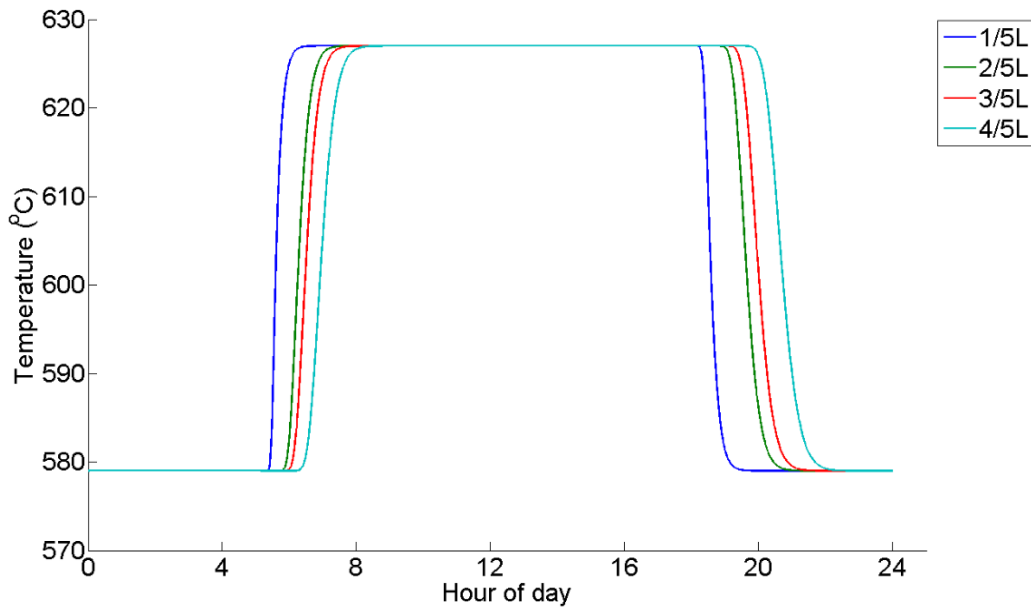
Figure 34: Temperature distribution for the elemental sulfur TES system during a typical summer day (June 30).

On summer days with high radiation, to obtain a useful energy output similar to a two-tank system, the thermocline tank should be fully charged, extracting completely the thermocline zone out of

79

the tank, followed by a full discharge. However, this strategy may not be possible in practice if the TES system outlet temperature is too high to drive the fluid to the solar field (SF) at the end of the charge process and too low to lead it to the power block (PB) at the end of the discharge.

Plant control is an important aspect of the CSP plant model, which ensures that each subsystem is operating within its allowable limits. The HTF temperature is another important metric that is controlled by Eq. (3.5) by varying HTF mass flow rate, to prevent damage to equipment or the fluid itself. Figure 35 displays the HTF mass flow rate to each subsystem during a typical day.
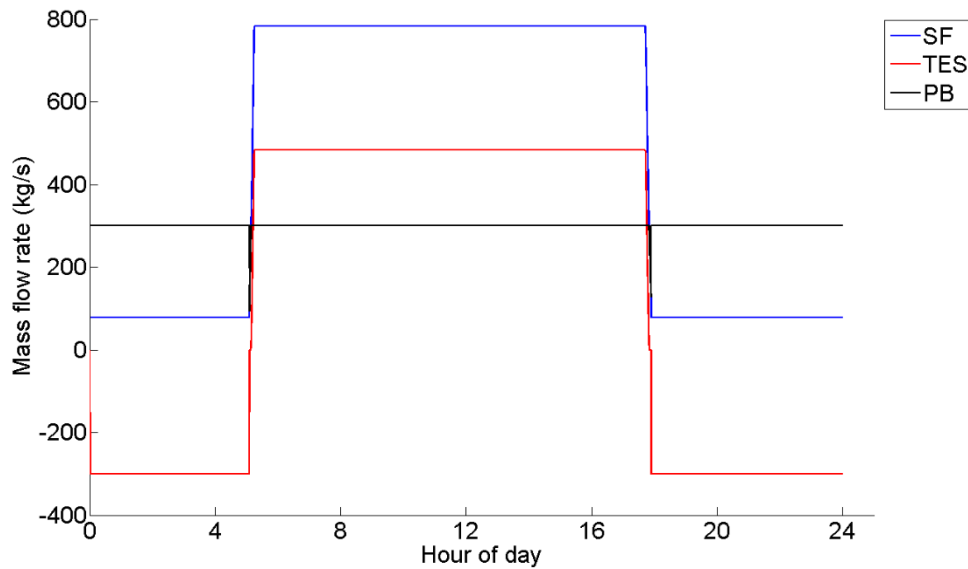
Figure 35: HTF mass flow rate through the solar field, TES, and power block system. Note that negative values for HTF mass flow rate through the TES denotes discharging, and positive values denote charging.

80

Thermal energy flow within the system is a primary metric to control, as a first measure to prevent damage and other negative consequences that can occur from operating outside the allowable limits of equipment across all subsystems. The thermal energy absorbed by the solar field and the power output from the power block for a few typical summer days is presented in Figure 36.
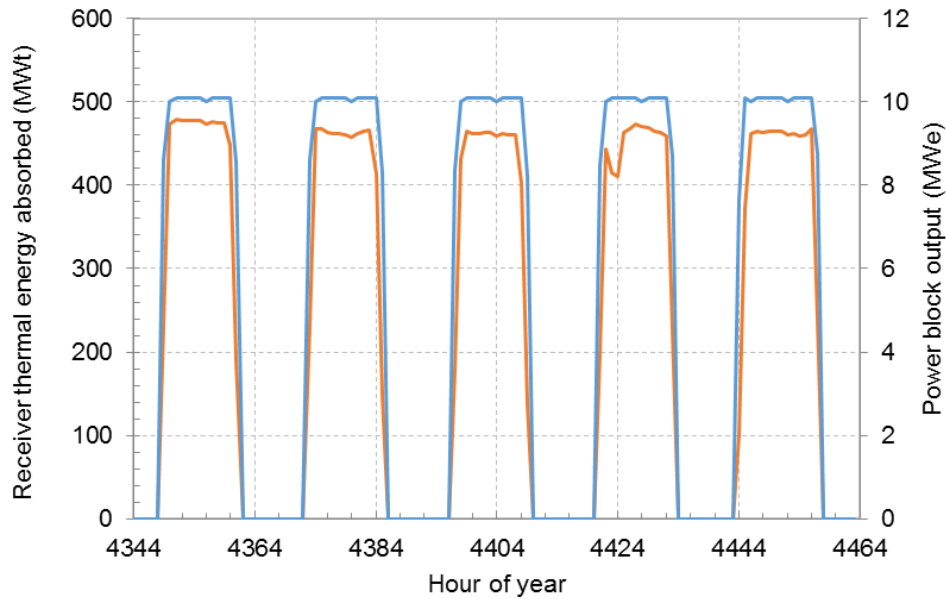
Figure 36: Thermal energy absorbed by the receiver (blue) and power block output (orange) for the baseline plant design integrated with a TES system employing elemental sulfur.

In the event of high DNI conditions with a fully charged TES system and the power block operating at design conditions, collectors are defocused to prevent overcharging of the TES system. The excess thermal power that is "dumped" is strongly dependent on the relative sizing of the solar field, TES, and power block.

Comparative studies must choose certain system design variables or outputs to hold constant to establish a fair comparison, such as solar field aperture area, plant cost, or net annual

81

electricity output. The current analysis keeps constant the energy storage capacity for all plant designs. Figure 37 presents the monthly capacity factor of TES configurations: one employing naphthalene as a storage fluid, and another employing elemental sulfur.
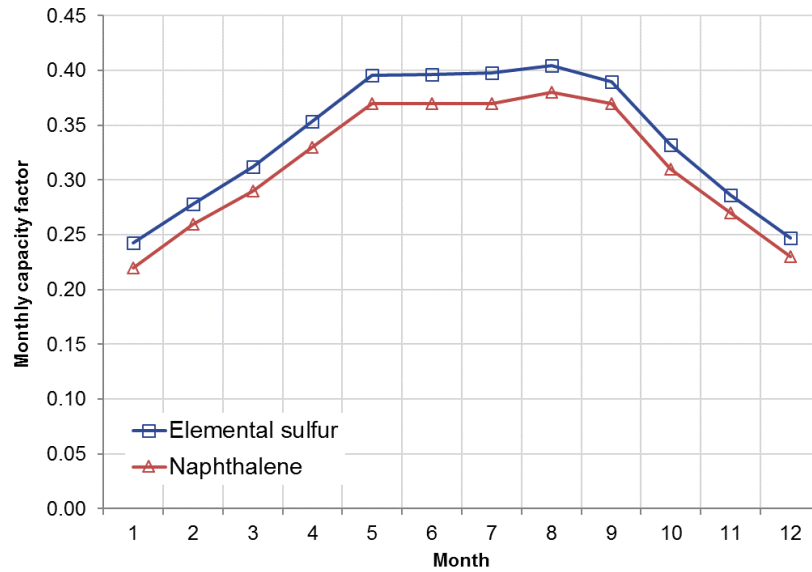
Figure 37: Comparison of monthly capacity factor for the CSP plant integrated with TES employing naphthalene or elemental sulfur as the storage fluid.

As previously mentioned, a user-specified energy storage capacity is the sole constraint. This is done so that each plant design has the same available dispatchable energy. The observation comes in how efficiently each case uses this energy. The results presented in Figure 37 show that elemental sulfur increases capacity factor substantially more than naphthalene. For the CSP plant integrated with a naphthalene TES system, the minimum and maximum monthly capacity factors are 22% and 38%, with an annual capacity factor is 31% for the baseline case. Similarly, the

82

minimum and maximum monthly capacity factors for the CSP plant integrated with an elemental sulfur TES system are 24% and 40%, with an annual capacity factor is 34% for the baseline case.

The next comparative study aims to compare the performance of the different power cycles detailed in Table 6. Each case is a power tower plant integrated with six hours of TES capacity with elemental sulfur as the storage fluid. Table 10 shows the annual simulation results for each plant design case.

Table 10: Annual performance metrics for different CSP plant designs.

Plant design	Annual electricity production (GWh$_e$)	Capacity factor	TES utilization factor	Annual thermal efficiency	Water usage (liters)
Sub-critical Rankine	38.0	42.1%	98.3%	32.1%	2.27×10^8
s-CO$_2$ (wet cooled)	44.5	44.3%	95.9%	36.2%	1.98×10^8
s-CO$_2$ (dry cooled)	42.5	43.1%	94.3%	35.6%	N/A

The results described in Table 10 illustrate some intuitive, yet worthwhile conclusions. Firstly, the CSP plant integrated with a sub-critical Rankine produces 10% and 14% less electricity on an annual basis than the s-CO$_2$ cycles with dry cooling and with wet cooling, respectively. Secondly, the sub-critical Rankine plant actually utilizes the TES system more often. The primary reason this occurs is because the sub-critical Rankine cycle requires more thermal input to produce the same amount of electricity. Because each case has equal solar multiple and nameplate power cycle

83

capacity (and therefore, absorbed thermal energy from the sun), the power cycle requires energy from the TES system more often to operate at design-point value. Restated, both of the s-CO_2 plant designs underutilize the TES system and can be built with a smaller capacity. Thirdly, both of the plant designs employing wet cooling consume a substantial amount of water, and the difference between them is minimal. The s-CO_2 cycle with dry cooling simultaneously saves dramatically more water while producing more electricity on an annual basis than the sub-critical Rankine cycle. However, the trade-off between the s-CO_2 cycle with dry cooling versus wet cooling is more nuanced, and no immediate conclusions can be drawn from this analysis. The value of both water and electricity varies greatly on geographic location, available resources, and current energy policies.

The results of the annual simulations presented in this chapter show that the novel storage fluids, such as naphthalene and elemental sulfur, show promise to increase performance of CSP plants from a technical standpoint. The thermal gradient of the TES system, as well as the thermal behavior of the solar field and power block, were validated using grid convergence and existing models developed by NREL, respectively. The TES systems are designed to provide a specific capacity to operate the power block at full-load operation, similar to existing molten salt TES systems, and therefore the power produced and capacity factor is nearly equivalent as expected. However, distinctions are drawn in Chapter 5, which investigates the economic viability of the TES systems under study compared to the state-of-the-art molten salt TES systems.

Chapter 4

Exergy Analysis of the TES System

4.1 Governing Equations

The Second Law of Thermodynamics introduces concepts of exergy and entropy, which is very distinct from the First Law. Therefore, the analysis based on the Second Law will be established to clearly understand the approach taken with a tandem analysis. This section provides an overview of the concepts of exergy and entropy and their roles. The Second Law of Thermodynamics, unlike the First Law, distinguishes the quality of energy of a system. The quality of energy is determined from the deviation from the 'dead state', which is typically the surrounding condition. This quality of energy is called "exergy", but is also known as useful work, availability, available energy, essergy, etc. in various literature. Here, we will utilize the term "exergy" henceforth, and therefore the analysis based on the Second Law of Thermodynamics will be called exergy analysis. Exergy is the maximum quantity of work that a system can produce as it reaches equilibrium with the dead state. Simply, exergy is the potential of the system due to its non-equilibrium condition in relation to its surroundings, which can be categorized as shown in Figure 38.

Exergy		

Physical		Chemical

Mechanical		Thermodynamic

Kinetic	Potential	Temperature	Pressure	Chemical	Mixing
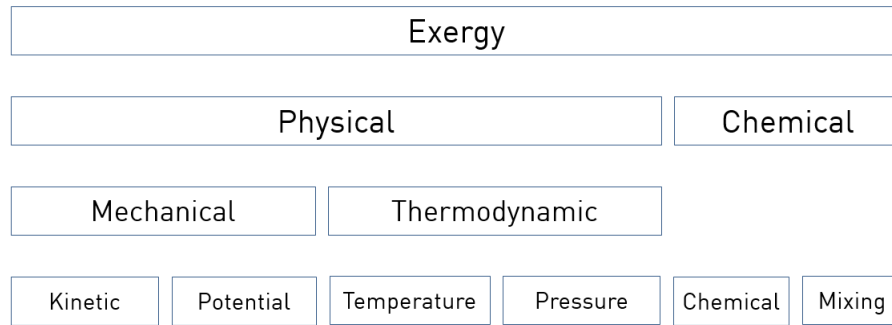
Figure 38: Exergy can be classified into various categories.

Exergy analysis provides a valuable means, in tandem with energy analysis, of assessing TES systems. Once equilibrium is reached, then the exergy of the system is zero. This is the fundamental difference between energy and exergy analysis: exergy is not conserved, and is in fact destroyed. In other words, this explains that energy can be degraded, or lose quality. Specifically, exergy analysis illuminates how closely actual performance approaches the ideal case, which produces a meaningful efficiency parameter. By illustrating the cause and location of thermodynamic losses, exergy analysis identifies opportunities for performance enhancement and system optimization.

In fact, the utility of exergy methods is becoming more widely recognized in recent years. There have been many studies that utilize exergy analysis for TES performance evaluation, including PCM systems [93-102], sensible heat storage [75, 93, 97, 101, 103, 104], thermochemical systems [26, 105, 106], and industrial applications [99, 102, 107-110]. However, there exists a wide range of approaches, and some have concluded that a conventional measure is required in order to fairly assess TES performance [4, 111, 112]. The rationale is that the energy efficiency of a TES system has remained the primary metric for overall performance, but can be

an inadequate measure because it does not take into account all considerations necessary in TES evaluation (e.g. temperatures of the supplied and recovered energy, storage duration, and how nearly the system approaches ideal performance). Naturally, the Carnot efficiency plays a role in determining the optimal design for the TES system.
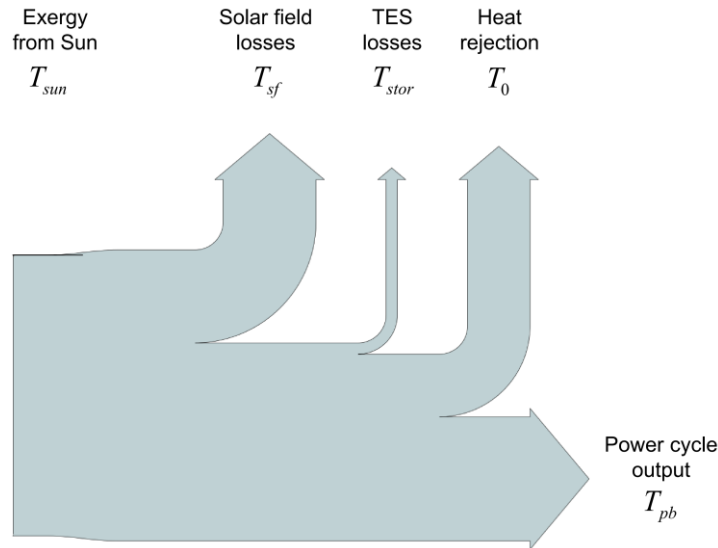
Figure 39: Diagram of operating temperatures at various locations of the CSP system.

The coupling of the various operating temperatures for each component leads to an optimal set of values that ensures maximum power output and minimum heat loss [113]. Moreover, the TES temperature should also be added into the coupling, and can be modelled similarly. A closed-form solution will be developed to determine the optimal temperature that balances increasing heat loss with improved Carnot efficiency.

In this study, tube cylinders are selected as the geometry due to tank design considerations, and ease of manufacturing. However, as pointed out by Dincer and Rosen [4], from an exergetic

87

standpoint, the geometry of the tank design must also balance trade-offs between fluid mechanics and heat transfer considerations. For example, the use of encapsulated spheres in packed beds will allow the HTF to flow through with a smaller pressure drop due to its aerodynamic shape, but will lead to reduced heat transfer due to its smaller surface area to volume ratio (a cube will have the opposite trade-off). Dincer and Rosen concluded that cylinders serve as a balance between the two – able to lessen pressure drop appreciably, while also maintaining a sufficient heat transfer surface area.
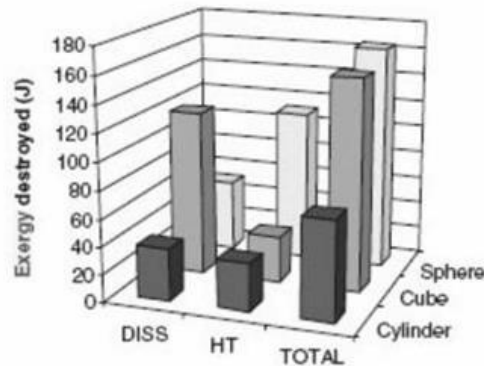
Figure 40: Exergy destruction via pressure drop (DISS) and heat transfer (HT) for a PCM

system [4].

Consider a control volume (CV) surrounding the TES tank, defined individually for the charging and discharging period, as shown in Figure 41. For both cases, only one inlet and outlet is considered. This simplifies exergy analysis by investigating the exergy destruction across the tank (and in the discharge period, the bypass loop as well), as opposed to determining the exergy destruction via heat transfer at each interface within the tank, i.e. at the storage-fluid-tube-wall interface, and the tube-wall-HTF interface.

88
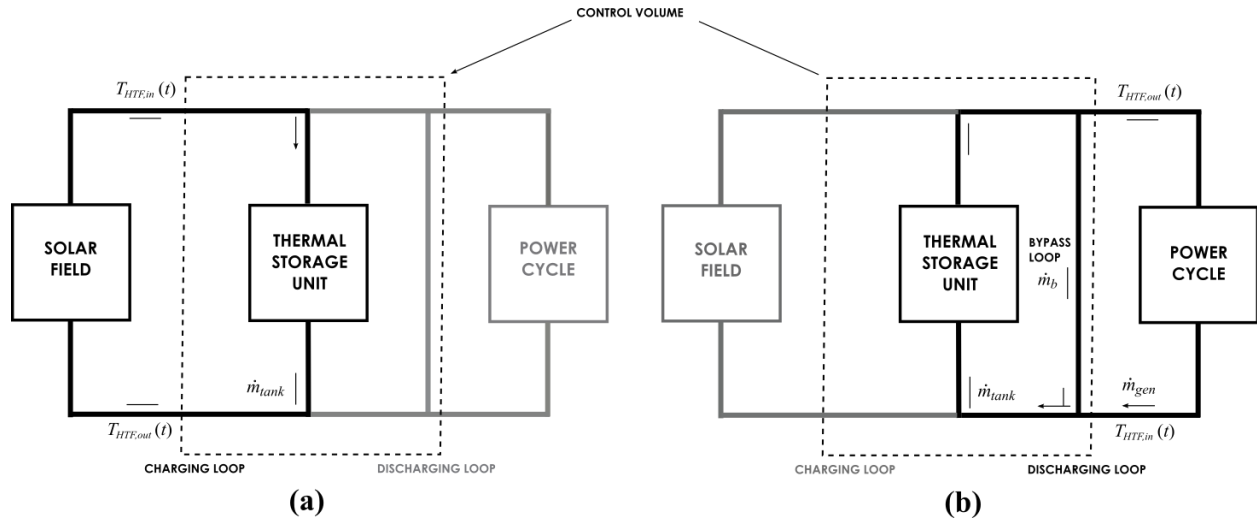
Figure 41: CV of the TES system for exergy analysis during a) charging and b) discharging.

The exergy supplied to and recovered from the TES tank can be evaluated solely from consideration of the inlet and exit conditions of the HTF. The exergy supplied to the TES tank during the charging period, assuming an incompressible fluid with constant specific heat and equivalent pressure states at the inlet and outlet due to the presence of the pump, can be expressed as

Rate of exergy stored during the charging period:

$$\dot{Ex}_{\text{charge}} = \dot{m}_{HTF} c_{HTF} \left[\left(T_{HTF,in} - T_{HTF,\text{out}} \right) - T_0 \ln\left(\frac{T_{HTF,in}}{T_{HTF,\text{out}}} \right) \right] \tag{4.1}$$

Rate of exergy recovered during the discharging period:

89

$$\dot{Ex}_{\text{discharge}} = \dot{m}_{HTF} c_{HTF} \left[\left(T_{HTF,\text{out}} - T_{HTF,\text{in}} \right) - T_0 \ln \left(\frac{T_{HTF,\text{out}}}{T_{HTF,\text{in}}} \right) \right] \qquad (4.2)$$

It should be noted that the control volume, as it is defined, captures the exergy destruction due to a finite temperature difference. In other words, exergy input is characterized by the inlet HTF temperature, and some is transferred to the storage fluid through a finite temperature difference, while some is destroyed in the heat transfer process (we'll get to the other mechanisms in the following section). Therefore, the exergy destruction due to heat transfer will manifest itself in the outlet HTF temperature. Then, it becomes straightforward to evaluate a second-law, or exergetic, efficiency, which will be described later in this chapter. However, one of the primary benefits of a second-law analysis is the identification of the mechanisms of exergy destruction, which informs opportunities for system-level performance enhancement. The various exergy destruction mechanisms are outlined in the following section.

4.1.1 Exergy Destruction Mechanisms

Next, the heat loss for a non-adiabatic TES system at a given time step can be determined by defining an overall heat transfer coefficient U, based on an outer shell surface area A_{shell}:

$$Q_{loss} = U A_{shell} \left(T_{stor,avg} - T_0 \right) \Delta t \qquad (4.3)$$

From an exergy standpoint, the 'quality' of the heat loss in comparison to ambient conditions is taken into account for a non-adiabatic case [4]:

$$Ex_{loss} = \dot{Q}_{loss} \left(1 - \frac{T_0}{T_{stor,avg}} \right) \qquad (4.4)$$

90

Accounting for pressure losses in both energy and exergy analyses of TES systems can be complicated to calculate if design geometry is not known. Pump work is often neglected due to this, but in many cases, it has been shown to be a significant energy cost and must be considered [114, 115]. Additionally, it has been demonstrated that the pressure loss is more pronounced in exergy analysis [112, 114].

Table 11: Various research efforts in exergetic analyses of TES systems.

Operation	Pressure drop irreversibility	Reference
Discharging	Unaccounted for	Strub 2000
Discharging	Unaccounted for	Erek, Dincer 2008
Charging	Unaccounted for	Kousksou 2007
Charging	Unaccounted for	Strub 1999
Charging	Accounted for	Kouskou 2008
Entire cycle	Accounted for	Domanski 1996
Entire cycle	Accounted for	Charach 1993

Naturally, each TES system will account for pressure losses differently based on respective tank geometry, flow regime, etc. For PCM systems utilizing shell-and-tube exchangers, several studies have adopted Kern's Method [116], or the Bell-Delaware Method [117]. Moreover, varying assumptions can be made in respective analyses to simplify the model for versatility. For a sensible storage system utilizing a heat exchanger, Krane approximated pressure drop using flow past a tube [115]. In this analysis, a typical design geometry of the TES tank is given and the pressure

91

loss is modeled accurately as crossflow over a large tube bank. An illustrative diagram is shown in Figure 42.
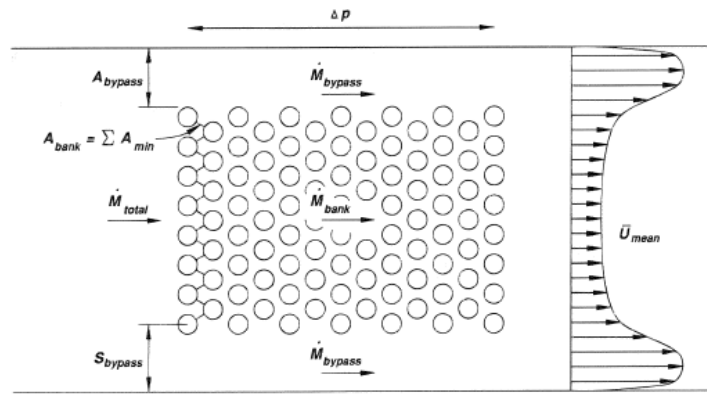
Figure 42: Diagram of pressure drop mechanisms for a large tube bank [118].

From [119], the tube row configuration can either be staggered or aligned relative to the incoming fluid as shown in Figure 43. The relevant parameters are the tube diameter, and the transverse pitch S_T and longitudinal pitch S_L which are measured between tube centers.

92

(a)   (b)
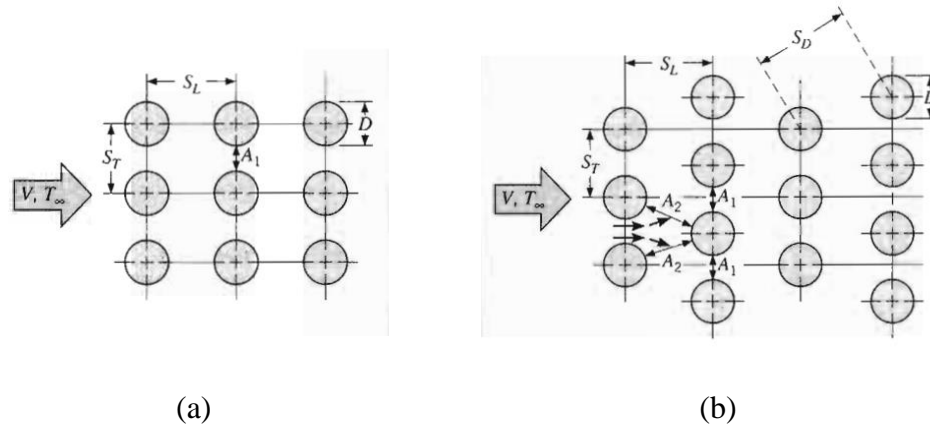
Figure 43: Tube row configuration with relevant parameters for a) aligned and b) staggered

configurations [119].

For this analysis, we will assume a staggered configuration with the number of tube rows N_L. Then

the pressure drop across the tube bank is given by

$$\Delta p = N_L \chi \left(\frac{\rho V_{max}^2}{2} \right) f \qquad (4.5)$$

where f is the friction factor, and χ is the correction factor; both are given in charts provided by

[119] and shown below.
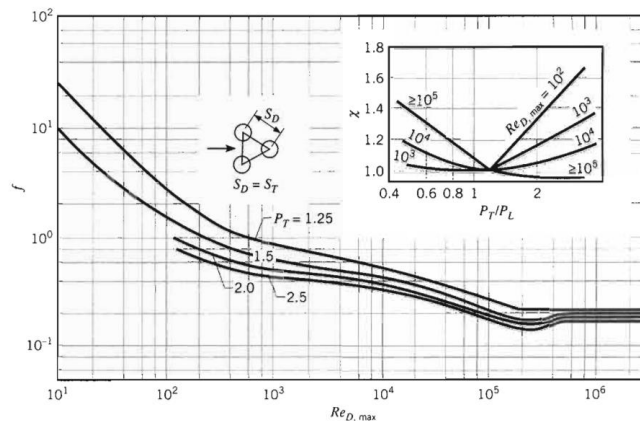
Figure 44: Friction factor and correction factor as a function of Reynolds number [119].

93

Then, the pump work required to overcome viscous effects is written as

$$W_{pump} = \frac{m\Delta p}{\rho \eta} \qquad (4.6)$$

where this is both an energy and exergy cost. This is because exergy is defined as "useful work" [115, 120]; in the governing principle, work done to the system is equivalent in both the first and second law analyses [112, 114, 121].

Exergy destruction due to pressure losses

Pressure losses in both energy and exergy analyses of TES systems cannot be evaluated accurately if design geometry is not known or is not within the scope of work. Pump work is often neglected in part because of this, but in many cases, it has been shown to be a significant energy cost and is an important consideration [114, 115]. Additionally, it has been demonstrated that the pressure loss has a greater effect in exergy analysis [112, 114].

Exergetic efficiency can be defined in a number of ways, depending on the system under study, scope of work, and general approach [98, 111, 122]. Jegadheeswaran [98] compiled exergetic efficiencies used in various TES studies to illustrate the different approaches taken in exergy analyses of TES systems, and the author has added other definitions encountered in the literature as well.

Table 12: Various definitions of exergetic efficiencies, adapted from [98].

Exergetic efficiency	Expression	Description	Reference
Charging	1. $\dfrac{Ex_{stored}}{Ex_{HTF}}$	Presents total exergy stored out of supplied	[123]
	2. $\dfrac{\dot{Ex}_{stored}}{Ex_{HTF}}$	Presents temporal variation of exergetic efficiency	[124]
	3. $\dfrac{Ex_{stored}}{Ex_{HTF} + Pump\,work}$	Acccounts for pump work	[125]
	4. $\dfrac{Ex_{stored}}{Ex_{HTF}}$	Presents total exergy recovered out of supplied	[126], [127]
Discharging	1. $\dfrac{Ex_{HTF}}{Ex_{PCM,init}}$	Presents total exergy recovered out of supplied from PCM	[123]
	2. $\dfrac{\dot{Ex}_{HTF}}{Ex_{PCM}}$	Presents maximum exergy recovered out of supplied from PCM	[101], [126]
Overall	1. $\dfrac{Ex_{recovered}}{Ex_{supplied}}$	Presents total exergy recovered from supplied	[101]
	2. $\psi_{charge}\psi_{discharge}$	Presents separate efficiencies for charging and discharging	[128], [129]
	3. $1 - N_S$	Presents the quantity of exergy destroyed	[130]

In this work, the analysis of a full working cycle allows exergetic efficiency to be expressed as

95

$$\psi = \frac{\int_{t_{charge}}^{t_{discharge}} (\dot{m}c)_{HTF} \left[T_{HTF,out}(t) - T_{gen,out} - T_0 \ln\left(\frac{T_{HTF,out}(t)}{T_{gen,out}} \right) \right] dt - E_{pump}}{\int_0^{t_{charge}} (\dot{m}c)_{HTF} \left[T_{sol,out} - T_{HTF,in}(t) - T_0 \ln\left(\frac{T_{sol,out}}{T_{HTF,in}(t)} \right) \right] dt} \qquad (4.7)$$

where t_{charge} and $t_{discharge}$ are the charge and discharge time, respectively, and E_{pump} is the pumping energy during a full charge-discharge cycle. The pump consumption is equivalent to the irreversibility, or exergy destruction, due to pressure drop within the system, in addition to the non-isentropic nature of the pump.

The subsequent section of the study is the investigation of several parameters on system performance. The effects of charging mass flow rate, tube bundle geometry, and storage and yield temperature are studied and described in detail in the next section.

4.2 Parametric Studies

Next, the impact of storage fluid loading is evaluated. Varying the storage fluid loading corresponds to traversing the *P-v* diagram across different phase regimes. Higher storage fluid loading is beneficial because it corresponds to larger energy storage density, i.e. the required thermal energy can be stored in a smaller volume. However, increasing storage fluid loading also has the negative impact of increasing maximum system pressure (holding maximum temperature fixed); this impacts either the tube radius, or the number of tubes needed to meet the energy storage capacity requirement.

96
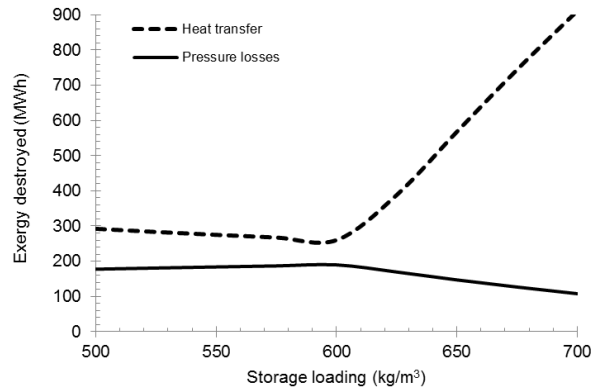
Figure 45: Effect of storage fluid loading on exergy destruction.

Figure 45 illustrates the effect of storage fluid loading on exergetic performance. The variation of storage fluid loading directly dictates the phase of the storage fluid during operation. Higher storage fluid loading leads to higher energy density, but at the expense of higher pressure. Therefore, it is clear that there is an optimum storage fluid loading that balances these competing effects. For the system under study, closer inspection reveals that operating between saturated liquid and two-phase mixture is the optimal loading. Intuitively, this makes sense because sub-cooled liquid results in higher pressures which necessitates a larger tube radius (increased exergy destroyed due to heat transfer), while operating in the liquid-vapor phase with constant pressure does not yield any appreciable benefits in thermophysical properties.

As mentioned previously, the results shown thus far assume an operation mode that achieves constant inlet HTF temperature by varying the HTF mass flow rate. The following parametric study investigates the alternative operation mode of constant HTF mass flow rate with varying inlet HTF temperature (this will be re-examined in the following section). In Figure 46,

97

the transient behavior at different locations in the charging loop is presented for varying mass flow rate. The results of Figure 46 illustrate the competing effects that must be balanced.

(a) $\dot{m}_{HTF} = 400 \, kg/s$

(b) $\dot{m}_{HTF} = 600 \, kg/s$

(c) $\dot{m}_{HTF} = 800 \, kg/s$
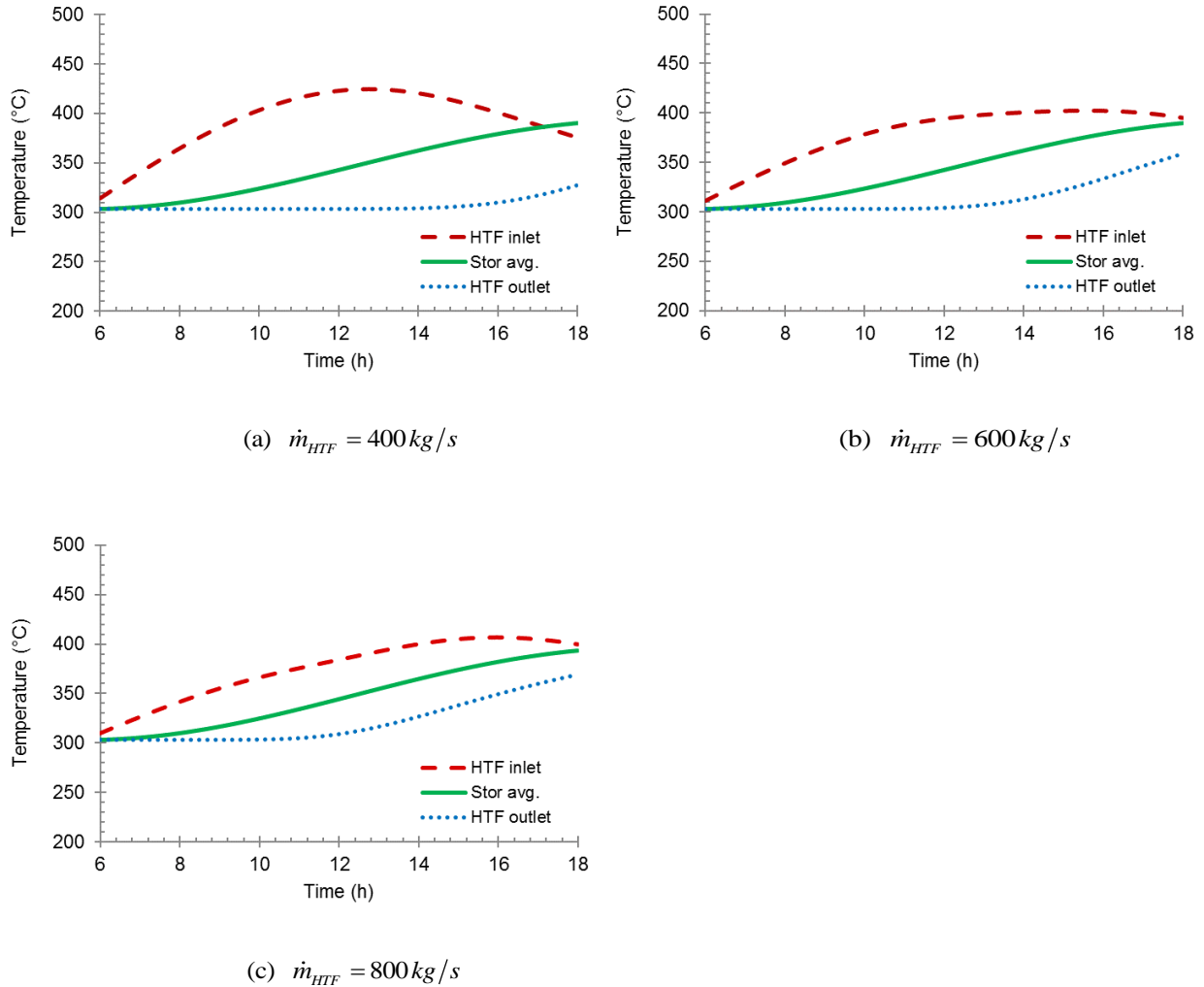
Figure 46: The transient behavior of the TES tank during the charging period, for different cases with increasing HTF mass flow rate.

As mentioned previously, based on the defined control volume (i.e. around the TES tank), exergy destroyed through the thermal interaction between the HTF and storage fluid inside the tank will exhibit its overall effect in the outlet HTF temperature. Therefore, we observe that the difference

98

between the inlet and outlet HTF temperature must be minimized because it dictates the exergy destroyed through this mechanism. This is primarily achieved by increasing mass flow rate, which can be seen in Figure 46; similar results have been presented by Erek and Dincer [96, 131] and by Mawire et al. [103]. However, the increase in mass flow rate clearly results in higher pressure drop and thus, higher exergy destroyed due to viscous effects. The total exergy destroyed will then observe a minimum by balancing this trade-off that occurs for varying mass flow rate.

It becomes clear that these parameters are fundamental to plant operation and warrant detailed investigation (i.e. the HTF exiting the solar field must not exceed a given temperature for thermal stability purposes, and the mass flow rate must not exceed a value for pump work to be reasonable). The results of varying mass flow rate on total exergy destruction and exergetic efficiency will be illustrated in detail in the following section.

It should be noted that balancing exergy destruction associated with heat transfer and with pressure drop is also dependent on many design geometry parameters, such as baffle spacing, tube radius, tube or tank length, and tube pitch among others. To investigate the optimum design geometry in the system under study, tube pitch and tube radius are selected as representative variables for the design geometry space, while other parameters, such as baffle spacing and cut, are taken from nominal values in heat exchanger design [118, 132]. Similar TES systems have also been studied to optimize encapsulated tubes and sphere size and spacing to balance pressure losses with adequate heat transfer behavior. Several studies for packed beds reported that increasing the radius of the storage fluid lessens the pressure drop, but thermal performance of the system declines due to lower surface area available for heat transfer [20, 133]. The system under study is also subject to this trade-off. The influence of tube radius is shown in Figure 47.

99
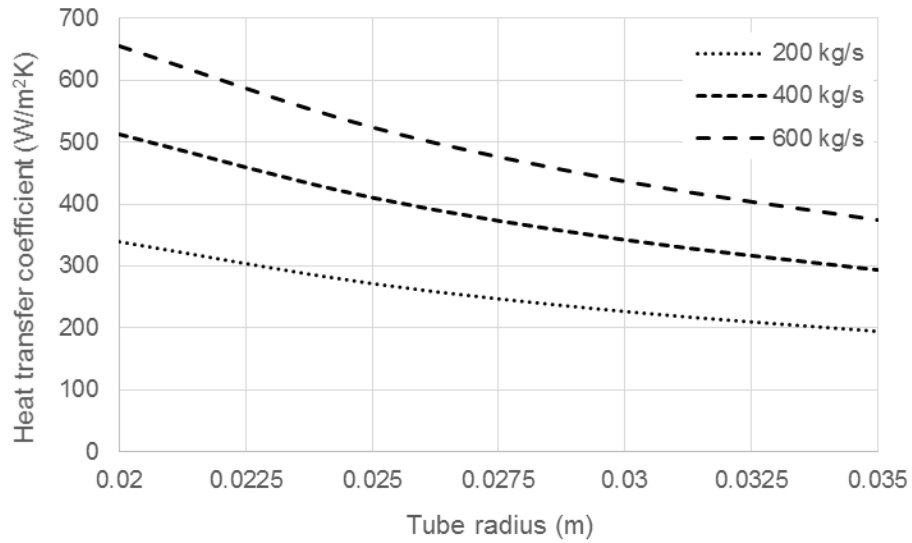
(a)
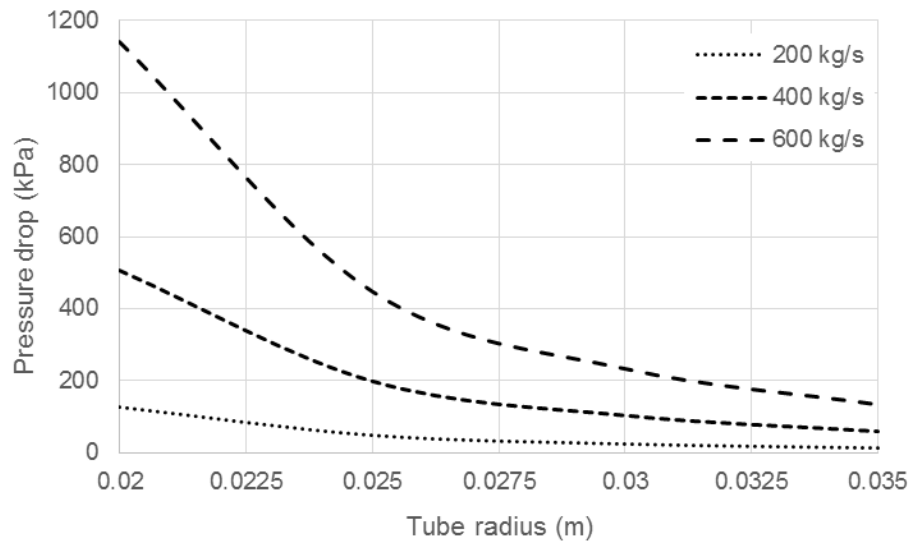
(b)

Figure 47: Effect of tube radius on heat transfer coefficient and pressure drop.

100

The effect of varying tube radius is much more dramatic for pressure drop than for heat transfer coefficient. One particular reason is the high thermal conductivity of the tube wall material, which effectively makes the thermal resistance impervious to changes in the tube radius-to-length aspect ratio. Additionally, for a constant tube pitch with larger tubes, this translates to a higher number of transfer units in series and effectively lengthens the path of the HTF as it flows through the TES system.
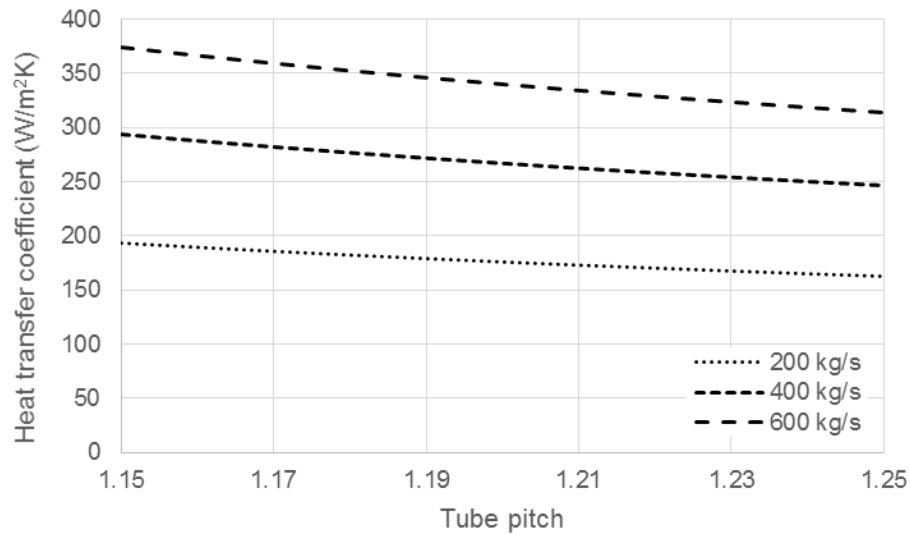
(a)
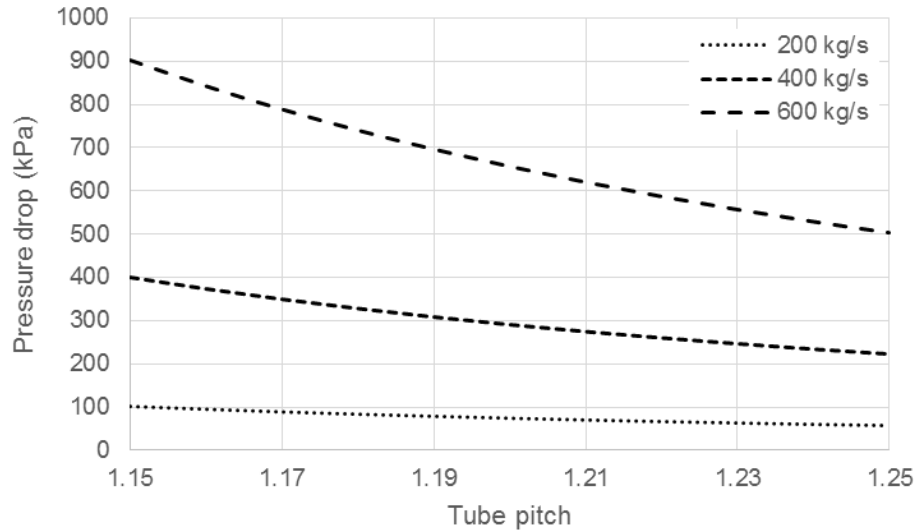
(b)

Figure 48: Effect of tube pitch on heat transfer coefficient and pressure drop.

The results of varying tube pitch are shown in Figure 48, which indicate that pressure drop varies more markedly than the heat transfer coefficient as tube pitch decreases, similar to the results reported for the parametric study of baffle spacing [134]. The tube pitch is constrained to a design window to maintain a feasible tank volume, as well as ensure that the transient heat transfer behavior is sufficient enough to allow for a reasonable charge and discharge time. These values are informed from the heat exchanger design [118].

Ambient temperature is another parameter that has a fundamental influence on exergy analysis, as it defines the dead state condition, and it varies greatly throughout the year. Most notably, it serves as the heat sink temperature for the cooling system of the power cycle, which strongly dictates its design-point and off-design performance. Specifically, the design-point

ambient temperature is significant because it defines a design-point thermal conductance for the cycle as described in Section 3.5.1.

To isolate and evaluate its impact on an annual basis, hourly DNI and ambient temperature data can be incorporated into the analysis by using a probability distribution function (PDF) to quantify the probability of achieving performance or cost targets. The PDF of the ambient temperature and DNI weighted ambient temperature compiled for Daggett, CA is shown in Figure 49. The DNI weighted ambient temperature probabilities represent more realistic conditions for CSP power cycle operation, as current conventional wisdom expects CSP plants generate electricity during peak pricing periods rather than operate as baseload plants. Note that, as expected, the DNI weighted probabilities are shifted towards warmer temperatures.

Ambient temperature (°C)	Ambient temperature-weighted probability	DNI-weighted probability
-7.5°C	0.02%	0.00%
-2.5°C	0.78%	0.05%
2.5°C	4.45%	0.87%
7.5°C	12.80%	4.50%
12.5°C	17.47%	11.72%
17.5°C	17.67%	16.54%
22.5°C	16.34%	18.17%
27.5°C	14.42%	18.55%
32.5°C	9.26%	14.83%
37.5°C	5.76%	12.35%
42.5°C	1.04%	2.42%
Average annual temperature (°C)	19.5°C	24.3°C
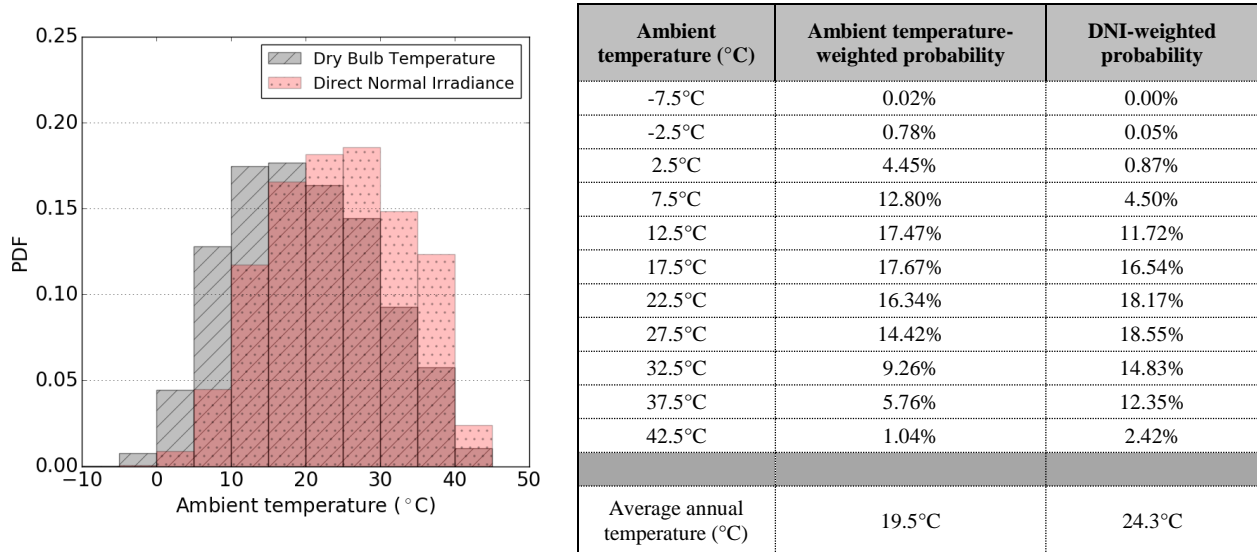
Figure 49: Probability density function of ambient temperature-weighted and direct normal irradiance-weighted probability, with a table of probability values located at the midpoint of each bin using TMY2 weather data for Daggett, CA.

103

Then, based upon the probability distribution that the power cycle will experience a varying ambient temperature throughout the year, we can assess annual performance by combining the modeled off-design efficiency at each temperature with its associated probability.

For the steam Rankine cycle model developed by Wagner, relative cycle performance drops by 7.5% with an increase in 20°C ambient temperature change using a wet-cooling system. For the s-CO_2 cycle using dry-cooling, the impact is expected to be more much pronounced as described in Section 3.4.1 [77]. A parametric study of ambient temperature on the performance of the baseline s-CO_2 cycle design, described in Table 6, is conducted. The baseline cycle is designed for 20°C ambient temperature, with the compressor inlet temperature defined as 15°C warmer, which assumes the cooling system maintains a constant temperature differential. Two additional cycle designs are being considered with a design-point of 25°C and 30°C for ambient temperature, respectively, to simultaneously observe the trade-off between designing a cycle with higher design-point efficiency, yet is more susceptible to steeper performance drop during off-design conditions. More detailed design parameters are included in Appendix C. To put both designs on equal footing, they maintain the same heat exchanger thermal conductance as the baseline design. The results are presented in Table 13.

Table 13: Results of the probabilistic modeling for s-CO_2 off-design performance using DNI-weighted dry-bulb temperature from Daggett, CA, with design-point efficiencies denoted by (*).

Ambient temperature (°C)	Design-point Thermal Efficiency

	Ambient temperature 20°C (51.4%*)	Ambient temperature 25°C (49.6%*)	Ambient temperature 30°C (48.0%*)
-10°C – 15°C	52.6%	51.6%	50.6%
17.5°C	52.2%	51.3%	50.3%
22.5°C	51.0%	50.3%	49.4%
27.5°C	48.1%	49.2%	48.6%
32.5°C	46.4%	47.8%	47.9%
37.5°C	44.6%	46.8%	46.9%
42.5°C	42.8%	45.9%	46.0%
Annual parameters			
Ambient temperature-weighted annual efficiency (-)	50.5%	50.3%	49.5%
Direct normal irradiance-weighted annual efficiency (-)	49.3%	49.6%	48.9%

The results observed in Table 13 support and expand upon the results of both the design-point and off-design analysis in Sections 3.5.1 and 3.5.2. The system designed for 20°C ambient temperature can achieve a maximum thermal efficiency of 52.6% yet drops to 42.8% during periods of high ambient temperature, while the system designed for 30°C ambient temperature can achieve between 45.9%-50.6% for the same ambient temperature range. Incorporating the probability distribution for the entire year to calculate annual thermal efficiency weighted by ambient temperature or direct normal irradiance, the system designed for 20°C ambient temperature achieves higher performance. However, it is clear that considering the DNI-weighted ambient temperatures results in the 30°C design being relatively more competitive with the 20°C design.

The behavior reveals that an optimal cycle design exists to balance high design-point efficiency with the performance penalty for non-ideal ambient conditions, which is seen in the probabilistic results for the 25°C design case.

It is also clear from these results that variation in ambient temperature has a more dramatic impact on the s-CO_2 cycle compared to the Rankine cycle. For a 20°C increase in design-point ambient temperature, the baseline s-CO_2 cycle experiences a 16.7% drop in relative efficiency, compared to 7.5% for the baseline steam Rankine cycle.

4.3 Exergetic Optimization

Previous researchers have investigated optimum specifications for key parameters in designing a wide range of TES systems [90, 135-137]. Pioneering works by Bejan [138-140] utilized exergy analysis to evaluate the performance of a sensible heat storage (SHS) system and identify an optimum charging time and an optimum number of thermal units. Other studies have extended Bejan's analysis by modeling the entire charge-discharge cycle and concluded that a typical optimized system destroyed about 70-90% of the supplied exergy content, as reported by Krane [115] and Domanski and Fellah [141]. Dincer [4, 142] investigated the viability of different SHS media and defined useful criteria for evaluating exergetic performance. Gunnewiek, Nguyen, and Rosen [114] studied the optimum discharge period for an SHS system for an entire working cycle. Erek and Ezar modeled the effect of charging processes on the storage process [143].

Additionally, optimization methods have emerged as a useful tool that can assist in energy forecasting and resource allocation, design and operation strategies, energy supply and demand modeling, and emission reduction. Baños et al. conducted a comprehensive review of research

106

efforts that utilize a wide range of optimization schemes in renewable energy systems to obtain solutions to maximize energy resource allocation and reliability, and minimize system cost [144]. From the perspective of solar thermal power plant design, optimization can determine the optimal sizing, component specifications, and plant operation. Table 14 presents a brief review of studies reporting optimal values for CSP plant subsystems relative to each other.

Table 14: Various studies of the effect of varying solar multiple on CSP plant operation.

Solar field	TES	Power block	Local optimal value(s)	Ref.
Trough	Two-tank molten salt	110 MW$_e$ steam Rankine	SM = 1.5 – 1.7 TES = 2-4 h	[145]
Trough	Thermocline molten salt	111.5 MW$_e$ steam Rankine	SM = 3 TES = 16 h	[146]
Trough	None	50 MW$_e$ steam Rankine	SM = 1.15	[145]
Tower	Two-tank molten salt	110 MW$_e$ steam Rankine	SM = 2.5 TES = 12 h	[134]

The objective of this section is the thermodynamic evaluation and optimization of the overall performance of the TES system. This investigation extends the analysis of a prior study investigating the optimum operating parameters for the same system, as reported in [147, 148]. In this analysis, the sole constraint will be energy output – each TES case must discharge 1621 MWh$_t$ in order to fairly compare each case. Using energy output as an objective constraint is a rational approach for comparing TES systems with varying parameters in order to determine optimal

107

operating values, such that exergy destruction is minimized while maintaining the same output. The TES system model will determine the required storage fluid mass, while the charging period will take this as an input.

The goal of constructing a system is often to achieve the maximum efficiency at the lowest cost within the boundaries of the technical and economic constraints. Optimization problems can be ill-conditioned with large gradients, which necessitate higher computing resources. Numerous studies have applied optimization schemes to renewable energy system design and operation such as the Nelder-Mead Simplex method, Lagrangian relaxation, and sequential linear or quadratic programming. Depending on the characteristics of the optimization problem, conventional optimization methods may not be feasible; for optimization problems that are NP-hard, polynomial time algorithms require exponential computational time which proves difficult and impractical [144]. To solve this, many researchers have applied heuristic approaches to solar thermal optimization problems including particle swarm [149], genetic algorithms [150], and artificial neural networks [151].

In Section 4.2, the effect of varying certain design parameters was explored to determine the strongest drivers of affecting exergetic performance. Now, to obtain an optimized solution, the optimization problem is solved using sequential linear programming. In addition to the design constraints, the system optimization is constrained to meet certain requirements: a minimum charge time of 6 hours, maximum discharge time of 12 hours, and exergetic efficiency greater than 85%. The optimization problem utilizes a simplex search method that, given positive convexity, ensures an increase in the objective function. The simplex is defined by k-dimensional space with $k+1$ vertices, where k is the number of design parameters under study. The initial guess for the

108

TES system configuration creates $k+1$ vertices, and the primary vertex is selected by the highest objective function value. The numerical model is called for each iteration to calculate the objective function and apply the design constraints. Then, upon convergence, the optimal parameters and best value of the objective function are those corresponding to the primary vertex. The objective function in this study is the exergetic efficiency; the model can be easily modified to accommodate a multi-objective function defined by the user.

One important aspect of any TES system with a thermal gradient is the mixing process, which degrades the exergy content while maintaining the same energy content, for a well-insulated system. As discussed in Figure 46, the mode of operation can: 1) maintain constant mass flow rate, with varying HTF temperature, or 2) maintain constant HTF temperature, with varying mass flow rate.

(a)   (b)
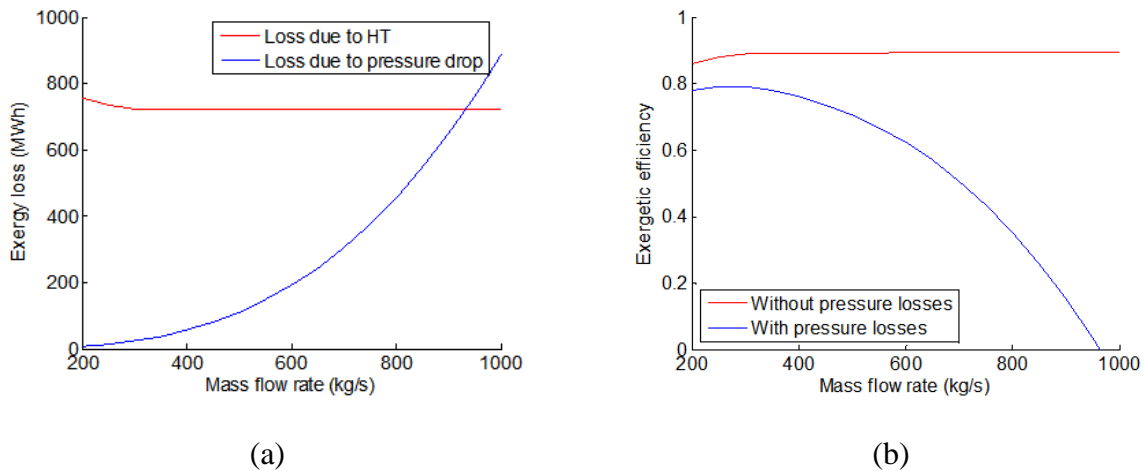
Figure 50: a) Exergy loss due to heat transfer (HT) and pressure drop, and b) exergetic efficiency with and without accounting for pressure drop.

109

Several deductions can be concluded from the results in Figure 50a. Most notably, the mode of operation is significant in determining the optimal design and operation of the TES system, especially because different parameters become independent or fixed. Once the mode of operation is selected, the balance of competing exergy destruction mechanisms via heat transfer and viscous losses translates to an optimal value of mass flow rate that very likely differs from alternative modes of operation. For low values of HTF mass flow rate, pressure drop is low while the heat transfer suffers and exergy destroyed due to transient thermal mixing is increased. Conversely, high values of HTF mass flow rate improves heat transfer, yet leads to an exponentially increasing pressure drop. Figure 50b shows the effect of this trade-off on exergetic efficiency, which reveals an optimal value for HTF mass flow rate.

As previously mentioned, the relative sizing of the system components, such as the solar field, TES, and power block, governs the overall system operation and performance. For example, a smaller solar field will generally not meet capacity needs of the power block. As solar field size increases, the thermal power output coming from the solar field can exceed the allowable limit for the power block causing "spillage", or excess energy that cannot be harnessed. The inclusion of a TES system allows for larger solar field sizes to collect energy for later use, thereby increasing capacity factor and flexibility for dispatch. Different CSP system configurations have been studied to find the optimal overall sizing of each component, and some key aspects are briefly listed in Table 14; however, other important system specifications that influence optimal values can be found at the source.

Here, we inspect the thermal gradient of the TES system and the effect of the latter mode of operation along with varying storage capacity, which is shown in Figure 51.

110
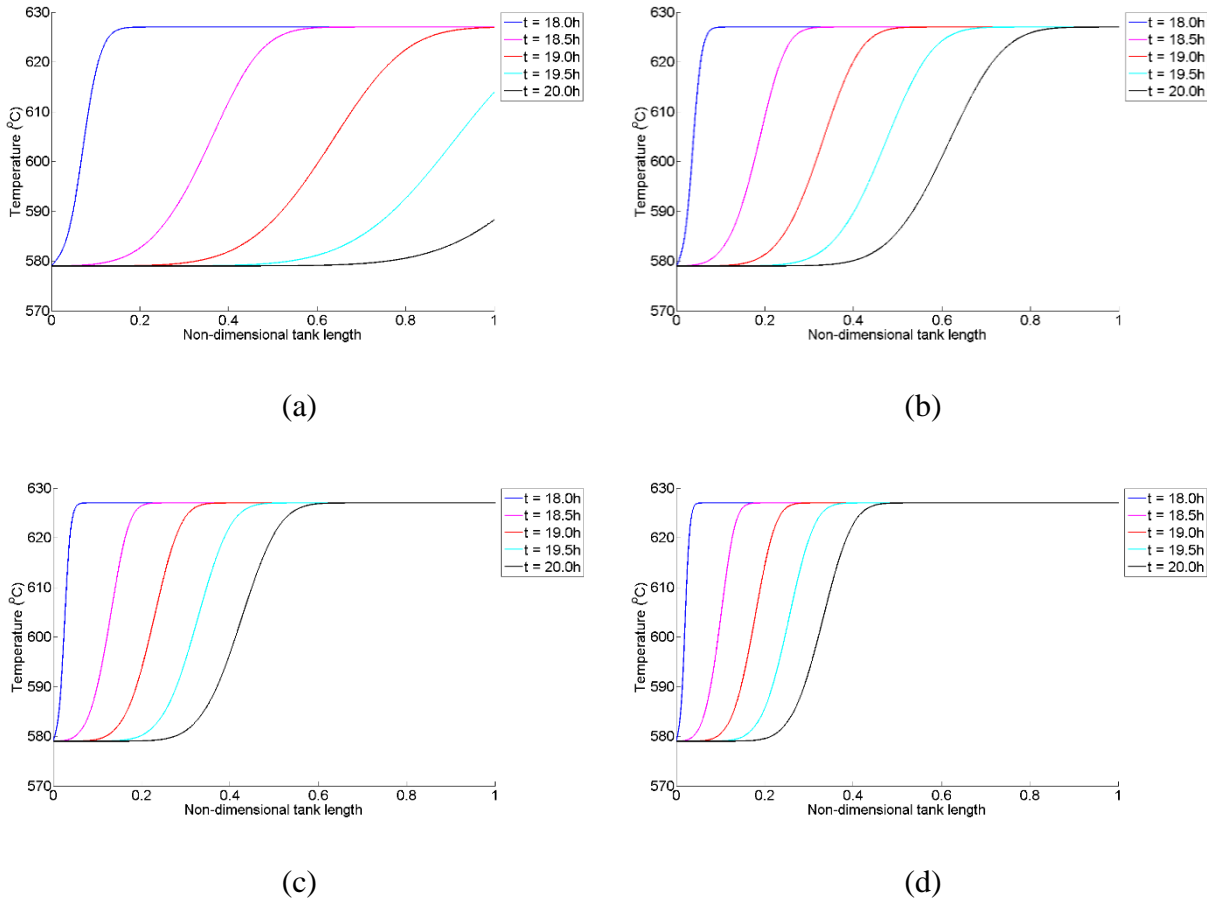
Figure 51: The thermal gradient of an elemental sulfur TES system for the mode of operation with varying mas flow rate to achieve constant HTF outlet temperature, for a) 3 hours, b) 6 hours, c) 9 hours, and d) 12 hours of storage capacity.

As Figure 51 shows, for low values of TES capacity, the tank becomes fully charged and discharging an undersized TES system relative to the power block leads to an unfavorable thermal gradient. Conversely, high values of TES capacity leads to an underutilized system. Therefore, an optimal value for TES capacity exists that balances these competing effects.

111

Both solar multiple and TES capacity are varied simultaneously for the parabolic trough plant integrated with an elemental sulfur TES system and the effect on exergetic efficiency is presented in Figure 52.
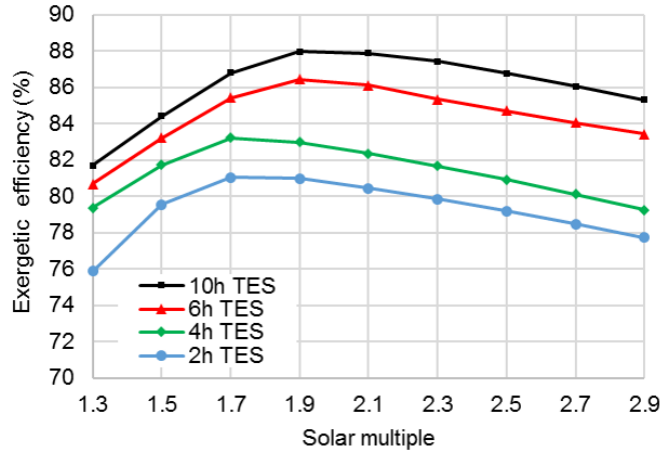
Figure 52: Exergetic efficiency as a function of solar multiple, for various hours of storage.

As Figure 52 shows, the optimal value of SM achieves the balance of collecting and providing sufficient thermal energy to the rest of the CSP components while minimizing "spillage" of wasted energy that cannot be collected. For increased TES capacity, the optimal SM increases to take advantage of the capability to collect energy for later use. Table 15 outlines the design parameters corresponding to the optimal elemental sulfur TES design and operation obtained from the parametric studies, as well as the optimization algorithm.

Table 15: Optimal values for an elemental sulfur TES design parameters evaluated by parametric study and optimization.

Parameter	Parametric study	Optimization

112

Storage fluid loading (kg/m^3)	1680	1680
Maximum storage temperature (°C)	600	627
Tube radius (m)	0.027	0.022
Tube pitch (-)	1.25	1.12
Solar multiple	2.0	1.9
TES storage capacity (h)	6	10
Power block design-point inlet temperature (°C)	600	627
Exergetic efficiency (-)	83.2	88.0

The results shown in Figure 52 illustrate that the exergetic performance can be increased from 84.1% to 87.9% by utilizing optimization schemes, with the respective optimal values for the design parameters. This increase in performance allows the TES system to achieve higher capacity factors and operate within the given set of constraints. However, this will often not correspond with a cost optimum [114], which is explored in the field of thermoeconomics by applying cost to exergy analysis, for which many methodologies have been developed [4]. The optimization scheme was also applied to the operating strategy, and is described in more detail in Appendix D.

This chapter characterizes the exergetic performance of the TES system and the subsequent opportunities for potential improvement using optimization methods. The optimization space includes both design and operating parameters, such as tube bank geometry, storage fluid loading, TES capacity, solar multiple, and power block characteristics. Using exergy as the fundamental property to optimize, competing exergy destruction mechanisms – namely, by heat transfer and by viscous losses – must be balanced to maximize the useful work that the TES system contains. Because there is a thermal gradient within the TES system, exergy can also be destroyed (or

113

entropy can be generated) via thermal mixing, which lowers the useful work stored even without losses to the environment. Moreover, choosing the mode of operation is also a significant design choice and represents a much larger space for optimization.

.

Chapter 5

Techno-economic Analysis

One of the primary factors that affect the deployment of CSP and TES technologies is the economic feasibility. To address this, the U.S. Department of Energy established the SunShot Initiative in 2011 to stimulate technological advances and identify cost-effective technologies [152]. The SunShot Initiative published a roadmap outlining the key technological and economic advancements and goals necessary to further development of CSP to reach cost parity with traditional fossil fuel sources. While the difference in cost may initially appear to be large, the expectation is that the mass production in the manufacturing process and product development will accelerate the cost reduction of the technology.

The most relevant cost target is for the TES system to reach $15/kWh$_t$ by 2020, a 25% reduction in cost within a five-year window as a baseline. The transition from Rankine power tower to s-CO_2 power tower implies a higher operating temperature which can lead to a larger temperature differential across the TES system and consequentially, lowers TES unit cost. In concert with the 66% capacity factor performance target, TES systems must simultaneously store energy more effectively while costing less. The roadmap has set a goal for levelized cost of electricity (LCOE) to reduce from $0.09/kWh in 2015 to $0.06/kWh by 2020. To provide the

114

reader with a broader sense of these values, the current LCOE estimates evaluated by IRENA for various renewable energy technologies are illustrated in Figure 53.
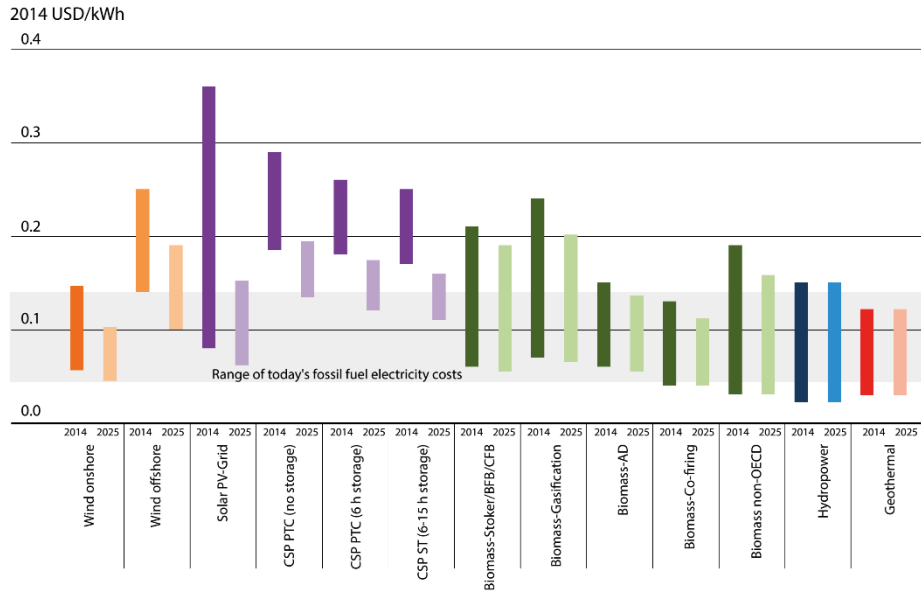
Figure 53: Comparison of LCOE for many different renewable energy technologies [153]

Comparative techno-economic assessment of TES systems can be challenging because of the diversity of technologies, which can add novel and unproven products that are still early in development. Understanding storage performance necessitates a set of metrics that fully describe the value of each TES system, which many researchers have written about [4, 154, 155]. This chapter investigates the interaction between TES technical performance and cost effectiveness.

5.1 Cost Estimation

Cost estimation is a critical component to inform technical design specifications to meet a desired return on investment. Similar to fluid property modeling, cost modeling can be a challenging and complex undertaking that involves a trade-off with time, complexity, and accuracy of the modeled results.

Numerous methodologies for assessing the economic feasibility of TES systems have been developed depending on the economic factors under consideration. Several models employ lifecycle analysis [156], while other studies estimate TES cost on an annual basis. Many studies investigate the added value of energy and grid services that TES can provide, including frequency regulation, spinning reserves, and non-spinning reserves [3, 157], and others incorporate the cost of mitigated greenhouse gas emissions and water usage [158-160].

5.1.1 Direct and Indirect Costs

The cost model is component-based to allow the user to take into account any changes dependent upon time or location, and is categorized broadly between direct and indirect costs. Currently, CSP requires relatively higher direct costs than some other energy generation technologies. TES systems also require operation and maintenance (O&M) costs to continue performing at design-point operation. Although the initial investment is high, CSP has lower O&M costs and many long-term benefits, including avoided fuel consumption, reduced CO_2 emissions, and advancement towards renewable portfolio standards.

The direct cost of the TES system is subdivided into several primary components: storage fluid, tube wall material, and resident volume of heat transfer fluid. Indirect costs vary greatly based upon the application that the TES system is integrated with. For simplicity, this analysis

116

assumes the TES system is integrated into a CSP plant. The costs under consideration are detailed

in

Table 16. Many assumptions are made in this analysis to provide a first approximation for the cost model, such as a simplified accounting for labor, balance of plant, among others.

Table 16: Overview of the cost for individual components considered in the TES system. The values listed are mean values from aggregated vendor quotes and other sources.

Direct Costs	Units	Mean value
Storage fluid	$/kg	• Naphthalene: 1.10 • Xylene: 1.50 • Decane: 1.50 • Glycerol: 1.75 • Elemental sulfur: 0.15
Tube wall material	$/kg	• Carbon steel: 1.25 • SS316: 3.00 • SS316L: 3.00 • SS347: 3.15 • Inconel:14.00
TES volume of heat transfer fluid	$/kg	• Therminol: 3.49 • Potassium nitrate salt: 1.00 • Hitec: 2.00 • Hitec XL: 3.96
Solar field	$/m^2	• Parabolic trough: 245 • Heliostat field: 165
Power cycle	$/kW	• Sub-critical Rankine: 875 • s-CO_2: 880
HTF system and tower/receiver	$/m^2	• Parabolic trough: 90 • Tower/receiver: 180
Indirect Costs		
O&M costs	$/kW-yr	50
Engineering and project management and owners' cost	% of direct cost	11
Contingency	% of direct cost	7
Balance of plant	% of direct cost	10
Financial parameters		
Discount rate	%	5.5
Inflation rate	%	3.0
Debt rate	%	6.0
Income tax	%	5.0
Sales tax rate	%	5.0
Federal tax	%	35

119

| ITC | % | 0 |

Many candidate materials for each component were considered. Vendor quotes for each material were averaged to determine a mean value. Direct cost inputs are based upon probabilistic modeling of available vendor quotes, which is described in the next section.

Indirect costs vary depending upon location, such as local labor rates, climate, tax rate, and market structure. Indirect costs vary greatly based upon the application that the TES system is integrated with. The items include integration cost, engineering and project management and owners' cost, sales tax, and contingency; the default values from the SAM Reference Plant Spreadsheet are chosen [161]. The cost data for many of the components remain uncertain with the exception of parabolic troughs and the sub-critical Rankine cycle, largely because of the relatively early development of each technology. As a result, most of the available cost data reflects early technology readiness level, with costs expected to decrease as the technology matures with further development.

5.1.2 Probabilistic Cost Analysis

Probabilistic cost analysis is introduced to quantify the inherent system uncertainties on the overall performance metrics of interest, and to evaluate two quantities: the magnitude of the possible factors containing uncertainty, and the likelihood of occurrence of the uncertainty for each factor. The spectrum of possible factors includes DNI availability, loan rate, and associated costs of plant subsystems. The probabilistic analysis methodology can be described in two stages. First, a probability distribution function appropriate to the dataset is generated for sampling. Then, a

120

sampling method utilizes the distribution to sample the variables containing uncertainty alongside the deterministic variables to evaluate the cost numbers of interest with a confidence interval.

Probability distribution functions are a realistic way of describing uncertainty and risk. Commonly used PDFs such as uniform, normal or triangular can be generated from empirical data, published literature, or user input. Subsequently, the model generates an estimated total TES cost with upper and lower bounds using vendor quotes as a dataset. For this study, a uniform distribution was used for the tube wall material due to the wide variance in the manufactured product (seamless tube, available diameters, bulk price for larger orders, etc.) so it is unclear whether one price is more probable than another. Latin Hypercube Sampling (LHS) is a systematic method of stratified sampling random numbers evenly over the sample space that can be applied to multiple variables. LHS requires fewer samples than Monte Carlo simulation, which can be helpful for sparse datasets, such as vendor quotes. The collection of modeled instances generates a probability distribution function that can be implemented into uncertainty and sensitivity analyses. A triangular distribution was used for the storage fluid which have variability in chemical purity, but is generally consistent in price. For the triangular distribution, the minimum and maximum values in the dataset are set to zero probability, and the most probable value is set such that the integration of the distribution is equal to one. Figure 54 shows a histogram of sampled datasets for the cost of elemental sulfur as a storage fluid candidate.

121
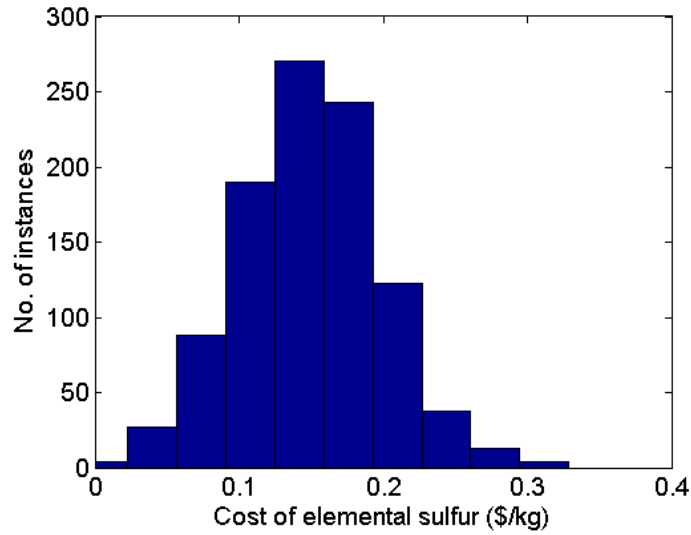
Figure 54: Histogram of elemental sulfur prices sampled [162].

5.1.3 Levelized Cost of Electricity

This section describes a mathematical framework developed to assess the value of the various TES systems employing different storage fluids, operating under different situations. The techno-economic performance of the TES system is assessed by the analysis of various CSP plant designs. The economic feasibility of utilizing elemental sulfur as a storage fluid in CSP applications is explored using well-established metrics described earlier in the chapter.

When projecting TES cost across the lifetime of the system, future revenue and expenses must be accounted for and discounted to the present value of money. This is most commonly achieved using a discount rate, and effectively determines when the sum of the total revenue reaches the sum of the total expenses. This can be expressed as

122

$$\sum_{n=1}^{N} \frac{Revenues_n}{\left(1+d\right)^n} = \sum_{n=1}^{N} \frac{Expenses_n}{\left(1+d\right)^n} \qquad (5.1)$$

The levelized cost of electricity (LCOE) is the most frequently used metric in comparative studies across electricity generation technologies. The expression for LCOE is then:

$$LCOE = \sum_{n=1}^{N} \frac{Q_n - R_n}{\left(1+d\right)^n} \qquad (5.2)$$

where d is the discount rate, N is the plant lifetime, and the default values from SAM are utilized.

5.2 Analysis of Supercritical Fluids

The purpose of this section is to conduct a comparative analysis of the storage fluid candidates being investigated. One important metric to measure is the vapor pressure. In the proposed single-tank design with the storage fluid enclosed in a rigid container, the vapor pressure is one of the primary drivers for the required wall thickness of the storage tube, which is directly related to cost. Figure 55 shows the vapor pressure as a function of temperature for storage fluid candidates.

123
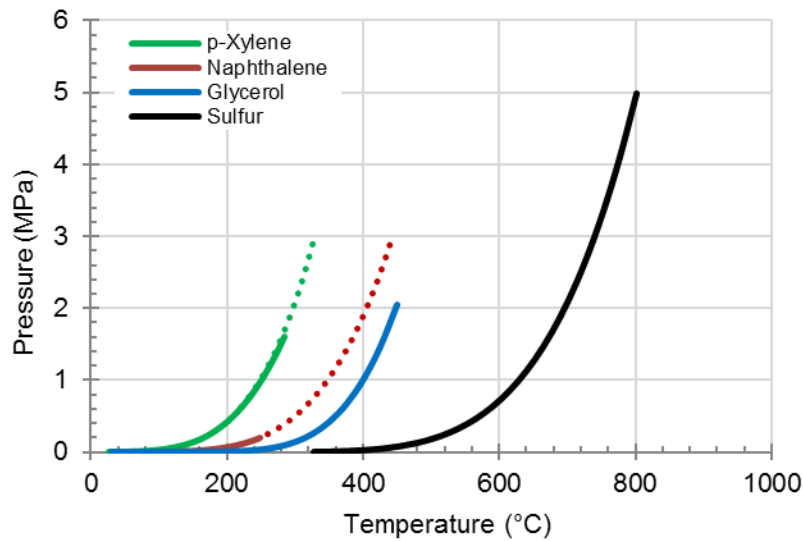
Figure 55: Vapor pressure of fluid candidates as a function of temperature. The solid lines denote experimental results, and the dotted lines denote numerical modeling results [163, 164].

The results shown in Figure 55 illustrate the realistic operating temperature for each storage fluid, based upon practical limits of vapor pressure as a function of temperature. Many other fluid candidates were screened and thermally cycled to examine vapor pressure, long-term thermal stability, material compatibility, among other parameters, which can be difficult to weigh. The two primary parameters are vapor pressure and thermal decomposition. Typical maximum operating temperatures for CSP plants are 390°C for parabolic trough plants, and 565°C for power tower plants. These results are reported in more detail in Appendix B.

Figure 56a Figure 56b show the internal energy and isochoric specific heat of naphthalene, respectively.

124

(a)

125
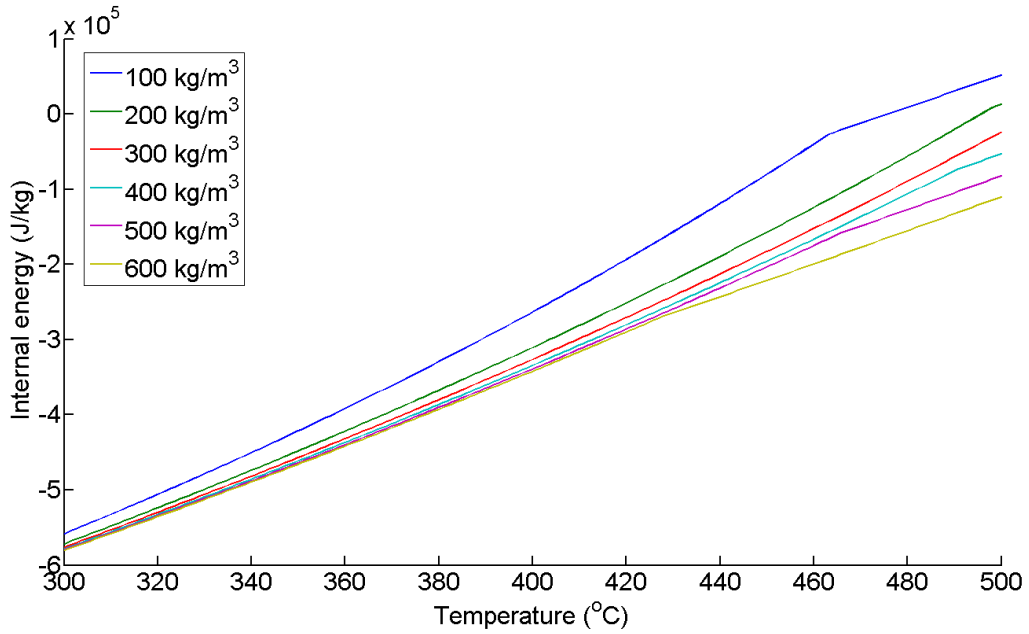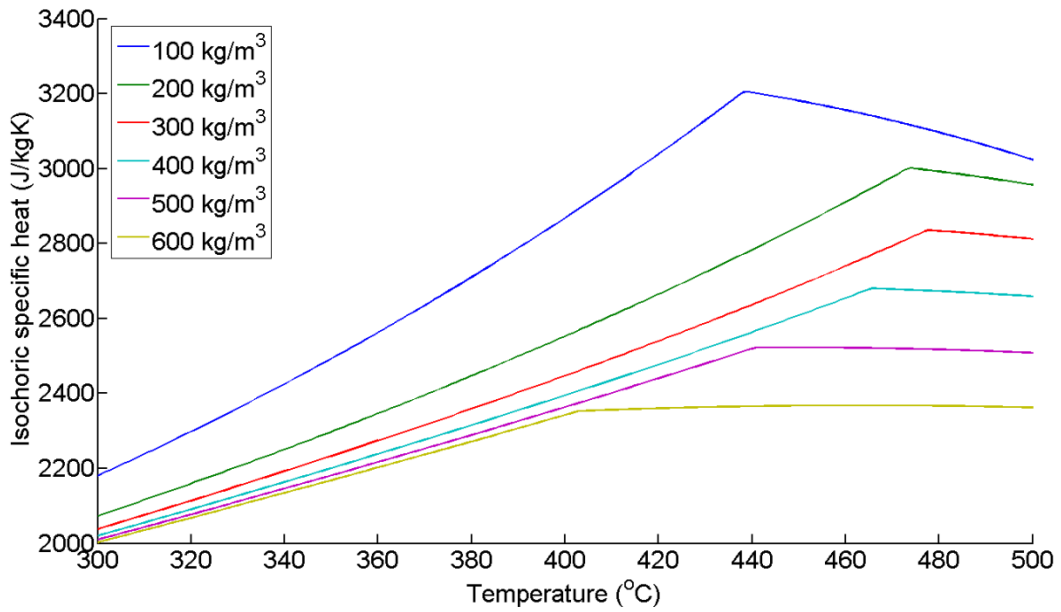
Figure 56: a) Internal energy and b) isochoric specific heat of naphthalene as a function of density and temperature, for a temperature differential of 100°C.

The results in Figure 59b show that as loading increases, the isochoric specific heat drops dramatically and the peak because less pronounced. The primary reason for this is because as the loading increases from 100 to 600 kg/m^3, it deviates further from the pseudo-critical line. As the cost breakdown of a naphthalene TES system for two temperature differentials is shown in Figure 57. The analysis is limited to a maximum operating temperature of 480°C due to long-term thermal stability concerns that were encountered in a longer thermal cycling study following the rapid screening studies discussed in Appendix B.

$$\Delta T = 100°C$$

Figure 57: Specific TES cost for naphthalene with SS316L tubes as a function of maximum operating temperature, for a typical temperature differential for trough plants.

The results presented in Figure 57 illustrate a couple key conclusions. Firstly, for a TES system employed naphthalene as a storage medium with a 100°C temperature differential, the prevailing trend of increasing cost with increasing maximum temperature is dominated by the high vapor pressure associated with naphthalene as it approaches the supercritical state. Thus, it is preferable to operate in the liquid and two-phase regime (well below 475°C, the critical temperature of naphthalene) to avoid the prohibitively high cost of the containment vessel. Therefore, in regards to TES cost, a modest thermodynamic advantage that might be realized by supercritical operation is negated by cost considerations related to high vapor pressure. Secondly, long-term thermal cycling experiments showed naphthalene exhibited thermal decomposition above 480°C at a level that is not well-suited for operation in a CSP plant with a 30-year lifetime. The thermal decomposition is also a contributing factor to the high vapor pressure by subsequently increasing the number of moles of decomposition constituents.

A fluid that can operate in the supercritical regime and have relatively low vapor pressure would be attractive; however, such a fluid that is suitable for typical CSP operating temperatures was not discovered in this work. The need for high-cost containment, along with the inability to withstand operating high operating temperatures desired for future CSP plants, leads to the conclusion that the fluids investigated for supercritical operation are unsuitable for TES in current CSP applications.

5.3 Analysis of Elemental Sulfur

As discussed in Section 2.2, using elemental sulfur in an indirect TES configuration in CSP applications was one of the initial storage fluid candidates considered for operation in the

supercritical regime. However, the thermal stability limitations of the organic fluid candidates at typical CSP plant temperatures and the challenges of operating in the supercritical regime led to the subsequent search for a storage medium capable of high-temperature operation in the liquid and two-phase regime. Consequently, elemental sulfur was identified as a promising storage medium candidate since it presents numerous advantages, including: high thermal stability, attractive thermophysical behavior, low unit price and high abundance, and a wide knowledge base of handling and transportation from the oil, gas, and mining industries.

In the CSP industry, the energy density of the TES system is another important metric that is becoming increasingly important. Energy density can be evaluated on a volumetric (per unit volume) and gravimetric (per unit mass) basis. Figure 58 shows the energy density for the TES system employing elemental sulfur as a function of maximum temperature for various temperature differential values, which generally varies based upon specific applications.

(a)

128
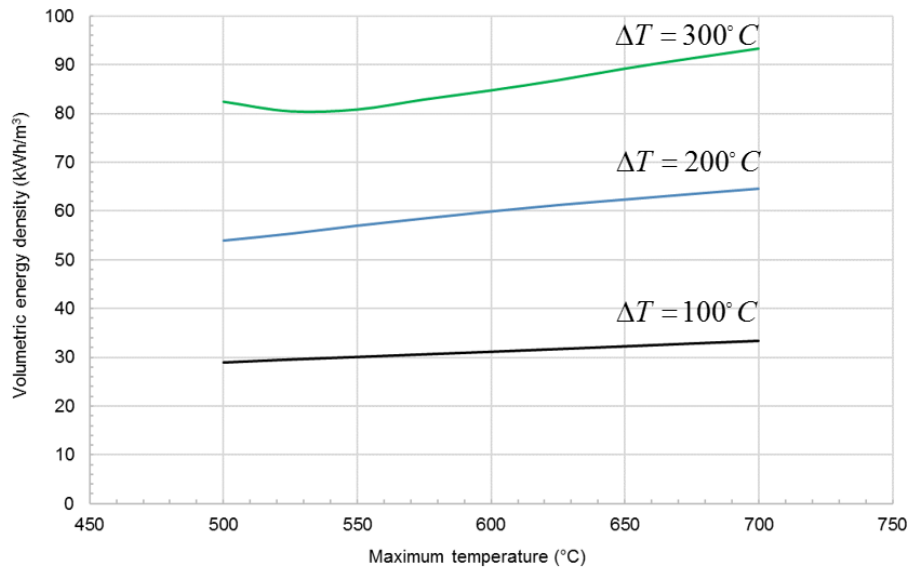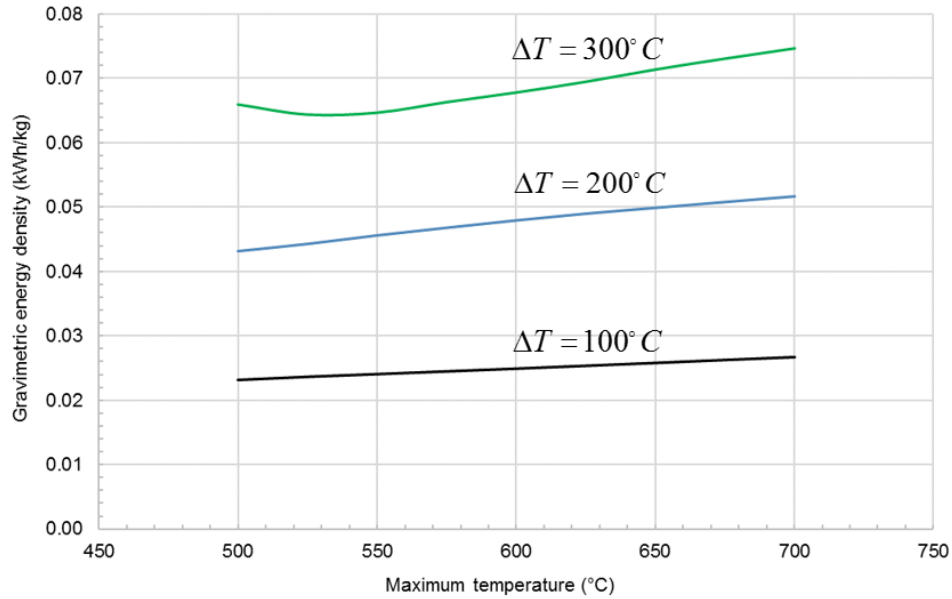
(b)

Figure 58: a) Volumetric energy density and b) gravimetric energy density of the single-tank system employing elemental sulfur as a function of maximum temperature, for various values of temperature differential.

Figure 58 shows the volumetric and gravimetric energy density, respectively, of an elemental sulfur TES system with three cases presented for varying temperature differential, ΔT, from 100°C to 300°C. By quick inspection, it is intuitive that larger values of ΔT increases both volumetric and gravimetric energy density. The results of particular interest are the magnitude for each energy density at typical CSP maximum operating temperature and ΔT. For a typical CSP power tower plant, the operating temperature range is 565°C to 290°C, with $\Delta T = 275$°C. Under these conditions, the volumetric energy density is 82 kWh/m^3 and the gravimetric energy density is 0.06 kWh/kg, both of which are promising. The next generation of CSP plant designs are projected to

129

attain maximum operating temperatures greater than 650°C along with larger values of ΔT [152], which in case both energy densities become even more attractive. With a maximum operating temperature of 650°C and conservatively assuming that ΔT remains at a constant 275°C, volumetric energy density approaches 90 kWh/m^3 and gravimetric energy density becomes 0.07 kWh/kg.

Comparative studies must choose certain system design variables or outputs to hold constant to establish a fair comparison, such as solar field aperture area, plant cost, or net annual electricity output. The current analysis keeps constant the solar field aperture area for both technologies, namely comparing parabolic trough to power tower, to investigate the trade-off between systems with higher optical (and thermal) efficiencies that also have higher costs. Another outcome of the comparative study is to assess the cost and performance of different TES system designs. Each case -- whether the operating temperature, fluid loading, or any other parameter is different – must contain the same energy in order to be compared fairly, and the observation comes in how efficiently each case uses this energy. Therefore, solar multiple is held constant, and indirectly the power block nameplate capacity must also be constant because both solar multiple and TES capacity are dependent upon it. The difference in performance will subsequently lead to different values for LCOE. Then, the unit cost of the TES system is included. The analysis for a parabolic trough plant are detailed in Table 17.

130

Table 17: Performance and economic analyses of annual simulation for parabolic trough plant with elemental sulfur TES.

Design parameters	Storage capacity			
	3 h	6 h	9 h	12 h
Solar multiple	2.1	2.1	2.1	2.1
Power block gross capacity (MW$_e$)	53	53	53	53
Plant location (TMY3 weather input)	Daggett, CA	Daggett, CA	Daggett, CA	Daggett, CA
TES storage capacity (h)	3	6	9	12
Storage material volume (m^3)	1.1×10^4	2.2×10^4	3.3×10^4	4.4×10^4
Containment material (kg)	2.3×10^6	4.7×10^6	6.9×10^6	9.2×10^6
Performance and cost				
Capacity factor	37%	39%	40%	41%
Net electricity production (GWh/year)	155	174	186	190
Parasitic load (GWh/year)	1.7	2.3	2.7	2.8
TES unit cost ($/kWh$_t$)	20	20	20	20
LCOE ($/kWh$_e$)	0.16	0.13	0.11	0.10

First, the unit cost of TES outperforms the cost target of $25/kWh$_t$ for the 2020 trough roadmap. While this is due to a combination of technical and economic factors, one of the primary reasons is that elemental sulfur is an order of magnitude less expensive than Hitec molten salt, which ranges from 1.00 – 1.50 $/kg. Second, LCOE meets the 2020 SunShot target for cases greater than 9 hours of storage, while the remaining cases do not meet this value. The principal reason for this behavior is that as storage capacity increases, less incident energy is spilled during periods of high

131

insolation. By increasing the plant's capability to minimize spillage, the relatively lower cost of storage ensures that the investment of the solar field, which has a relatively higher unit cost compared to TES, is maximized.

As CSP plants trend towards future designs with higher operating temperature and temperature differential, it is of interest to evaluate specific TES costs. The upper, lower, and most-probable values are shown in Figure 59 as a function of maximum operating temperature.

$\Delta T = 275°C$ $\Delta T = 350°C$

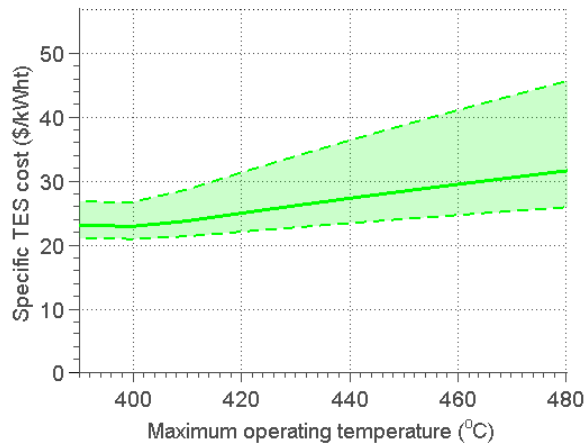(a)   (b)
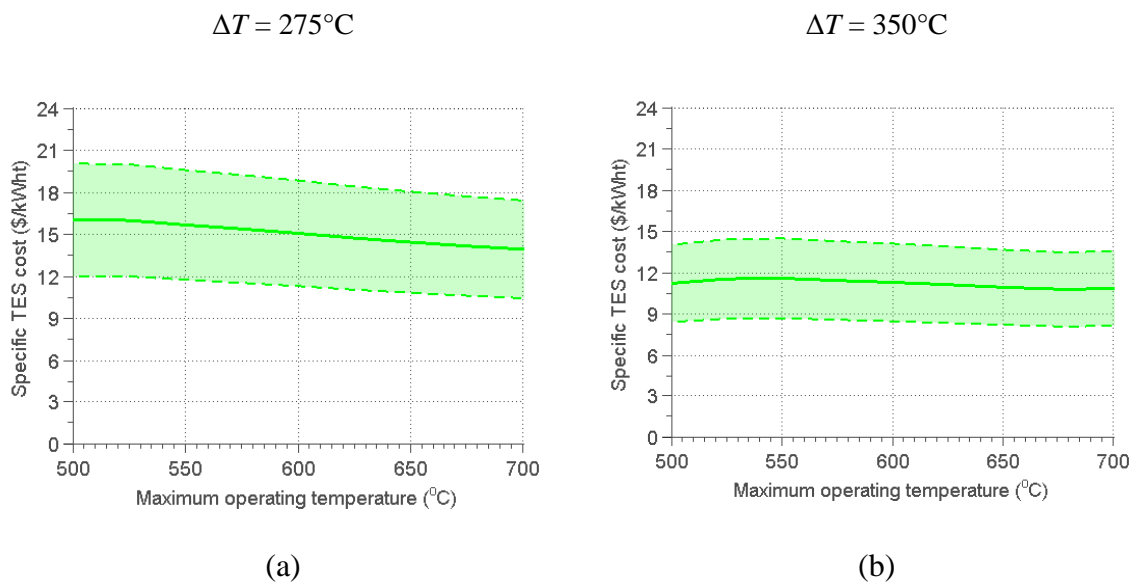
Figure 59: Specific TES cost for sulfur with SS316L tubes as a function of maximum operating temperature, for two values of temperature differential across the TES system.

The results presented in Figure 3 illustrate that the effect of maximum operating temperature has a minor influence on specific TES cost. This is largely due to the greater extent of dissociation from S_8 to S_2 at higher temperatures. Figure 59a shows results for a temperature differential of 275°C, which is the current value for existing power tower plants (which have a maximum

operating temperature of 565°C). From a preliminary cost analysis, the elemental sulfur TES shows promise to lower cost of TES for existing plant designs. Broadly, this can be largely attributed to the suitable fluid properties of elemental sulfur, as well as its low price. Figure 59b represents future CSP plants that are capable of operating with a larger temperature differential of 350°C. Intuitively, the specific TES cost decreases with higher temperature differential. The upper bound in this case remains below the SunShot goal of $15/kWh$_t$, which reveals that even for the most expensive vendor quotes collected, the elemental sulfur TES system shows early encouraging signs of economic feasibility.

Figure 59 shows a cost breakdown and comparison of TES systems employing naphthalene, elemental sulfur, and molten salt. The calculation for costs of the naphthalene TES system is limited to 290°C – 480°C due to thermal stability limitations, and elemental sulfur and molten salt TES systems are for maximum operating temperature of 290°C – 565°C.
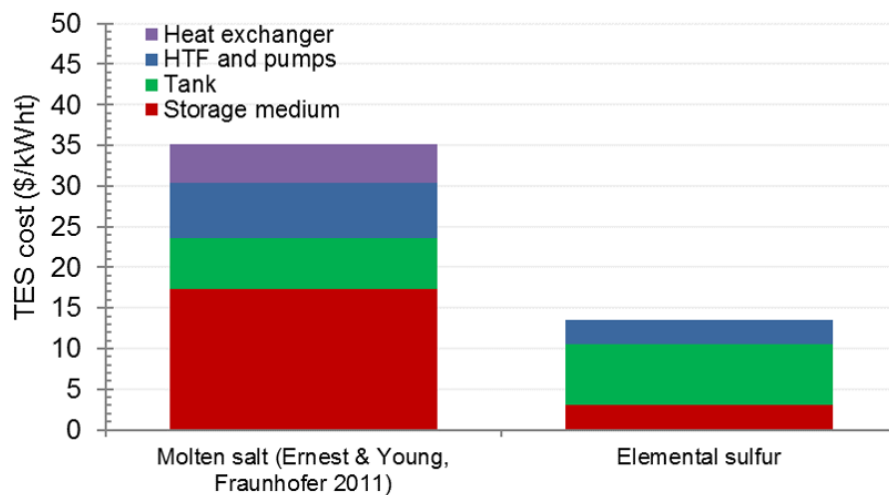
Figure 60: Cost comparison of molten salt [165] and elemental sulfur TES system costs.

133

Figure 60 highlights a few important observations. Firstly, the overwhelming cost of the molten salt TES system is the salt itself. It is evident that the storage medium presents the greatest opportunity for cost reduction. Most notably, elemental sulfur combines the most attractive traits of the molten salt and naphthalene-based systems, respectively: 1) it exhibits low vapor pressure for the operating temperatures of interest, as in the molten salt TES system, and 2) it has a significantly low-cost storage medium, far less than both the molten salt and naphthalene-based TES systems. Elemental sulfur has an opportunity to substantially reduce the cost of TES systems and warrants much more investigation to determine its economic viability to be commercially manufactured and integrated into CSP plants.

In summary, the objective of this chapter was to evaluate techno-economic analysis of a TES system employing supercritical fluids, and a TES system employing elemental sulfur as a storage medium in the context of CSP applications. A thermodynamic and cost model simulated annual performance of the elemental sulfur TES system integrated in a large-scale CSP trough plant. The results illustrated that naphthalene, the leading storage fluid candidate for supercritical operation in this study, can be cost-effective in the sub-critical temperature range 290°C – 420°C, while operating at higher temperatures near the supercritical point leads to excessive vapor pressure and thermal stability issues. The simulations for an elemental sulfur TES system show that it can meet the SunShot 2020 cost targets of \$25/kWh$_t$ for trough plants, and \$0.12/kWh$_e$ for plant designs with greater than 9 hours of storage capacity. Overall, this research effort illustrates that elemental sulfur is a promising, low-cost TES material for CSP applications.

134

135

Chapter 6

Conclusion

Low-cost storage fluid candidates show promise to lower the cost of TES systems, maximize energy generation to the grid at peak demand, and enable higher penetration of renewable energy technologies. The chemistry and vapor-liquid equilibrium varies greatly between fluids and therefore, it is necessary to develop high-fidelity models in order to accurately assess transient performance and thermal property variation. The behavior of the storage fluid is characterized using different methods, including regressions, equations of state, and semi-empirical phase and reaction equilibrium modeling, which is integrated into a system-level CSP plant to evaluate the TES system performance. Furthermore, techno-economic analysis was conducted to evaluate economic feasibility using well-established metrics that fully describe the value of each TES system.

The results of this work revealed elemental sulfur as a promising candidate capable of operating in high-temperature CSP plants. Elemental sulfur has several key advantages for high-temperature operation. One of the fundamental requisites of a storage fluid is high thermal stability over a 30-year plant lifetime. As an element, sulfur exhibits very little, if any, thermal decomposition and thus makes it an ideal candidate for high-temperature CSP operation, in an environment where there are few choices for thermally stable storage fluids. Secondly, the thermochemical storage of elemental sulfur via endothermic bond-breaking process of S_8 chains breaking into smaller S_2 molecules at higher temperatures has an attractive enthalpy of reaction, while requiring no catalyst. Additionally, elemental sulfur is very low cost as a market commodity,

136

and is well understood in part to sulfur recovery systems. The techno-economic analysis showed that economic feasibility warrants further research and cost modeling of an elemental sulfur TES system.

6.1 Recommended Future Work

There are several immediate directions for further investigation. Firstly, optimal design of the TES system parameters, such as tube radius or containment material, was not explored. This can reduce costs considerably and lead to economic viability over a wider range of storage capacities. Therefore, this area is highly recommended for near-term future work.

It is also worth investigating the performance of an elemental sulfur TES system integrated with CSP power plants operating at higher temperatures, which has been identified as the general path forward to increase cycle efficiency of the power block. High-temperature operation presents several challenges that are common to all TES technologies. In order to capitalize on the thermal stability of elemental sulfur at high temperatures, the model is being developed for high-temperature CSP plants integrating with a power tower and supercritical CO2 Brayton cycle [70]. The SunShot 2020 cost targets for CSP power tower systems are to achieve a TES unit cost of $15/kWh$_t$ and an LCOE of $0.06/kWh$_e$. There are further opportunities for optimization of dispatch controls that have not been explored, including weather forecasting and ancillary service provision.

In addition, sensitivity analyses can be used to determine the strongest drivers of system performance and cost. Specifically, optimization of tank design to balance effective heat transfer with pressure drop will lead to a TES system with higher exergetic efficiency. The developed TES model was built in the context of CSP applications, which provides insight into enabling higher

137

solar penetration on the grid. Linear Fresnel Reflectors (LFR) possess an interesting combination of design advantages and challenges. One chief advantage is LFRs do not use rotating joints, as the conventional troughs do at the end of each collector line, and they do not necessarily have metal–glass welds at the ends of each receiver tube module for maintaining vacuum within the outermost tube and as a result, are cheaper to manufacture from both a material and labor standpoint. Additionally, lower maintenance and operation costs prove to be another benefit. Substantial cost reduction potential can be realized primarily due to cheaper mirrors and lower structural costs [166]. However, lower optical performance remains a challenge and must be balanced by lower cost per m^2 of aperture compared to parabolic troughs or power towers. Finally, the performance and economic feasibility of TES in other applications, such as geothermal, combined heat and power, and grid storage present interesting opportunities the merit exploration. The flexibility of the TES model allows any model that fits the interface described in Chapter 3 to communicate with other energy-based models for different systems. The performance of the TES system can then be repeated with minimal modification of the code.

138

Appendix A: Model Interfaces

main module

The first section of the model starts with a legend of variables, and system-level specifications for plant component sizing and configuration. This includes solar multiple, hours of thermal storage, and nameplate power block capacity. Additionally, the HTF medium, storage fluid medium, storage tube material, and type of power cycle technology can also be chosen at this point.

Table 18: Input arguments for the overall plant design and sizing.

Variable	Units	Notes
Solar field		
solarField_config	-	Solar field technology. The user can select one of the following: 1. Parabolic trough 2. Power tower 3. Linear Fresnel
sm	-	Solar multiple
htf	-	Heat transfer fluid. The user can select one of the following: 1. Therminol VP-1 2. Therminol 66 3. Potassium nitrate salt (NaNO3-KNO3) 4. Hitec 5. Hitec XL
Thermal energy storage		
tes_hours	h	Hours of TES, relative to the power cycle nameplate capacity
tubeProps	-	Structure containing all tube material properties
fluidProps	-	Structure containing all storage fluid properties

139

Power block (structure: powerBlock)		
power_cycle_config	-	Power cycle technology. The user can select one of the following: 1. Sub-critical Rankine (wet-cooled) 2. Supercritical carbon dioxide Brayton (wet-cooled) 3. Supercritical carbon dioxide Brayton (dry-cooled)
Q_dot_pb_des	MW	Nameplate capacity of power block

solarField function

For a specified solar field configuration, solar multiple, and other design parameters detailed in Table 4, the thermal energy collected by the receiver is determined by SAM at hourly intervals. The receiver performance is assumed to be independent of the thermal storage and power block subsystems, and is evaluated on an annual basis. For this study, meteorological data are used for Daggett, CA from the TMY3 database [81].

Table 19: Input arguments for the solar field model.

Variable	Units	Notes
General		
SM	-	Solar multiple
Location	-	Meteorological data
HTF	-	HTF properties
Q_dot_ref	W/m^2	Reference
Technology	-	Solar field technology. The user can select one of the following: 1. Parabolic trough 2. Heliostat field with central receiver
m_dot_htf_min	kg/s	Minimum allowable HTF mass flow rate

140

m_dot_htf_max	kg/s	Maximmum allowable HTF mass flow rate
Outputs		
A_sf	m^2	Total aperture area of solar field
Q_abs	W	Total absorbed thermal energy by the solar field
eff_sf	-	Thermal efficiency of the solar field

auto_tes_design function

The thermal energy storage model has two distinct functions: one for the design of the TES system based upon user specified parameters, and another for the operating state of the TES system during transient simulation. Firstly, the TES design model determines the specific design parameters required to store the desired hours of TES capacity according to Eq. (3.17).

Table 20: Input arguments for the TES design model.

Variable	Units	Notes
Inputs		
tes_hours	h	Hours of TES capacity
Q_dot_pb_des	MW$_e$	Nameplate capacity of the power cycle
nu_pb_des	-	Thermal efficiency of the power cycle at design-point conditions
T_high	°C	Hot temperature of the system operating at design-point
T_low	°C	Low temperature of the system operating at design-point
storage_fluid	-	Storage fluid medium. The user can choose one of the following, or insert user-defined values for the storage fluid properties as a function of temperature and density: • Naphthalene • Decane • *para*-Xylene

141

		• Sulfur
rho_stor	kg/m^3	Density of storage fluid
rhoL_sat_stor	kg/m^3	Saturated liquid density of fluid
rhoG_sat_stor	kg/m^3	Saturated vapor density of fluid
k_stor	W/mK	Thermal conductivity of storage fluid
Tube material properties		
tube_material	-	Tube material. The user can choose one of the following, or insert user-defined values for the tube material properties: • Carbon steel • Stainless steel 316L • Stainless steel 347 • Inconel 600 • Titanium
F_tu	MPa	Ultimate tensile strength of tube material
sigma_wall	MPa	Allowable stress
derate	-	Thermal derating factor based upon maximum temperature
n	-	Safety factor
cp_wall	J/kgK	Specific heat of tube material
rho_wall	kg/m3	Density of tube material
k_wall	W/mK	Thermal conductivity of tube material
r_i	m	Tube inner radius
L	m	Tube length
p_t	m	Tube pitch
Outputs		
m_stor	kg	Total mass of storage fluid
V_stor	m^3	Total volume of storage fluid
E_stor_vol	kJ/m^3	Volumetric energy density of storage fluid

142

Variable	Units	Notes
P_stor	MPa	Pressure of storage fluid
cv_stor	J/kgK	Specific heat of storage fluid
t_wall	m	Tube wall thickness
N_tubes	-	Total number of tubes

One of the primary outputs of the TES design model is the required storage fluid mass to achieve the desired storage capacity. The required storage fluid mass is driven by fluid properties such as the specific heat and density of the storage fluid. Similarly, another important fluid property is the pressure of the storage fluid at the maximum operating temperature. Based upon the chosen storage medium, these fluid properties are evaluated using an appropriate fluid property modeling methodology and is described in more detail in Chapter 3: Fluid Property Modeling. Tube wall thickness, a significant driver of the cost of the TES system, is calculated using the maximum pressure of the storage fluid in tandem with the tube material properties and geometry per Eq. (3.20).

fcn_powerBlock_design function

The performance analysis models import the design-point specifications, and evaluate the performance of the specific subsystem during operation. Specifically, the off-design performance is characterized during periods when one or more parameters deviate from design-point values.

Table 21: Input arguments for the power block design model.

Variable	Units	Notes
Inputs		

143

Variable	Units	Notes
powerBlock_config	-	Power cycle technology. The user can select one of the following, or define the following parameters: 1. Sub-critical Rankine (wet-cooled) 2. Supercritical carbon dioxide Brayton (wet-cooled) 3. Supercritical carbon dioxide Brayton (dry-cooled)
Q_dot_pb	MW	Nameplate capacity of power block
Q_dot_pb_ref	MW	Nameplate capacity of reference power block
T_pb_in_des	°C	Design-point HTF temperature into the power block
T_pb_out_des	°C	Design-point HTF temperature exiting the power block
m_dot_htf_des_ref	kg/s	Design-point HTF mass flow rate of reference power block
nu_pb_des	-	Design-point cycle efficiency
Outputs		
cap_ratio	-	Capacity ratio of the user-defined nameplate capacity, and the reference power block nameplate capacity
m_dot_htf_des	kg/s	Design-point HTF mass flow rate

fcn_tes_tank_od function

The off-design TES model imports the design-point specifications and evaluate the performance of the TES tank to determine the spatial and temporal temperature distribution.

Table 22: Input arguments for the off-design TES model.

Variable	Units	Notes
Thermal energy storage		
m_dot_htf	kg/s	HTF mass flow rate into the TES system
T_htf_in	°C	HTF temperature into the TES system
T_amb	°C	Ambient temperature

Outputs		
Nu_o	-	Outer Nusselt number
T_stor	°C	Storage fluid temperature
T_stor_avg	°C	Average axial storage fluid temperature
T_wall	°C	Tube wall material temperature
T_wall_avg	°C	Average axial tube wall material temperature
T_htf	°C	HTF temperature
T_htf_avg	°C	Average axial HTF temperature

Appendix B: Organic Fluid Screening

THERMAL TESTING OF ORGANIC FLUIDS FOR SUPERCRITICALTHERMAL ENERGY STORAGE SYSTEMS

Louis A. Tse
Department of Mechanical and
Aerospace Engineering
University of California, Los Angeles
Los Angeles, CA, USA

Antoine Stopin
Department of Chemistry and
Biochemistry
University of California, Los Angeles
Los Angeles, CA, USA

Gani B. Ganapathi
Jet Propulsion Laboratory
California Institute of Technology
Pasadena, CA, USA

Miguel A. Garcia-Garibay
Department of Chemistry and
Biochemistry
University of California, Los Angeles
Los Angeles, CA, USA

Richard E. Wirz
Department of Mechanical and
Aerospace Engineering
University of California, Los Angeles
Los Angeles, CA, USA

ABSTRACT

Concentrating solar power (CSP) continues to advance as worldwide interest in renewable energy continues to grow. CSP technologies, including parabolic troughs, power towers, and dish/engines, provide the unique potential for low-cost thermal energy storage that will ensure that renewable energy can become cost-competitive with traditional fossil fuel sources on a large scale and comprise a significant portion of the global energy portfolio.

The challenge is to develop cost-effective thermal energy storage to ensure that renewable energy can become a major part of the national and global energy supply. Storage fluid selection is a critical decision that must fulfill a number of criteria to not only provide long-term reliability, but also to remain cost-competitive in the power generation arena. The state-of-the-art thermal storage design uses a 2-tank molten salt configuration. However, most molten salt mixtures have a relatively high freezing temperature, which poses some system design issues. Additionally, the price of molten salt mixtures is steadily increasing. Current laboratory and industry research efforts have shifted focus to exploration of alternative storage fluids to significantly reduce costs.

146

In this study, several storage fluid candidates have been selected based on an attractive combination of thermodynamic properties, cost, and availability. In this paper, rapid screening of fluid candidates is reported, and an expanded series of thermal cycling and supercritical characterization experiments have been planned and are being implemented to determine the long-term durability of the fluid candidates over a range of operating temperatures for extended periods of time. Commercial-grade materials were used, and in the case of naphthalene and biphenyl, the testing procedure was carefully controlled to prevent sublimation of the sample. This paper presents the results of a study investigating the thermal stability of several organic fluids. Samples were extracted and chemical analyses such as nuclear magnetic resonance (NMR) and gas chromatography (GC) were conducted to observe degradation behavior and decomposition pathways. The rapid screening phase provided a timely and effective filter of the best-performing fluid candidates for supercritical thermal energy storage.

INTRODUCTION

The common principle of CSP technologies is that it captures the thermal energy from the sun to deliver heat to generate electricity. One of the key factors in advancing this field has been the development of thermal energy storage (TES), which is an integral element in concentrating solar power (CSP) plants that mitigates short-term intermittency due to cloud cover or during nighttime. The Department of Energy has identified improved thermal energy storage as one of the critical technology developments needed to allow solar thermal power to replace non-renewable power generation sources.

The current state-of-the-art TES design utilizes a two-tank indirect storage system with molten nitrate salts. However, the salt mixtures used for these systems, which are typically a mixture of sodium nitrate (60 wt%) and potassium nitrate (40 wt%), can be prohibitively expensive. Many researchers are investigating more complex salt mixtures with low melting point and thermal stability (Raade and Padwitz 2011 [1], Bradshaw and Siegel 2008 [2]), characterizing current salt blends (Trahan et al 2012 [3]), and even enhancing the thermal conductivity of salts through composites (Pincemin et al 2008 [4]). A recent study by Kelly [5] even investigated advanced thermal storage using supercritical H2O and CO2 as heat transfer fluids in power tower applications, although these two particular fluids were deemed impractical for that purpose due to high vapor pressure and fluid properties with strong temperature dependence within the operating range. The principal objective of this study [6] is to evaluate the implementation of supercritical fluids as a storage medium. By thermally cycling the storage fluid between a relatively low temperature two-phase state and a high temperature supercritical state, a large excursion in internal energy can be accessed which includes both sensible heat and latent heat. The main challenge to such a system is the high pressure associated with the supercritical state, necessitating a thick-walled storage vessel. To mitigate this cost, the proposed design utilizes a single-tank TES system, effectively halving the required wall material.

As part of the larger research project, a systematic series of thermal cycling experiments is being conducted to identify potential storage fluids with a combination of attractive thermodynamic properties, high thermal stability, and low cost. In parallel of the fluid selection process and thorough analyses of fluid samples, a small-scale demonstration of the single-tank design has been constructed by the Jet Propulsion Laboratory to assess system operability [7].

147

In the proposed design, the storage fluid is enclosed in tube bundles with sufficient wall thickness to withstand the highest system pressure. Vapor pressure has been one of the primary concerns in designing TES systems; however, the rising cost of molten salt may negate the benefits of its low vapor pressure. The tube bundles are contained in a low-pressure tank shell, through which the heat transfer fluid (HTF) flows, creating an internal heat exchanger within the storage tank.

The thermal decomposition of supercritical organic fluids as a function of thermal cycling is less predictable due to few investigations in the high-temperature thermal stability of organic fluids. Therefore, storage materials must be strategically chosen to attain the most attractive combination of several traits:

1. Desirable thermophysical properties
2. Thermally stable
3. Low melting point
4. Compatibility between storage and tank material
5. Low cost
6. High availability
7. Minimal environmental and health impact

Potential candidates for new storage fluids

Currently, there is a significant amount of data regarding organic fluids; however, the scientific data is relatively limited in the supercritical regime. This is partly because many organic fluids become volatile at high temperatures, and their potential applications for thermal energy storage have not been explored. The critical properties of the storage material candidates are listed in Table 1 below.

Table 1: Critical properties of storage material candidates.

Material	Critical temperature (°C)	Critical pressure (bar)	Critical density (kg/m³)
Naphthalene[8]	475	40.5	315.2
1-methylnaphthalene[8]	499	36.1	-
ortho-Xylene[8]	357	37.3	286.6
meta-Xylene[8]	345	35.4	283.4

148

para-Xylene[8]	344	35.1	281.3
Decane[8]	344	21.1	227.6
Biphenyl[8]	507	35.1	154.2
Tert-butylbenzene[8]	387	36.9	-

It is quite clear that no single material can fully satisfy the previously listed criteria. Therefore, trade-offs must be made in the selection of thermal storage material candidates. Naphthalene has been tested as a candidate for phase change materials (PCM) in thermal energy storage [10], but has been deemed impermissible due to the small difference between its melting point and flash point. In this design, the storage material will be encapsulated in storage tubes and evacuated of air, so the flash point is not a concern. To identify the best candidate, it is critical to understand the decomposition pathways that the organic fluids undergo at high temperatures. The mechanistic details of the thermal degradation will inform the fluid selection, as well as the design process.

EXPERIMENTAL PROCEDURE

Test Objectives

In this study, a series of experiments have been performed, either at the UCLA laboratory or JPL facilities, in order to determine the durability of the selected materials for prolonged lengths of time over a range of operating temperatures.

The experimental procedure combined pyrolysis methodology and thermal cycling. Pyrolysis observes the thermal decomposition pathways of organic materials at elevated temperatures, in the absence of oxygen. The pyrolysis of aromatic compounds remains actively studied due to their regular usage in many industrial processes. Additionally, typical TES systems operate for 10,000 cycles or more during a 30-year life of a power plant; thus, it is important to simulate a power plant environment if possible. This type of high-cycle thermal testing has been performed by Sandia National Laboratories for molten salt (Brosseau et al [11]) and by the University of Stuttgart for candidates for organic and inorganic PCMs (Abhat [12]). However, for the materials in this study, thermal cycling is less strenuous in comparison than for molten salt or PCMs, which undergo repeated melt-freeze cycles.

Apparatus

Figure 1 shows the schematic of the experimental apparatus. The tank and piping is constructed of 316 stainless steel with various fittings. The tank diameter is 7.62 cm (3 in) and the chamber can contain one liter of material. The tank is rated for temperatures up to 650°C and a maximum pressure of 275 bar. Similar to molten salt storage systems, heat tracing is installed to prevent freezing within the piping or other components when testing any materials that are

149

solid at room temperature (in particular, naphthalene and biphenyl). It is important to have a hermetic seal for testing volatile compounds like naphthalene, which is achieved with a stainless steel o-ring. Four gate valves are installed to purge the system with nitrogen at the beginning of every test, to minimize oxidative decomposition pathways. The nitrogen was bubbled through the liquid or melt from a stainless steel tube at atmospheric pressure. The tank is insulated with removable fiberglass material to minimize heat loss.

Because all but two of the storage material candidates are liquid at room temperature, the sample was inserted into the vessel through a charging port by syringe. In the case of naphthalene and biphenyl, the sample was ground using a mortar and pestle until it visibly became a fine powder, and then subsequently poured into the tank. The tank was pre-heated to 100 °C to melt the naphthalene so that nitrogen could be bubbled to better remove air from the vessel.
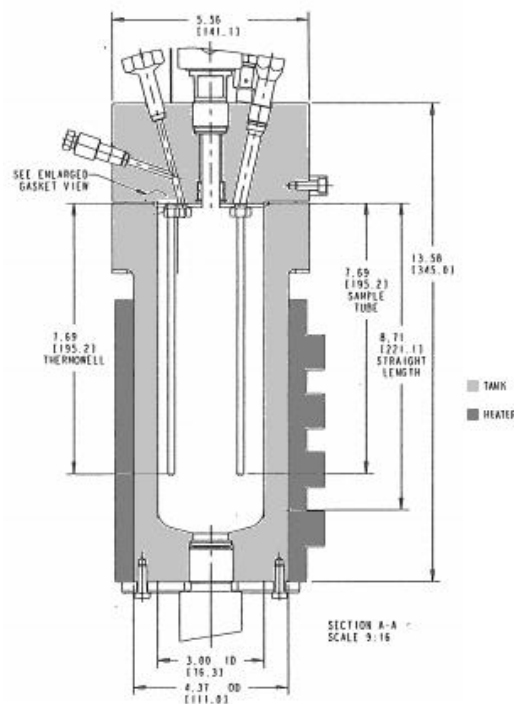
Figure 1: Dimensions of the one-liter vessel at UCLA.

Each test used a small sample of the candidate material, and was heated to critical temperature. However, in almost all cases, supercritical state was not achieved due to critical pressure not being met (due to the small volume of sample compared to the volume of the one-liter vessel). Samples were extracted at the end of each day to observe trends of thermal degradation. Upon test completion, analytical chemistry techniques were conducted to assess durability of each fluid. The sample purity was chosen to be commercial-grade to test fluids that would most likely be implemented into a TES system. The sample purity for each fluid is $\geq 99.00\%$. It is worth noting that other than the convective currents in the tank, the fluid was not mechanically stirred. This is to accurately simulate the conditions of the single-tank design [1], in which the storage fluid will be encapsulated in tube bundles. After each test was

150

completed, the vessel was cleaned in a heated bath with various solvents, including acetone, pentane, and dichloromethane, to prevent contamination from previous tests.

RESULTS AND DISCUSSION

The stability of these different compounds was studied using gas chromatography (GC) and ^{1}H nuclear magnetic resonance (NMR). The gas chromatogram obtained before and after heating were analyzed to verify that the qualitative ratio of the desired compound in the solution (each compound is pure at $\geq$ 99.00%) does not change during the experiment. This piece of information is given qualitatively by the area percentage of the biggest signal. The NMR spectra were studied in order to dee the apparition of an eventual new signal that would indicate the formation of a side-product during the heating/cooling cycle. These analyses were able to give qualitative insights on the stability of these compounds. The role of the rapid screening being the preliminary filter of adequate candidates for longer stability studies, the spectra and chromatograms obtained helped us decide which compounds to choose for further testing.

Naphthalene

The results obtained for naphthalene are presented in Figure 2. Naphthalene exhibited suitable thermal stability, with no residual pressure. The initial sample under thermal testing was 93 grams. The heating cycle is shown in Figure 3, with the reduced temperature and reduced pressure. These are interesting because near the reported critical point of the fluid, the observed temperature and pressure initially decrease, then continue increasing.

(a)

151

RT   AREA   AREA%
6.286   521005   99.26400
6.375   2452   .46716
10.790   1411   .26883
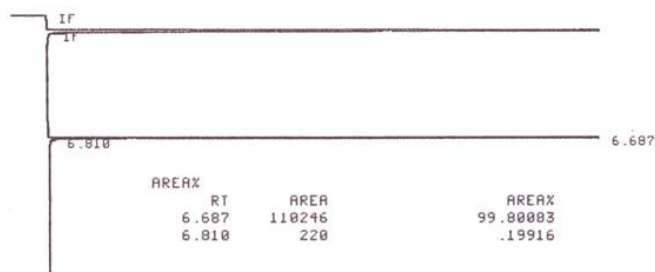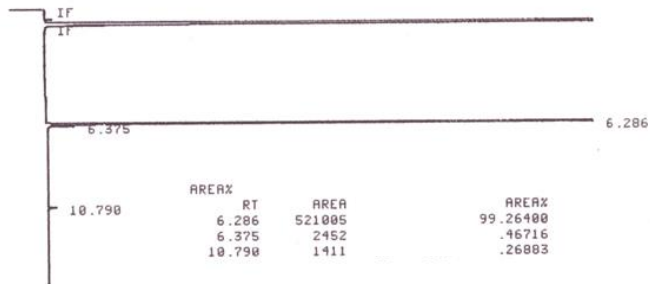
(b)

Figure 2: Gas chromatogram of naphthalene obtained a) before and b) after heating.
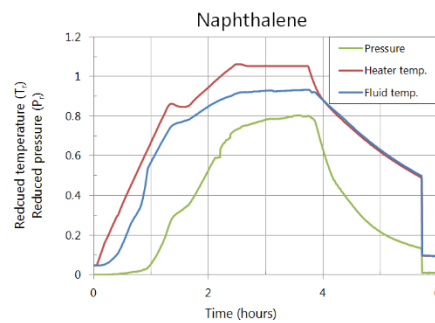
Figure 3: Heating cycle of naphthalene.

1-methylnaphthalene

The post-test gas chromatography results obtained for 1-methylnaphthalene are presented in Figure 4. The initial sample was 100 grams. Changes in the feedback loop of the temperature controller caused the heater temperature to cascade, but this was remedied in future tests. This is shown in the heating cycle (Figure 5), with the reduced temperature and reduced pressure. The gas chromatogram for 1-methylnaphthalene revealed the appearance of a new signal. It is noteworthy to indicate that out of all the test fluids, 1-methylnaphthalene showed the strongest change in color after heating.

152

(a)

(b)

Figure 4: Gas chromatogram of 1-methylnaphthalene obtained a) before and b) after heating.
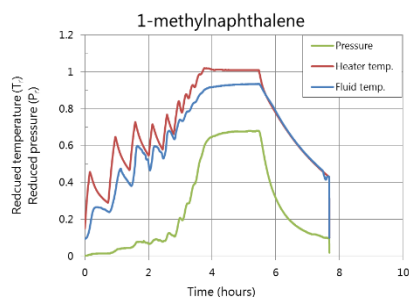
Figure 5: Heating cycle of 1-methylnapthalene.

Xylene (*ortho-, meta-, para-*)

***para*-Xylene:** The initial quantity of *p*-xylene was 100 grams. Zero residual pressure was observed, and all three forms of xylene displayed minimal thermal degradation, which is illustrated in the gas chromatograms obtained for *p*-xylene in Figure 6. Similarly, the observed temperature and pressure initially decreased, then increased, near the critical point of xylene. This can be seen in the heating cycle of *p*-xylene, shown in Figure 7.

153

*ortho-, meta-***Xylene:** The initial quantity of each isomer of xylene was 100 grams. However, because all three cases exhibited similar behavior, only the results for *p*-xylene are shown.
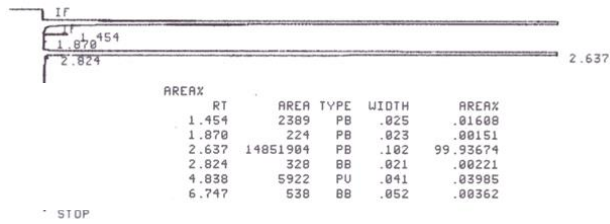
(a)
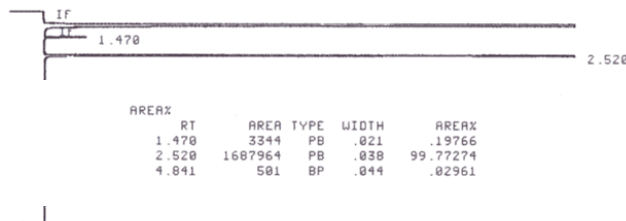
(b)

Figure 6: Gas chromatogram for *p*-xylene obtained (a) before heating, and (b) after heating.
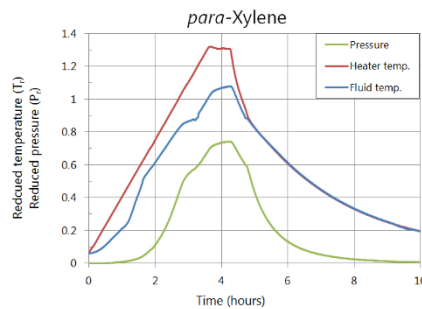
Figure 7: Heating cycle of *p*-xylene.

Decane

While decane showed initial promise due to its wide availability and attractive thermophysical properties, it did not illustrate adequate thermal stability, as shown in Figure 8. The initial sample was 100 g, and 4 g of sample was extracted at the end of the experiment. The heating cycle is shown in Figure 9.

154

AREA%

RT	AREA	TYPE	WIDTH	AREA%
2.589	775	BV	.046	.03008
2.756	6844	UP	.047	.26559
3.324	2564226	PB	.070	99.50925
15.532	5027	PU	.088	.19508

(a)

AREA%

RT	AREA	TYPE	WIDTH	AREA%
1.679	480	PU	.037	.02910
2.563	467	VV	.046	.02831
2.730	4162	UP	.047	.25228
3.278	1642222	PB	.062	99.54483
15.543	2400	PP	.089	.14548
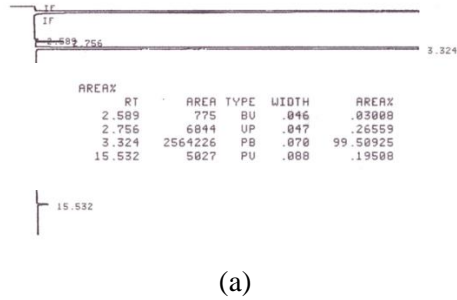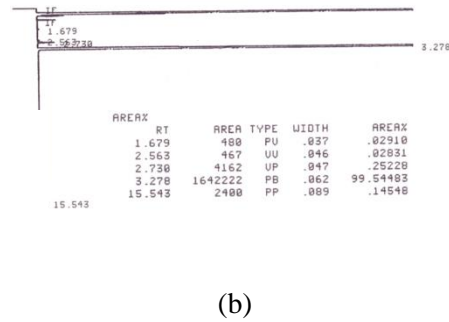
(b)

Figure 8: Gas chromatogram of decane obtained a) before and b) after heating.
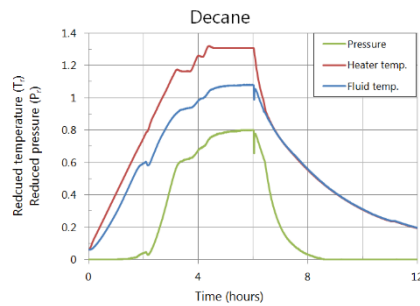
Figure 9: Heating cycle of decane.

Biphenyl

The initial sample was 115 grams, and is solid at room temperature. Biphenyl was of particular interest because, like naphthalene, it has low vapor pressure. Biphenyl was the first test fluid examined using NMR; the results are show in Figure 10. Biphenyl exhibits minimal thermal degradation, but it is important to note that the presence of polymers was not able to be detected with current analysis. The heating cycle of biphenyl is shown in Figure 11.

155
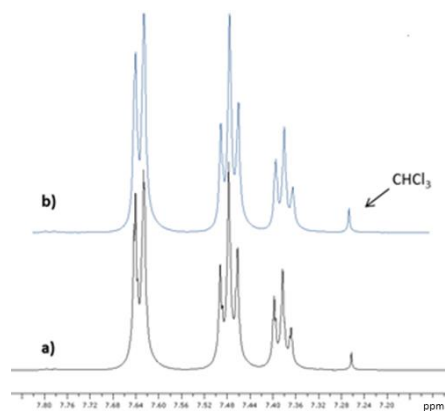
Figure 10: ^{1}H NMR spectra of biphenyl obtained a) before and b) after heating.
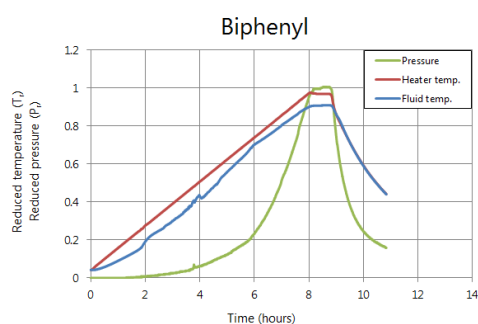
Figure 11: Heating cycle of biphenyl.

Tert-butylbenzene

The thermal stability of *tert*-butylbenzene is illustrated in Figure 12. The initial sample was 100 grams. Zero residual pressure was observed, but moderate thermal decomposition was shown. Given the stability of other candidates, *tert*-butylbenzene was not selected for further testing. The heating cycle is shown in Figure 13.
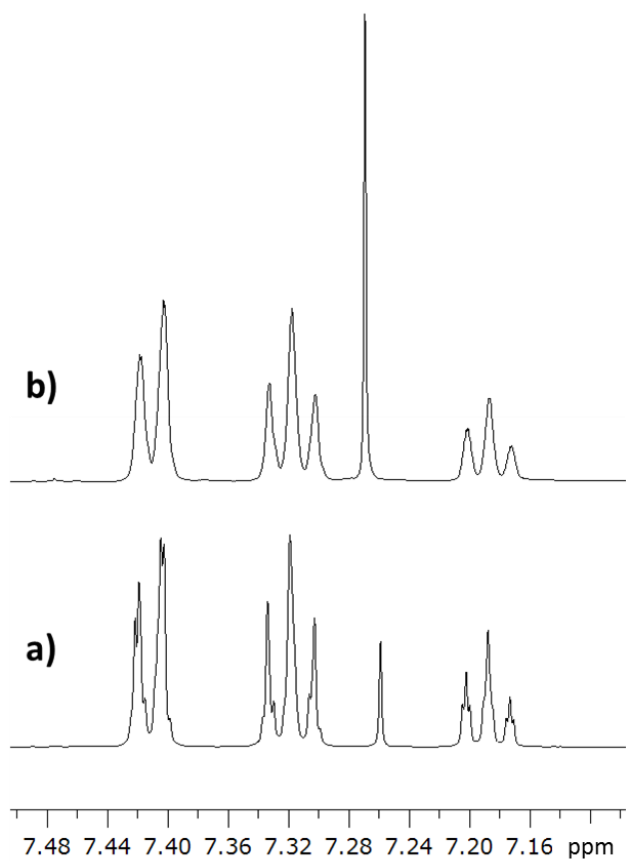
Figure 12: Zoom on the aromatic section of the ^{1}H NMR spectra of *tert*-butylbenzene obtained a) before and b) after heating.
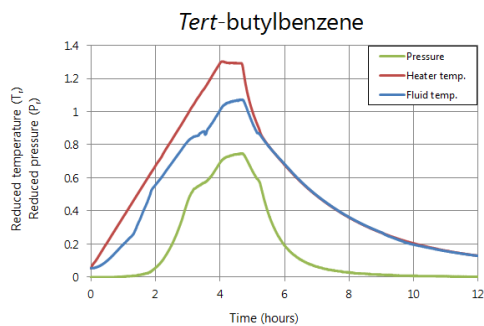
Figure 13: Heating cycle of *tert*-butylbenzene.

CONCLUSION

At the completion of the rapid screening phase, naphthalene and *p*-xylene appear durable enough to be prime candidates for further testing. The decomposition of these two compounds appears to be minimal (less than 1 % after the rapid screening) and would not impact its storage capability or the operation of the thermal storage unit. They are slated for further examination, such as more rigorous thermal cycling, and corrosion testing for materials compatibility.

These experiments were conducted using commercial-grade materials, which are the probable grade of storage fluids that would be implemented in a TES system. In a few cases, further tests can be done using lower-purity materials, which can be significantly less expensive (such as brown, or crude, naphthalene). This will provide insight into opportunities for lowering cost.

ACKNOWLEDGEMENTS

REFERENCES

1. Raade, J., Padowitz, D., 2011. "Development of Molten Salt Heat Transfer Fluid with Low Melting Point and High Thermal Stability," Journal of Solar Energy Engineering, Vol. 133, 3, pp. 31013.
2. Bradshaw, R.W., Siegel, N.P. "Molten Nitrate Salt Development for Thermal Energy Storage in Parabolic Trough Solar Power Systems," Proceedings of the ASME 2012 2nd International Conference on Energy Sustainability, August 10-14, 2008, Jacksonville, Florida, USA.
3. Trahan, J., Kuravi, S., Goswami, Y., Rahman, M., Stefanakos, E. "Thermal Characterization of High Temperature Inorganic Phase Change Materials for Thermal Energy Storage Applications," Proceedings of the ASME 2012 6th International Conference on Energy Sustainability, July 23-26, San Diego, CA, USA.
4. Pincemin, S., Olives, R., Py, X., Christ, M., 2008. "Highly conductive composites made of phase change materials and graphite for thermal storage," Journal of Solar Energy Materials and Solar Cells, 92, pp. 603-613.
5. Kelly, Bruce. "Advanced Thermal Storage for Central Receivers with Supercritical Coolants," DOE Grant DE-FG36-08GO18149, Abengoa Solar Inc., Lakewood, CO, June 15, 2010.
6. Ganapathi, G.B., Wirz, R.E. "High density Thermal Energy Storage with Supercritical Fluids", ASME 2012 6th International Conference on Energy Sustainability, July 23-26, San Diego, CA, USA.
7. Ganapathi, G. B., Berisford, D., Pauken, M., Wirz, R.E. "A 5 kWh Lab Scale Demonstration of a Novel Thermal Energy Storage Concept with Supercritical Fluids," ASME 6th International Conference on Energy Sustainability, July 23-26, 2012, San Diego, California, USA.
8. Tsonopoulos, C., Ambrose, D. "Vapor-Liquid Critical Properties of Elements and Compounds. 3. Aromatic Hydrocarbons." J. Chem. Eng. Data, 1995, 40, 547-558.
9. Kay, W.B., Pak, S.C. "Determination of the critical constants of high-boiling hydrocarbons. Experiments with gallium as a containing fluid." J. Chem. Thermodyn., 1980, 12, 673.
10. Arndt, P.E., Dunn, J.G., Willix, R.L.S., 1984. "Organic Compounds as Candidate Phase Change Materials in Thermal Energy Storage," Elsevier, Thermochimica Acta, 79, pp. 55-68.
11. Brosseau, D., Kelton, J. W., Ray, D., Edgar, M., Chisman, K., and Emms, B., 2005, "Testing of thermocline filler materials and molten-salt heat transfer fluids for thermal energy storage systems in parabolic trough power plants," Journal of Solar Energy Engineering, Transactions of the ASME, 127, pp. 109-116.
12. Abhat, A., 1982. "Low temperature latent heat thermal energy storage: heat storage materials," Journal of Solar Energy, Vol. 30, 4, pp. 313-332.

Appendix C: s-CO₂ Power Cycle Modeling

ANALYSIS AND OPTIMIZATION FOR OFF-DESIGN PERFORMANCE OF THE RECOMPRESSION sCO2 CYCLES FOR HIGH TEMPERATURE CSP APPLICATIONS

Louis A. Tse
Department of Mechanical and Aerospace Engineering
University of California, Los Angeles
Los Angeles, CA, USA

Ty Neises
National Renewable Energy Laboratory
Golden, CO 80401

ABSTRACT
This study investigates optimal design and operation of supercritical carbon dioxide (sCO2) power cycles for concentrating solar power (CSP) applications. Previous design-point and off-design studies have supported the potential efficiency improvements and established broad operating conditions for the sCO2 power cycle at temperatures pertinent to CSP applications. This study investigates a simple/recompression sCO2 cycle integrated with molten salt heat source and maximizes cycle efficiency for off-design operation. The findings of this study report optimal operating parameters under off-design conditions and provide an understanding of the effect of cycle parameters on other primary subsystems in a CSP plant.

INTRODUCTION
Concentrating solar power utilizes solar beam irradiance to produce heat for a thermodynamic power cycle. Consequently, CSP employs power cycle concepts similar to those found in coal and nuclear power plants. Previous studies have suggested that the sCO2 power cycle has the potential to replace the steam-Rankine cycle for at least some CSP configurations [85, 86, 133, 167]. Researchers in fossil, nuclear, waste heat, and other application spaces have studied cycle component design and manufacturing and cycle design and operation. This research informs the

159

CSP community about the cycle; however, CSP presents its own unique challenges in designing and operating a power cycle.

One typical CSP system configuration is to capture the solar heat with a fluid that can be stored. Typically the storage fluid stores the thermal energy over a temperature gradient. As such, the volume of fluid required is proportional to the temperature gradient of the cycle's heat input. Therefore, all else equal, design and operation strategies that create a larger temperature gradient are preferred. Thermal storage allows the plant operator to decide when to dispatch the stored, hot fluid to the power cycle to generate electricity. This capability allows CSP plants to increase revenue potential by generating electricity during peak demand, with these peak pricing periods often coincide with hot, summer afternoons. Furthermore, locations with the best solar resource typically prohibit evaporative cooling. Therefore, it is paramount that the power cycle is designed to achieve high performance with hot compressor inlet temperatures. Additionally, some CSP design and operation strategies require that part-load operation is understood.

While researchers are interested in the sCO2 concept for both CSP and traditional heat sources, CSP and nuclear power cycle configurations differ from coal and natural gas cycles in that the heat source is a heat flux instead of a sensible heat source (i.e. waste heat and combustion gas heating). The result of this difference is that CSP and nuclear sCO2 cycles are designed to limit the temperature range at which thermal energy is injected to the cycle, with a general goal to balance a hot average injection temperature with a reasonable power density. Two of the most common cycle configurations for flux based applications are shown in Figure 1. The simple, recuperated cycle (a) is the least complex but least efficient configuration. Many publications detail the benefit of adding a recompressor (b) to the simple cycle. Essentially, the recompressor facilitates more effective heat exchange in the low-temperature recuperator, resulting in better recuperation and a more efficient cycle. The trade-off is that the recompressor consumes work from cycle. While research at NREL and other institutions has suggested that the partial cooling cycle may offer additional benefits over the recompression cycle [167], this paper focuses on the recompression cycle because it is the most likely near-term, high efficiency solution.

160
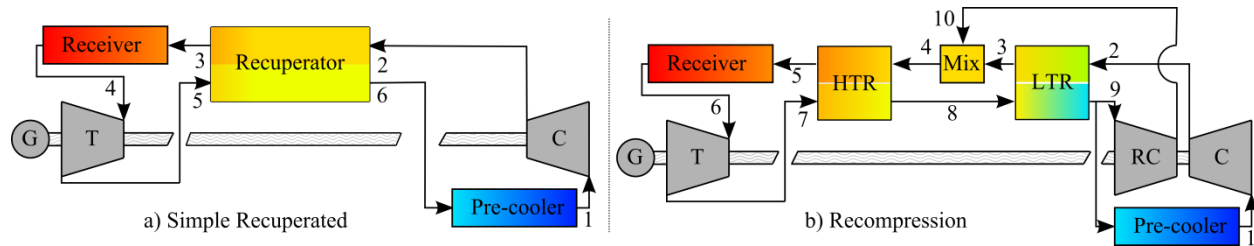
Figure 1: Common sCO2 cycle configurations for flux based heat sources.

Dyreby [77] presented an extensive investigation of the off-design performance of the simple and recompression cycles. The study assumed a generic heat input into the cycle to stay relevant to all applications. The analysis studied several cycle designs. One primary design choice studied was the design-point compressor inlet temperature, which subsequently influences recuperator conductance, turbomachinery sizing, and thermal efficiency. The study strongly suggests that for power cycles expected to operate under off-design conditions, as would be the case for CSP applications, a relatively hot compressor inlet temperature is preferred, especially when considering simple cycles. On the other hand, the study shows that the low-temperature compressor inlet recompression design can be advantageous if the cycle will rarely experience off-design operation. This could occur for applications with a fairly consistent heat sink, e.g. a large body of water utilized for once-through cooling.

This study builds on Dyreby's work by integrating his model with a hot molten salt heat source. This extension enables analysis of issues unique to CSP. Specifically, this study varies the off-design compressor inlet temperature and molten salt mass flow rate and temperature to investigate: 1) cycle design and off-design performance when the heat input source and heat exchanger are defined, 2) the potential impact on molten salt cold return temperature when off-design performance is optimized, and 3) estimated annual efficiencies for two different design compressor inlet temperatures.

MODELING APPROACH

This study uses two design point and two off-design models to generate results of a sCO2 recompression cycle configured for CSP applications. As such it's important to document each model's input parameters, solution, and interaction with other models. Figure 2 shows this information at a high level and differentiates between *cycle* models developed by Dyreby [77] and

161

application models we developed for CSP analysis. The following subsections provide more detail for each model, with a focus on the *application* modeling additions.
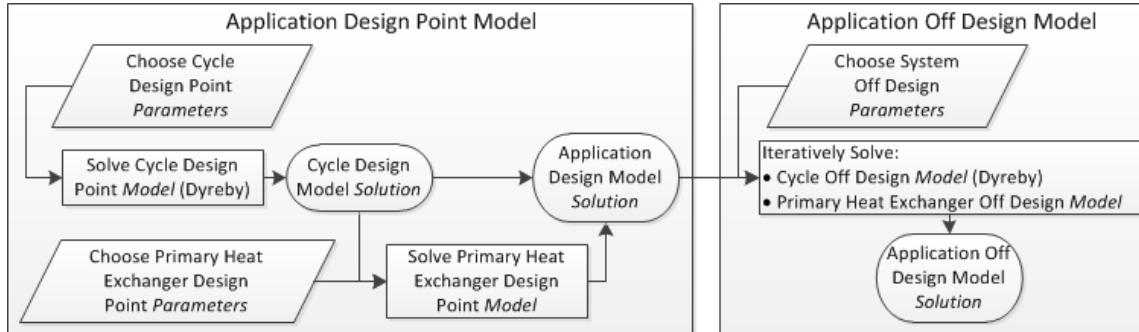
Figure 2: Modeling information flow diagram for the design point and off design models.

CYCLE DESIGN POINT MODEL

The cycle design point model uses equipment and operational parameters to find the combination of compressor inlet pressure, pressure ratio, and recompression fraction that results in the smallest recuperator conductance while still achieving the target cycle thermal efficiency. The model then uses this information to size the turbomachinery. More detailed description of this model is provided by Dyreby [77]. Table 1 describes the parameters and solution values, with numbers from our baseline case.

The compressors and turbine all have independent shafts in this configuration. The turbine shaft speed is fixed to 3,600 rpm for a grid-connected synchronous generator. The model assumes that the shaft speed of each compressor is independently adjustable.

Table 1: Cycle design point model parameters and solution results. Numbers in this table represent the design used in the following discussion.

Design Point Parameters			Optimized Design Point Parameters		
Net Power Output	10	MW	Comp. Inlet Pressure	9.00	MPa
Thermal Efficiency (no cooling)	0.48	-	Comp. Pressure Ratio	2.74	-
Turb. Inlet Temp	690	°C	Recompression Fraction	0.18	-
Turb. Isentropic Efficiency	0.93	-	**Design Point Solution Results**		
Turb. Shaft Speed (fixed)	3600	rpm	Recuperator Conductance	1375	kW/K
Main Comp. Inlet Temp	45	°C	Recuperator NTU	13.27	
Comp. Isentropic Efficiency	0.89	-	Main Comp. Shaft Speed	33294	rpm

162

Maximum Pressure	25	MPa	Turb. Rotor Diameter	2.32	m
Neglecting Pressure Drops			CO2 Mass Flow Rate	82.0	kg/s
			PHX CO2 Inlet Temperature	505	°C

CYCLE OFF-DESIGN MODEL

The cycle off-design model uses design point solution results that describe component design to predict the cycle performance when the off-design parameters vary from their design values. For example, the off-design compressor uses the design compressor rotor diameter and design efficiency along off-design parameters compressor shaft speed and compressor inlet temperature to calculate the compressor outlet pressure, isentropic efficiency, and power consumption. As with the cycle design point model, Dyreby [77] provides a more detailed description of this model. Table 2 lists the required cycle design point solution results, parameters, and results for the off-design model. The off-design model optimizes the compressor shaft speed, main compressor inlet pressure, and the recompression fraction off-design parameters to maximize the cycle thermal efficiency.

Table 2: Cycle off-design model required design point solution results, parameters, and solution results. Numbers in this table are selected from the off-design analysis presented in the following discussion.

Required Design Point Solution Results	Off-Design Parameters			Off-Design Results		
Recuperator Conductance	Turb. Inlet Temp	687	°C	Net Power Output	9.30	MW
Turb Isen Efficiency	Comp. Inlet Temp	50	°C	Thermal Efficiency	0.47	-
Turb. Rotor Diameter	**Optimized Off-Design Parameters**			PHX CO2 Inlet Temp.	510	°C
Comp. Isen Efficiency (2)	Main Compressor Shaft Speed	36523	rpm	Pressure Ratio	2.73	-
Comp. Rotor Diameter (2)	Main Compressor Inlet Pressure	9.0	MPa	CO2 Mass Flow Rate	82.9	kg/s
Maximum Pressure	Recomp. Fraction	0.17	-			
Component Pressure Drops						

163

PRIMARY HEAT EXCHANGER DESIGN POINT MODEL

We are modeling the primary heat exchanger as a counter-flow molten salt to CO2 heat exchanger. The goal of the design point model is to use information from the cycle design point solution and the molten salt hot inlet temperature to calculate the required conductance (UA) of the primary heat exchanger. We set the capacitance ratio (CR) at design to 1.0, thereby ensuring that the molten salt and CO2 streams both experience the same inlet-to-outlet temperature differential. Then, we calculate the maximum possible heat transfer in the heat exchanger using Equation (1). Next, we find the heat exchanger effectiveness by dividing the actual heat transfer by the maximum heat transfer. Finally, we calculate the UA using Equation (2).

$$\dot{q}_{max} = (\dot{m}cp)_{CO_2,des} \cdot (T_{HTF,hot} - T_{CO_2,PHX,in}) \tag{1}$$

$$UA_{des} = \frac{\varepsilon}{1-\varepsilon}(\dot{m}cp)_{CO_2,des} \tag{2}$$

Table 3 shows the required *cycle* design point solution results, the primary heat exchanger design point parameters, and the primary heat exchanger design point solution results. Note that one outcome of fixing the CR is that the design heat transfer fluid (HTF) mass flow rate is a *dependent* variable calculated by the primary heat exchanger design point model, while the HTF temperature is a design parameter. Alternatively, we could specify the HTF mass flow rate and let the CR vary, but that allows for the potential of a significantly unbalanced heat exchanger that could result in suboptimal *application* design. Ultimately, the optimal CR is a function of heat exchanger and system costs and performance, and is outside the scope of this paper.

Table 3: Primary heat exchanger model required *cycle* design point solution results, design point model parameters, and solution results. Numbers in this table represent the design used in the following discussion.

Required Design Point Solution Results	Design Point Parameters		Design Point Solution Results		
PHX CO2 Inlet Temperature	HTF Inlet Temp	700 °C	PHX Conductance	2.9×10^5	kW/K
Turb. Inlet Temp			PHX NTU	9.39	
CO2 Mass Flow Rate			HTF Mass Flow Rate	72.4	kg/s

164

PRIMARY HEAT EXCHANGER OFF-DESIGN MODEL

During off-design operation, we know the cold CO2 inlet and hot HTF inlet temperatures and mass flow rates, and we want to solve for the outlet temperature of both streams. Because both the mass flow rates can be different than their respective design point values, the convective heat transfer coefficient, and therefore the conductance, of the heat exchanger can vary. We estimate the off-design overall heat transfer coefficient, U, using Equation (3), based upon the Dittus-Boelter correlation for the effect of mass flow rate on heat transfer coefficient (Patnode [90]). Next, we calculate the off-design capacitance ratio using Equation (4). Then, we apply Equation (5) to find the NTU. Next, we find the off-design effectiveness using Equation (6). Finally, Equation (7) uses the effectiveness to calculate the off-design heat transfer, which we use to calculate the outlet temperatures. Table 4 lists the required *PHX* design point solution results, required *cycle* off-design solution results, parameters, and results for the PHX off-design model.

$$U = U_{des}\left(\frac{1}{2}\left(\frac{\dot{m}_{CO_2}}{\dot{m}_{CO_2,des}} + \frac{\dot{m}_{HTF}}{\dot{m}_{HTF,des}}\right)\right)^{0.8} \tag{3}$$

$$C_R = \frac{\dot{C}_{min}}{\dot{C}_{max}} = \frac{\min\left(\left[(\dot{m}c_p)_{CO_2}\right],\left[(\dot{m}c_p)_{HTF}\right]\right)}{\max\left(\left[(\dot{m}c_p)_{CO_2}\right],\left[(\dot{m}c_p)_{HTF}\right]\right)} \tag{4}$$

$$NTU = \frac{UA}{\dot{C}_{min}} \tag{5}$$

$$\varepsilon = \begin{cases} \dfrac{1-\exp\left(-NTU\left(1-C_R\right)\right)}{1-C_R\exp\left(-NTU\left(1-C_R\right)\right)}, & \left(for\ C_R < 1.0\right) \\ \dfrac{NTU}{1+NTU}, & \left(for\ C_R \geq 1.0\right) \end{cases} \tag{6}$$

165

$$\dot{Q}_{PHX} = \varepsilon \dot{C}_{min} \left(T_{HTF,hot} - T_{CO_2,PHX,in} \right) \tag{7}$$

Table 4: Primary heat exchanger off-design model required *PHX* design point solution results, required *cycle* off-design solution results, off-design parameters, and off-design results. Numbers in this table are selected from the off-design analysis presented in the following discussion.

Required *PHX* Design Point Solution Results	Required *Cycle* Off-Design Solution Results		Off-Design Results	
PHX Conductance	PHX CO2 Inlet Temp.	510 °C	Turb. Inlet Temp	687 °C
HTF Mass Flow Rate	CO2 Mass Flow Rate	82.9 kg/s	HTF Return Temp	520 °C
	Off-Design Parameters			
	HTF Inlet Temp	700 °C		

SOLVING THE APPLICATION OFF-DESIGN MODEL

We described above that the cycle design point model is solved independently of and before the primary heat exchanger design point model, because the design of the cycle informs the design of the heat exchanger. However, Figure 2 shows that for the off-design application model, the primary heat exchanger and cycle solutions are coupled and must be solved iteratively, as illustrated in Figure 3. The turbine inlet temperature is a function of the molten salt inlet temperature and mass flow rate, and the CO2 inlet temperature and mass flow rate to the primary heat exchanger. If all other off-design parameters in Table 2 are known, then setting the turbine inlet temperature will constrain the off-design performance. However, the off-design performance determines the CO2 inlet temperature and mass flow rate to the primary heat exchanger. Therefore the problem is iterative, and for each unique set of off-design parameters there is only one turbine inlet temperature that results in the correct primary heat exchanger behavior (i.e. calculated conductance equal to actual conductance).

166
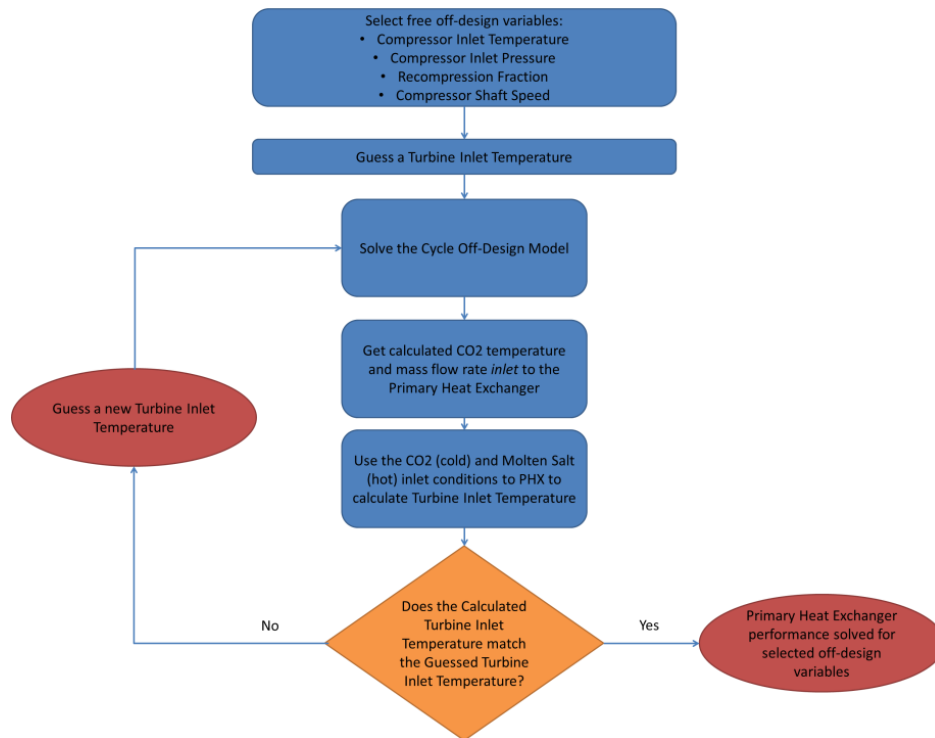
Figure 3: Information flow diagram for Primary Heat Exchanger convergence.

OFF-DESIGN PERFORMANCE ANALYSIS

To assess the integration of the sCO2 cycle into CSP applications, the inclusion of the primary heat exchanger model is necessary because it provides several important parameters. Firstly, the cycle model considers an agnostic heat source input into the CO2 stream. With the addition of the PHX model, the salt-to-CO2 approach temperature may provide an equivalent heat input to the cycle model, but at a turbine inlet temperature different from that at design, thereby affecting efficiency. Secondly, optimizing cycle efficiency with the addition of a PHX model may result in a HTF cold temperature that deviates from design-point value. Warmer HTF cold temperatures are of particular concern, as this effectively reduces thermal energy storage capacity (which is dependent upon a temperature differential), and impacts fluid flow through the receiver, and may risk venturing into unfavorable HTF property regimes.

As described in previous sections, previous studies have explored the *cycle* off-design behavior when turbine inlet temperature, heat input, and compressor inlet temperature vary. This section aims to investigate the interaction between cycle and heat exchanger parameters, and the relative magnitude of multiple parameters simultaneously experiencing off-design conditions on cycle efficiency. Table 5 describes the range of off-design conditions for each off-design parameter in

167

the following analysis. The cycle design point is described in Table 1 and Table 2, while an off-design example solution is shown in Table 3 and Table 4.

Table 5: Design-point values for the baseline system under study.

Primary parameter	Design-point value	Range	Secondary parameter values
$T_{htf,hot}$	700	500 – 800	$T_{mc,in}$ = 35, 45, 55
$\dot{m}_{htf,frac}$	1.0	0.6 – 1.2	$T_{htf,hot}$ = 675, 700, 725
$T_{mc,in}$	45	35 – 50	$\dot{m}_{htf,frac}$ = 0.6, 1.0, 1.2

The results from the off-design performance analysis are shown in Figure 4. The thermal efficiency is normalized by the design-point value. Figure 4a shows that operating at warmer compressor inlet temperatures decreases thermal efficiency appreciably. It is also important to note that Dyreby's design-point analysis shows the slope of the efficiency curve is much steeper for designs with colder main compressor inlet temperature. For example, the baseline design-point value for the compressor inlet temperature is 45°C, which is relatively warm; if the system were designed for a colder compressor inlet temperature, the slope would be steeper at warmer temperatures.

Figure 4b illustrates the impact of mass flow fraction on off-design performance. As the mass flow fraction decreases to 60% of its design-point value, off-design thermal efficiency decreases by approximately 5%. Lower mass fractions essentially translate to reduced heat input into the cycle, and compressor speed and inventory control are able to compensate to a certain degree to maximize off-design thermal efficiency.

Finally, Figure 4c describes the effect of HTF hot temperature during off-design conditions, which typically occur during periods of cloud cover or nighttime, or when thermal storage is unavailable. One important observation is that for this baseline system, HTF hot temperature is the parameter with the most markedly dramatic shifts during off-design operation. Of course, one important driver of this trend is the Carnot limit. The results in Figure 4c clearly illustrate that the optimal

168

plant operation (to maximize efficiency) must focus upon achieving design-point HTF hot temperature. In existing systems, this is achieved in a number of ways, including varying HTF mass flow rate to the solar field, implementing fossil backup or thermal storage, and increasing the solar multiple of the plant. However, this analysis does not consider the disadvantages of these plant designs which must be balanced with cycle performance.

(a)

(b)

(c)
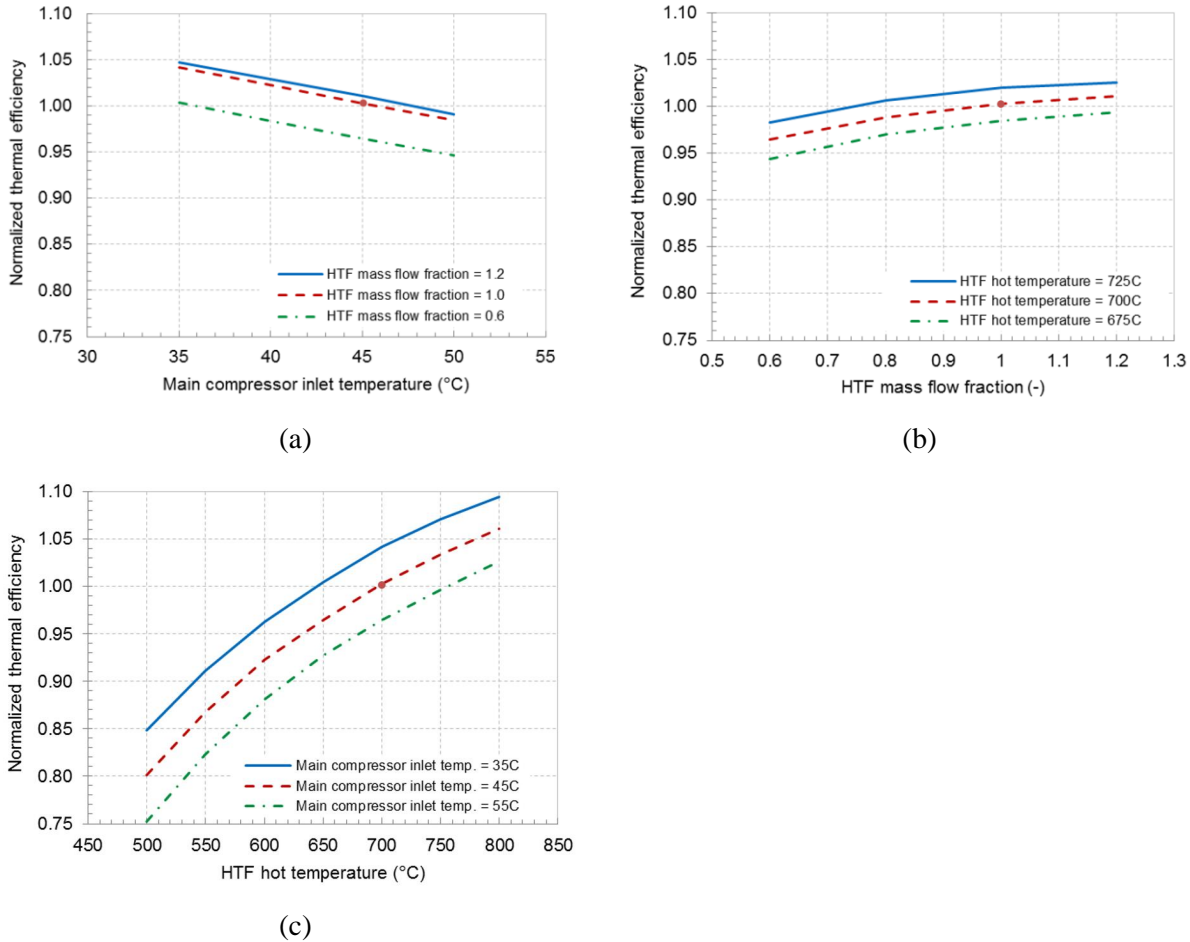
Figure 4: Design of experiments study of various off-design (OD) conditions, investigating the main and interaction effects: a) main compressor inlet temperature, b) mass flow fraction, and c) HTF hot temperature. Design-point values are given by the dot.

Because CSP applications are expected to be dry-cooled in hot climates, off-design performance at warmer compressor temperatures is of particular interest. Further, the HTF cold temperature is also important for CSP applications because of its significance to other CSP plant components,

169

such as the thermal storage and receiver subsystems, both of which are designed to operate for a specific temperature differential. Should the HTF cold temperature increase during off-design operation the overall storage capacity is lessened. Figure 5a shows the HTF cold temperature as a function of main compressor inlet temperature. One key observation is the HTF cold temperature increases substantially for mass flow fractions below design-point, which can occur with varying frequency depending on the plant's thermal storage capacity and operation strategy. Also important to note is that the HTF cold temperature can increase appreciably for warmer compressor inlet temperatures. Figure 5b shows the HTF temperature differential normalized to the design-point value, and suggests that storage capacity at part load is roughly 80% of the design capacity. This conclusion, along with decreased part load efficiencies, may influence the plant operation strategy to focus on full load storage dispatch to the power cycle.

(a)   (b)
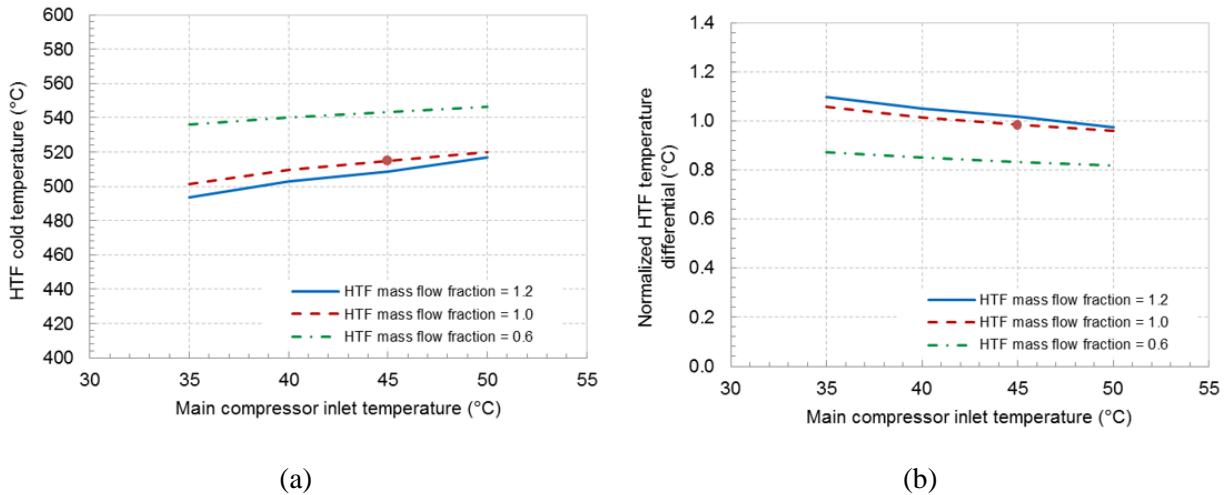
Figure 5: HTF cold temperature and normalized HTF temperature differential across the primary heat exchanger as a function of main compressor inlet temperature.

Probabilistic performance analysis

Off-design performance across an annual basis is critical to evaluating the technical and economic feasibility of the system. As shown in the previous section, main compressor inlet temperature is highly influential for off-design thermal efficiency. In this analysis, we assume that the cooling system can maintain a constant temperature differential of 15°C such that

170

$$T_{mc,in} = \max(T_{amb} + 15^\circ C, \ 31^\circ C) \tag{8}$$

with the minimum of 31°C to stay above the critical point of CO_2, and the parasitic load of the cooling fan being neglected for this study. To estimate the performance of the cycle on an annual basis, hourly DNI and ambient temperature data can be incorporated into the analysis by using a probability distribution function (PDF) to quantify the probability of achieving performance or cost targets. The PDF of the ambient temperature and DNI weighted ambient temperature compiled from the Typical Meteorological Year (TMY2) weather dataset for Daggett, CA is shown in Figure 6. The DNI weighted ambient temperature probabilities represent more realistic conditions for CSP power cycle operation, as current conventional wisdom expects CSP plants generate electricity during peak pricing periods rather than operate as baseload plants. Note that, as expected, the DNI weighted probabilities are shifted towards warmer temperatures.

Ambient temperature (°C)	Ambient temperature-weighted probability	DNI-weighted probability
-7.5°C	0.02%	0.00%
-2.5°C	0.78%	0.05%
2.5°C	4.45%	0.87%
7.5°C	12.80%	4.50%
12.5°C	17.47%	11.72%
17.5°C	17.67%	16.54%
22.5°C	16.34%	18.17%
27.5°C	14.42%	18.55%
32.5°C	9.26%	14.83%
37.5°C	5.76%	12.35%
42.5°C	1.04%	2.42%
Average annual temperature (°C)	19.5°C	24.3°C
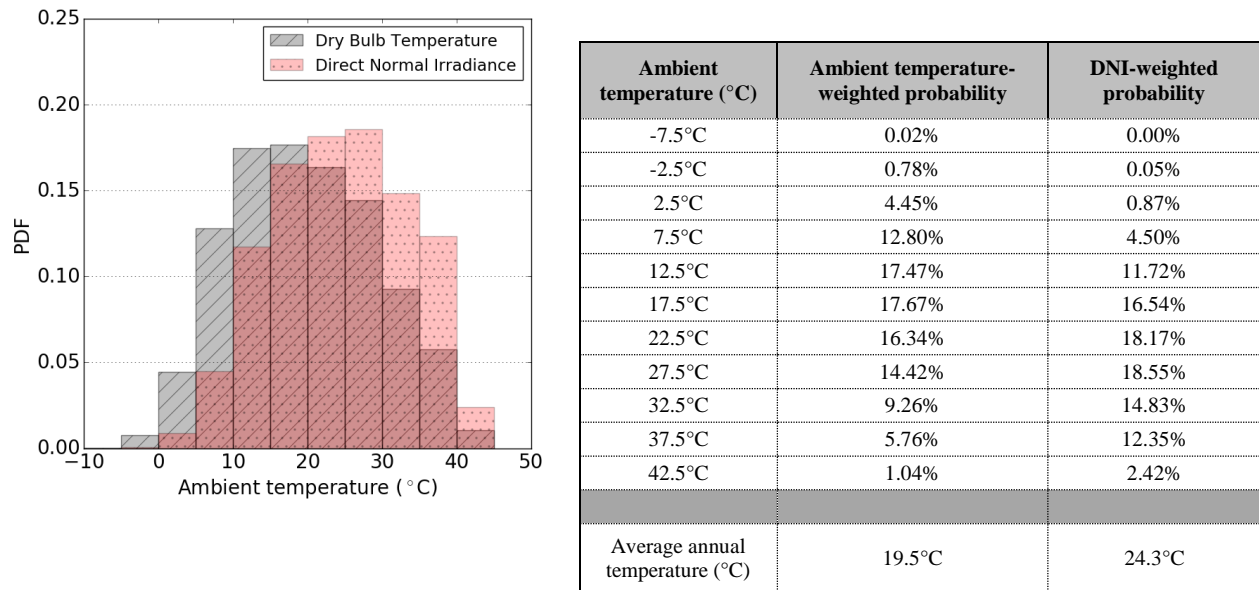
Figure 6: Probability density function of ambient temperature-weighted and direct normal irradiance-weighted probability, with a table of probability values located at the midpoint of each bin.

Then, based upon the probability distribution that the s-CO2 cycle will experience a variable main compressor inlet temperature throughout the year, we can assess annual performance by combining the modeled off-design efficiency at each temperature with its associated probability.

171

In addition to the baseline cycle design, another cycle design is considered for comparative analysis. The baseline cycle is designed for 35°C main compressor inlet temperature, which results in design values outlined in Table 1. The second cycle design being considered has a design-point of 45°C for main compressor inlet temperature. To put both designs on equal footing, they maintain the same heat exchanger thermal conductance as the baseline design. The results from this analysis are detailed in Table 6.

Table 6: Results of the probabilistic modeling for off-design main compressor inlet temperature using DNI-weighted dry-bulb temperature from Daggett, CA, with design-point efficiencies denoted by (*).

Ambient temperature (°C)	Design-point Thermal Efficiency		
	Compressor inlet temperature 35°C (51.4%*)	Compressor inlet temperature 40°C (49.6%*)	Compressor inlet temperature 45°C (48.0%*)
-10°C – 15°C	52.6%	51.6%	50.6%
17.5°C	52.2%	51.3%	50.3%
22.5°C	51.0%	50.3%	49.4%
27.5°C	48.1%	49.2%	48.6%
32.5°C	46.4%	47.8%	47.9%
37.5°C	44.6%	46.8%	46.9%
42.5°C	42.8%	45.9%	46.0%
Annual parameters			
Ambient temperature-weighted annual efficiency (-)	50.5%	50.3%	49.5%
Direct normal irradiance-weighted annual efficiency (-)	49.3%	49.6%	48.9%

172

The results observed in Table 6 support and expand upon the results of both the design-point and off-design analysis. The system designed for 35°C compressor inlet temperature can achieve a maximum thermal efficiency of 52.6% yet drops to 42.8% during periods of high ambient temperature, while the system designed for 45°C compressor inlet temperature can achieve between 45.9%-50.6% for the same ambient temperature range. Incorporating the probability distribution for the entire year to calculate annual thermal efficiency weighted by ambient temperature or direct normal irradiance, the system designed for 35°C compressor inlet temperature achieves higher performance. However, it is clear that considering the DNI-weighted ambient temperatures resulting in the 45°C design being relatively more competitive with the 35°C design, and it is likely that a design temperature between these two points is optimal for this simplified study. Ultimately, the relationship between the value of electricity generation and ambient temperature will drive the compressor design temperature, and it is likely that paradigm will result in warmer compressor inlet temperatures than the ambient or DNI-weighted approaches.

Future work includes a wider parameter investigation during off-design operation to determine benefits and drawbacks, such as inlet compressor pressure (also known as inventory control), cooling air mass flow rate, and turbomachinery rotational speeds. Furthermore, this analysis will be extended to analyze constraining the cycle to achieve a constant HTF cold temperature and the associated tradeoffs.

CONCLUSION

This study investigates the performance of a recompression sCO2 Brayton cycle integrated with thermal storage in a CSP context, for both design-point and off-design conditions. Results of the design analysis showed that the inclusion of a HTF and primary heat exchanger model agree with previous studies suggesting that CSP plants must place careful consideration of the coupled system design parameter space, such as heat exchanger conductance, temperature differential across the heat exchanger, work output, and cycle efficiency. The performance analysis revealed the relative magnitude of the influence for two parameters both varying simultaneously off-design on cycle efficiency, HTF cold temperature, among other parameters. The current study highlights that off-design performance not only has immediate impacts on cycle efficiency, but also influences HTF cold temperature, which has indirect and important implications on thermal storage and receiver

173

performance. Finally, approximate annual efficiency calculations suggest that expected weather conditions during cycle operation should be considered when designing the system.

BIBLIOGRAPHY
[1] Neises, T., and Turchi, C., 2014, "A comparison of supercritical carbon dioxide power cycle configurations with an emphasis on CSP applications," Energy Procedia, 49, pp. 1187-1196.
[2] Turchi, C. S., Ma, Z., Neises, T. W., and Wagner, M. J., 2013, "Thermodynamic study of advanced supercritical carbon dioxide power cycles for concentrating solar power systems," Journal of Solar Energy Engineering, 135(4), p. 041007.
[3] Chapman, D. J., and Arias, D. A., "An Assessment of the Supercritical Carbon Dioxide Cycle for Use in a Solar Parabolic Trough Power Plant," Proc. Proceedings of SCCO2 Power Cycle Symposium, RPI, Troy, NY, April, pp. 29-30.
[4] Ma, Z., and Turchi, C., "Advanced supercritical carbon dioxide power cycle configurations for use in concentrating solar power systems," Proc. Proceedings of Supercritical CO2 Power Cycle Symposium, pp. 24-25.
[5] Dyreby, J. J., 2014, "Modeling the Supercritical Carbon Dioxide Brayton Cycle with Recompression," THE UNIVERSITY OF WISCONSIN-MADISON.
[6] Patnode, A. M., 2006, "Simulation and performance evaluation of parabolic trough solar power plants," University of Wisconsin.

Appendix D: Optimal Operation

Proceedings of the 9th International Conference on Energy Sustainability

ES2015

June 28 – July 2, San Diego, California, USA

PowerEnergy2015-49053

OPTIMAL OPERATION STRATEGIES FOR THERMAL ENERGY STORAGE SYSTEMS IN SOLAR THERMAL POWER PLANTS

Louis A. Tse
Department of Mechanical and Aerospace Engineering
University of California, Los Angeles
Los Angeles, CA, USA

Richard E. Wirz
Department of Mechanical and Aerospace Engineering
University of California, Los Angeles
Los Angeles, CA, USA

Adrienne S. Lavine
Department of Mechanical and Aerospace Engineering
University of California, Los Angeles
Los Angeles, CA, USA

175

ABSTRACT

This paper examines the economic benefits of various operation strategies for a thermal energy storage (TES) system in a solar thermal power plant. A thermodynamic model developed to evaluate different design options has been utilized to calculate system performance and assess the impact of operation strategies, storage capacity, and market prices on the value of TES. The overall performance is also investigated through several parametric studies, such as solar multiple, geographic location, and choice of HTF. The influence of these parameters has been evaluated in consideration of exergy destruction due to heat transfer and pressure drop. By incorporating exergy-based optimization alongside traditional energy analyses, the results of this study evaluate the optimal values for key parameters in the design and operation of TES systems, as well as highlight opportunities to minimize thermodynamic losses. Annual performance for each case is characterized both by nominal and part-load efficiency. Levelized cost of electricity (LCOE) is calculated for all cases, illustrating a set of optimal parameters that yield a minimum LCOE value.

NOMENCLATURE

A	cross-sectional area (m^2)
c	specific heat of fluid (Jkg^{-1}K^{-1})
E	energy (J)
Ex	exergy (J)
f	friction factor
h	heat transfer coefficient (Wm^{-2}K^{-1})
k	thermal conductivity (Wm^{-1}K^{-1})
m	storage fluid mass (kg)
$\dot{m}$	HTF mass flow rate (kgs^{-1})
P	pressure (kPa)
P_h	heat transfer perimeter (m)
q	heat rate (W)
T	cross-sectional average temperature (ºC)
u	internal energy per unit mass (Jkg^{-1})
V	HTF velocity (m/s)

176

χ	correction factor
η	pump efficiency
ρ	fluid average density (kg m^{-3})
τ	charging/discharging time
ψ	exergetic efficiency
AS	ancillary services
CAISO	California Independent System Operator
CSP	concentrating solar power
HTF	heat transfer fluid
LCOE	levelized cost of electricity
SM	solar multiple
STPP	solar thermal power plant
TES	thermal energy storage

SUBSCRIPTS

b	bypass
c	charging period
d	discharging period
gen	generator
i	inner
in	inlet
max	maximum
o	outer
out	outlet
sol	solar field
$stor$	storage
$tank$	tank (refers to HTF flow through tank)
tot	total
$wall$	wall (refers to wall of tube containing storage fluid)

INTRODUCTION

Concentrating solar power (CSP) with thermal energy storage is a promising technology to reduce levelized cost of electricity and its global implementation is projected to grow substantially in the

177

near future. CSP coupled with TES significantly increases capacity factor, and the storage capability allows for shifting energy to the periods of peak demand.

Two-tank storage systems employing molten salt has been demonstrated in large-scale CSP plants, in both parabolic trough and power tower configurations. However, the overall cost of molten salt storage systems remains high at approximately 30-50 $USD/kWh, with the molten salt inventory and the tanks accounting for 50% and 25% of the costs, respectively. The Department of Energy's SunShot Initiative has championed an aggressive effort to bring CSP closer to cost parity with traditional energy generation systems [152]. Cost-effective TES is an important component in attaining the cost reduction goals.

Several studies of CSP systems have assumed dispatch is fixed and have not include the comprehensive benefits of flexible dispatchability with TES. Many studies have investigated the value of CSP systems with molten salt TES by modeling the provision of ancillary services [145, 168], dispatch flexibility with arbitrage pricing [169], and production cost of variable generation [170]. This has resulted in a progression towards more complete evaluations of net system costs by clarifying substantial elements of value and establishing long-term economic and reliability benefits. Sioshansi and Denholm [168, 169], Denholm [170], Jorgenson [134], and Mills and Wiser [171, 172] have analyzed flexible dispatch of TES in CSP plants and have demonstrated the added market value of spinning and non-spinning reserves with exogenous fixed market prices. Cole [173], Camacho [174], and Powell [175] have modeled advanced control of TES systems in solar thermal power plants and have illustrated that the incorporation of TES with intermittent renewable energy sources and time-of-use electricity pricing decreases system costs by reducing required equipment size and maximizing plant operating revenue. Rolfsman [176] studied the optimal operation of TES in district heating applications and showed that proper operation of the TES prevents the most expensive equipment from operating in order to meet peak demand. In particular, TES permits system flexibility to plant operators and enables additional ancillary and market services such as short-term energy balancing, addressing system contingencies, synthetic inertial response, and peak shaving. Specifically, these include:

- Primary control reserves: frequency response
- Secondary control reserves: regulation, spinning reserve, and non-spinning reserve
- Tertiary control reserves: supplemental reserves

178

Energy dispatched into the real-time market allows plant production to be optimized to maximize plant revenue. The deviation from production scheduling is called load-following. In this analysis, because of the timescale (regulation is dispatched on the order of seconds), only revenues from spinning and non-spinning reserves are considered.

To further advance valuation of CSP with TES technologies, this investigation aims to evaluate the benefit of multi-phase TES in flexible dispatch with variable generation, and examines performance metrics such as avoided fuel and total plant revenue. The particular solar thermal power plant configuration that is considered is a parabolic trough plant with a multi-phase TES system that is described in [147, 177, 178]. Because the TES system plays an integral role in system operation, this paper investigates the performance of a multi-phase TES system. The nominal nameplate capacity of the power block is set to 50 MWe Rankine cycle, because it is a usual size for current parabolic trough plants. The solar field is modeled with a solar multiple of 1.4 and 6 hours of storage, both of which are derived by design operating conditions at a nameplate capacity of the power block, on a particular reference day.

Capital cost of the total CSP plant is an important marker on the economic feasibility of the system. This study aims to investigate the operating revenue of the CSP plant given the capability to respond quickly to demand on-grid during peak hours. This study assesses the responsiveness of the multi-phase TES system to ramp rate requirements and utility demand profiles typical in the CAISO territory. In order to analyze the cost and responsiveness of the plant to the various start-up costs (both time and energy), ramp rate requirements, and transient behavior of the CSP and TES systems must be modeled and matched to utility demand profiles. Therefore, in this study, the important factors of increasing dispatchability are presented, and effective operation strategies to maximize plant revenue are discussed.

CSP PLANT DESIGN

There have been a variety of designs for CSP plants that have been under study, such as SEGS I-IX, Andasol, Solar One and Two, among others, in terms of the relative sizing of each primary component – the solar field, TES, and power block, as shown in Figure 1. The balance of each of

179

these subsystems will govern the capacity factor, operational decisions, and ultimately levelized cost of electricity of the plant.
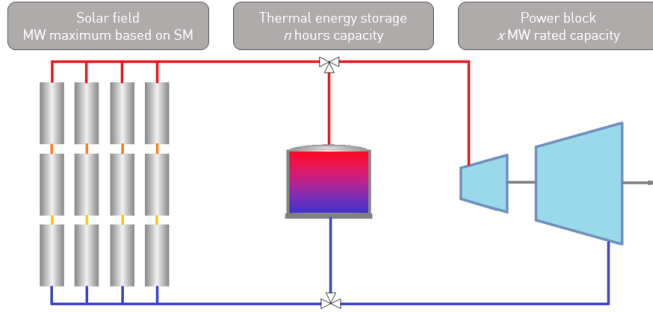
Figure 1: Primary system components in the CSP plant.

Solar field configuration

The conventional layout for oil-based parabolic trough solar fields is utilized [161, 179]. For the charging period, the inlet condition for the TES tank is governed by solar irradiation. The required solar field size is informed by a user-specified storage capacity (Table 2), which is held constant for all cases. The aperture area for one loop is calculated by dividing the total area by the number of loops. Because the maximum operating temperature of Therminol VP-1 is 400°C, the mass flow rate is varied to achieve a constant inlet HTF temperature of 390°C, and the minimum and maximum mass flow rate through a single loop is set to 1 kg/s and 12 kg/s, respectively. For a required energy output during the discharging period, the energy input during the charging period must be equal, therefore the solar field area can be expressed as

$$A_{sol} = \frac{E_{out}}{\int_0^{t_{charge}} \dot{Q}_{sol}} \qquad (7)$$

where $\dot{Q}_{sol}$ is the solar irradiance as a function of time during the charging period. For the discharging period, the steam generator specifications provide the inlet condition to the TES tank (Table 2). The storage tubes and tank are assumed to be the same length, and the boundaries at the tank inlet and outlet are assumed adiabatic.

Assuming no losses in the piping, the equality of the HTF temperature between the tank and solar field during the charging period is

180

$$T_{tank,in} = T_{sol,out} \qquad (8)$$

$$T_{tank,out} = T_{sol,in} \qquad (9)$$

with similar expressions between the tank and steam generator during the discharging period.

Table 1: Parameters for the solar field in the baseline system under study.

Solar field parameters	
Solar field optical efficiency	74.2%
Solar field cleanliness factor	97%
Solar field size	337,6100 m^2
Type of collector	Eurotrough-II
Number of loops	120
Design HTF outlet temperature	390°C

Hourly direct normal irradiation and psychometric data have been obtained from the National Solar Radiation Database (NSRDB) for Daggett, CA [81]. In order to account for transient behavior of the parabolic trough collector system, a common operation strategy is to maintain the charging loop mass flow rate nearly constant while adapting the solar field outlet temperature [91]. In this paper, a different strategy is chosen, and the solar field outlet temperature is held constant and the charging loop mass flow rate is variable, up to a maximum value. Additionally, the plant location governs the market pricing, demand profiles, and operating conditions and constraints. For consistency, the analysis utilizes CAISO data within the model which a CSP plant in Daggett would be subject to.

TES system

The thermal energy storage unit is envisioned as a single-tank design (Figure 2), in which the storage fluid is enclosed in tube bundles with sufficient wall thickness to withstand the highest system pressure. The tube bundles are contained in a low-pressure tank shell, through which the heat transfer fluid (HTF) flows, creating an internal heat exchanger within the storage tank. The schematic shows the operation during the discharge cycle, when the HTF flows between storage and the steam generator. During charging, the HTF is directed to flow between storage and the solar field.

181
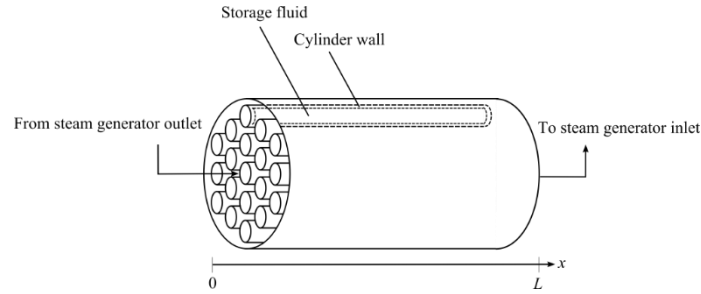
Figure 2: Single-tank system configuration with tube bundles (not drawn to scale).

The TES tank interacts with the charging and discharging loops, as shown in Figure 2. In the charging loop, energy from the solar field is transferred to the tube bank containing the storage fluid via heat transfer from the HTF. The discharging loop reverses this process and removes energy from the tube bundles to the HTF, to produce steam for power generation. In this study, we analyze the charging and discharging periods individually with respective control volume inputs and outputs, as indicated in Figure 2.

Since the storage fluid temperature is high at the beginning of the discharge cycle, the HTF temperature will also be higher than the optimal value required by the steam generator; this value is taken as 390°C based on a performance study of a two-tank TES system performed by Kolb [3]. To reduce the HTF temperature to its design value, the HTF exiting the thermal storage unit is mixed with the HTF exiting the steam generator through a bypass loop.

The thermal storage tubes are loaded with a certain fixed mass of the storage fluid. Since their volume remains constant, the average density, or *loading*, ρ also remains constant. Thus the discharge cycle follows a constant density (i.e. constant specific volume) line on a *P-v* diagram, as shown in Figure 3.

182
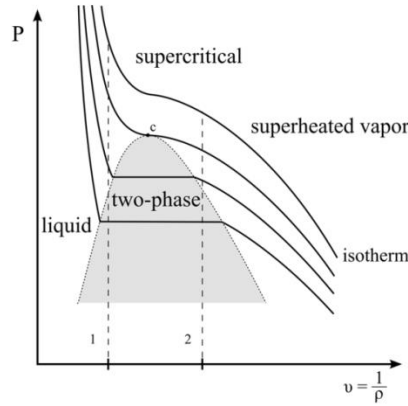
Figure 3: *P-v* diagram showing vertical lines of constant average fluid density.

The charging period begins at an initial two-phase state corresponding to low temperature, pressure, and internal energy, and ends at a final state corresponding to high temperature, pressure, and internal energy. Conversely, the discharging period reverses this process as energy is extracted from the TES system. At any instant in time, the internal energy and density can be related to the storage fluid temperature and pressure:

$$u = u(T_{stor}, P), \quad \rho = \rho(T_{stor}, P) \qquad (1, 2)$$

Thus with fixed density, if the storage fluid temperature is known, its pressure can be determined from Eq. (2) and its internal energy can then be determined from Eq. (1). These relationships are implemented using the Peng-Robinson equation of state and enthalpy departure function, which have been shown to provide reasonable predictive capabilities for a wide range of fluids [36]. Additional needed inputs for Eq. (1) are the fluid critical temperature and pressure, acentric factor, and the ideal gas specific heat and saturation pressure as functions of temperature. In this paper, naphthalene is modeled as an example of storage fluid, but any fluid can be investigated if its thermodynamic properties, namely density and internal energy, are known as a function of temperature and pressure [147].

Table 2: System specifications of the example TES system.

Storage fluid properties	
Critical temperature, T_c	478ºC
Critical pressure, P_c	4070 kPa

183

Acentric factor, ω	0.309
Molecular weight	128.17 kg/kmol
Effective specific heat of storage fluid, c_{stor} (from Peng-Robinson)	2.18 – 2.98 kJkg^{-1}K^{-1}
Thermal conductivity of storage fluid, k_{stor}	0.122 Wm^{-1}K^{-1}
Other fixed system parameters	
Specific heat of tube wall material, c_{wall}	0.5 kJkg^{-1}K^{-1}
Thermal conductivity of tube wall material, k_{wall}	16.3 Wm^{-1}K^{-1}
Density of tube wall material, ρ_{wall}	7990 kg/m^3
Ultimate tensile strength, F_{tu}	291 MPa
Specific heat of HTF, c_{HTF}	2.446 kJkg^{-1}K^{-1}
Thermal conductivity of HTF, k_{HTF}	0.098 Wm^{-1}K^{-1}
Density of HTF, ρ_{HTF}	1060 kg/m^3
Inner tube radius, r_i	0.025 m
Tube pitch	0.056 m
Tube length, L	12 m
Inner Nusselt number, $(hD)_i / k_{stor}$	6.92
Outer Nusselt number, $(hD)_o / k_{HTF}$	271
Dead-state temperature, T_0	25ºC
Storage capacity	6 h

Energy analysis

The TES system and discharging loop are modeled with a set of energy and mass balances, as given below.

Energy balance for the storage fluid:

$$(\rho c A)_{stor} \frac{\partial T_{stor}}{\partial t} = -(hP_h)_i (T_{stor} - T_{wall}) + (kA)_{stor} \frac{\partial^2 T_{stor}}{\partial x^2}$$

(3)

Energy balance for the tube wall material:

$$(\rho c A)_{wall} \frac{\partial T_{wall}}{\partial t} = (hP_h)_i (T_{stor} - T_{wall})$$
$$-(hP_h)_o (T_{wall} - T_{HTF}) + (kA)_{wall} \frac{\partial^2 T_{wall}}{\partial x^2}$$

184

$$(4)$$

Energy balance for the HTF flowing through the storage tank:

$$\left(\rho c A\right)_{HTF}\frac{\partial T_{HTF}}{\partial t}+\dot{m}_{tank}c_{HTF}\frac{\partial T_{HTF}}{\partial x}=\left(hP_h\right)_o\left(T_{wall}-T_{HTF}\right)$$
$$+\left(kA\right)_{HTF}\frac{\partial^2 T_{HTF}}{\partial x^2}$$

$$(5)$$

The values of hi and ho are informed from FLUENT simulations of HTF flowing parallel to a single tube of radius 0.025 m, through an outer cylindrical control volume of radius 0.026 m, utilizing the same values for mass flow rate (Table 1) and fluid properties (Table 2). The equations also assume that the bulk mean and cross-sectional average temperatures are identical for the HTF; this assumption has been shown to be quite accurate from the FLUENT simulation. In addition, the temperature difference across the tube wall is neglected due to the tube wall thermal resistance being small compared with the overall thermal resistance. With regards to initial temperature conditions, the storage tank is initially assumed to be fully discharged. Then, cyclic operation is performed until the temperatures within the tank achieve stability.

The value of c_{stor}, the effective specific heat of the storage fluid, is defined as

$$c_{stor}=\frac{\Delta u}{\Delta T}\qquad(6)$$

where Δu is the change in internal energy corresponding to an incremental change in temperature, ΔT, which is operationally taken across one time step. The effective specific heat is calculated at each spatial and time step, and is termed "effective" because it includes latent heat effects. The inlet condition for the HTF is different for the charging and discharging loops.

Once the discharge model is solved for a specified period of time (12 h), the quantity of thermal energy removed from storage, E_{tot}, can be calculated:

$$E_{tot}=\left(m\Delta\bar{u}\right)_{stor}+\left(mc\Delta\bar{T}\right)_{wall}+\left(mc\Delta\bar{T}\right)_{HTF}\quad(10)$$

185

where the overbar represents the volumetric average and Δ denotes the difference between the initial and final states. Note that E_{tot} also represents the quantity of solar energy that had to be diverted to storage during the charging period. Then, for the discharging period, the power block specifications of an Andasol-type plant are modeled [180], as given in Table 2. Specifically, the value of E_{tot} needed to generate the desired turbine power of 50 MW$_e$ for 12 hours at the turbine efficiency of 37% is $E_{tot} = 50 \text{ MW} \times 12 \text{ h}/0.37 = 1621 \text{ MWh}_t$. The storage fluid mass is iterated upon to achieve the desired storage capacity.

Pressure loss

Pressure losses in both energy and exergy analyses of TES systems cannot be evaluated accurately if design geometry is not known or is not within the scope of work. Pump work is often neglected in part because of this, but in many cases, it has been shown to be a significant energy cost and is an important consideration [114, 115]. Additionally, it has been demonstrated that the pressure loss has a greater effect in exergy analysis [112, 114].

Naturally, each TES system will account for pressure losses differently based on respective tank geometry, flow regime, etc. For PCM systems utilizing shell-and-tube exchangers, several studies have adopted Kern's Method [116], or the Bell-Delaware Method [117]. Moreover, varying assumptions can be made in respective analyses to simplify the model for versatility. For a sensible storage system utilizing a heat exchanger, Krane approximated pressure drop using flow past a tube [115]. For this analysis, a typical design geometry of the TES tank is given and the pressure loss is modeled as crossflow over a large tube bank. The pressure drop for a tube bank with a staggered configuration is given in [181]:

$$\Delta p = N_L \chi \left(\frac{\rho_{HTF} V_{max}^2}{2} \right) f \qquad (10)$$

where N_L is the number of tube rows, V_{max} is the maximum velocity of the HTF, χ is the correction factor, and f is the friction factor; the latter two are given in charts as a function of Reynolds number and tube configuration, and provided by Bergman et al.. The exergy destruction due to a pressure drop Δp is written as

186

$$\dot{W}_{pump} = \frac{\dot{m}_{HTF} \Delta p}{\rho_{HTF} \eta} \qquad (11)$$

where this is both an energy and exergy cost. This is because exergy is defined as "useful work" [115, 120]; in governing principles, work done to the system is equivalent in both the first and second law analyses [112, 114, 121].

Exergy analysis

The exergy supplied to the TES tank during the charging period, assuming an incompressible fluid, can be expressed as

$$Ex_{charge} = \int_{0}^{t_{charge}} (\dot{m}c)_{HTF} \left[\left(T_{HTF,in} - T_{HTF,out} \right) - T_0 \ln \left(\frac{T_{HTF,in}}{T_{HTF,out}} \right) \right] dt$$

$$(12)$$

And the exergy recovered from the TES tank during the discharging period is similarly denoted as

$$Ex_{discharge} = \int_{t_{charge}}^{t_{discharge}} (\dot{m}c)_{HTF} \left[\left(T_{HTF,out} - T_{HTF,in} \right) - T_0 \ln \left(\frac{T_{HTF,out}}{T_{HTF,in}} \right) \right] dt$$

$$(13)$$

It should be noted that by defining the control volume across the TES tank, any exergy destruction that occurs between the storage fluid and HTF in the tank is still accounted for, as it will ultimately manifest itself in the outlet HTF temperature.

Exergetic efficiency can be expressed in a multitude of ways, depending on the analysis [111]. In this work, the analysis of a full working cycle allows exergetic efficiency to be expressed as

$$\psi = \frac{\int_{t_{charge}}^{t_{discharge}} (\dot{m}c)_{HTF} \left[T_{HTF,out}(t) - T_{gen,out} - T_0 \ln \left(\frac{T_{HTF,out}(t)}{T_{gen,out}} \right) \right] \Delta t}{\int_{0}^{t_{charge}} (\dot{m}c)_{HTF} \left[T_{sol,out} - T_{HTF,in}(t) - T_0 \ln \left(\frac{T_{sol,out}}{T_{HTF,in}(t)} \right) \right] \Delta t} - E_{pump} \qquad (14)$$

Power block performance

The power block considered is a 50 MWe steam Rankine cycle. The HTF used in the system governs the operating temperature of the power block. As stated before, the thermal stability of Therminol VP-1 allows for a nominal temperature of 390°C. However, when not enough thermal

187

power is available from the solar field or TES, the power block will perform at part-load conditions. Nominal and part-load efficiency of each case considered has been derived from previous assessment of parabolic trough models [91, 182].

Design- and part-load conditions

Detailed power block components can model the thermodynamic performance depending on the thermal parameters of the pre-heater, evaporator, superheater, number of extraction points, regenerative feeders, among other components [90, 137, 183]. For this model, transfer functions based on empirical data from an Andasol-type plant described by Kolb [182] are utilized to characterize design- and part-load efficiency of the turbine. These curves are dependent on inlet HTF temperature and mass flow rate, and the outputs are outlet HTF temperature and gross power output.

Table 3: Operational parameters for the power block.

Parameter	Baseline value
Ramp rate	10%/min
Start-up energy	20%
Number of starts per day	Unconstrained
Minimum up time	1 h
Minimum down time	1 h
Outage rate	4%
Minimum/maximum generation	25%/110%
Mass flow rate	547 kgs^{-1}
HTF inlet temperature	390ºC
HTF outlet temperature	289ºC
Power output	50 MW_e

The system model was implemented in MATLAB using the Peng-Robinson equation of state and enthalpy departure function calculated for naphthalene using data of Barrow and McClellan [164], and the saturation pressure was modeled using the Pitzer correlation [37]. The governing equations were discretized explicitly in space and time. The time interval for the calculations was on an hourly basis, which is the typical timeframe for forecasting and is discussed in the subsequent sections.

188

OPERATIONAL STRATEGIES

Operational attributes

As described in the previous section, solar thermal power plants with TES can be designed with a variety of different parameters, each of which have an impact on overall cost-benefit analysis. Still, in the context of adding value to market or utility benefit, operational attributes, such as ramp rate, minimum and maximum generation levels, and start-up costs, play an equally important role. These parameters, combined with real-time market conditions, must be modeled to determine optimal operation of the TES system and maximize energy revenues. The operational parameters considered are detailed in Table 3.

Ancillary services (AS) and valuation

Ancillary services (AS) and other flexible dispatch requirements for energy systems are projected to increase as wind, solar, micro-grids, and grid storage increase in penetration. The California Energy Commission (CEC) has ceased construction of coal-fueled power generation in CA as well as the import of power produced by coal-fueled plants. As a result, the wholesale energy market has a stronger reliance on natural gas and renewable energy. According to Stoddard et al., the use of natural gas for immediate delivery, the "spot market", and options on future delivery has illustrated a high price volatility in recent years. Specifically, natural gas prices have shown an upward trend - the annual average natural gas price has increased 247% from 1995-2005 [184]. Then, the deployment of CSP can lower exposure to natural gas price fluctuations and provide cost savings, particularly in the provision of ancillary services. Ancillary services (AS) can be described in three categories:

- Primary: Frequency response
- Secondary: Regulation, spinning reserve, non-spinning reserve
- Tertiary: Supplemental reserve

Assumptions

A major assumption in this analysis is that the CSP plant operator will have perfect foresight of energy prices and available solar energy forecasts in determining the optimal operation strategy.

189

In reality, plant operators can have a wide variety of forecasting tools which directly impact the quality of the forecast. The purpose of this study is not to evaluate the effectiveness of forecasting techniques. Other studies have compared the "backcasting" technique, or the dispatch according to historical data. The results determined that it depends largely on the solar multiple and storage capacity, and approximately 90% of the operating revenues of a perfect foresight system can be realized [168].

Additionally, we assume the CSP plant will not provide frequency response, regulation up/down, or non-spinning reserves due to the timescale of dispatching these services, which would be unfeasible for the TES and power block being considered. We study two cases for the spinning reserves, in which either 25% or 50% of the power block capacity can be delivered [157]. Moreover, this analysis assumes that the CSP plant operates as a price-taker with real-time energy prices that do not respond to the energy sales of the CSP plant. Restated, every participant in the wholesale energy market affects the current price of energy. However, this assumption is sound because the analysis is for a single CSP plant, which would have a minimal effect relative to the entire CAISO market [145].

Optimization model

In this analysis, the sole constraint will be energy output – each TES case must discharge 1621 MWh$_t$ in order to fairly compare each case. Using energy output as an objective constraint is a rational approach for comparing TES systems with varying parameters in order to determine optimal operating values, such that exergy destruction is minimized, while maintaining the same output.

Solar resources without storage are generally scheduled on a day-ahead and hour-ahead basis using production forecasts in those time-frames, and do not currently submit bids to alter their production. A further differentiating characteristic is whether resources are able to follow economic dispatch instructions, whether from a utility or through a bid-based wholesale auction market. The scheduling procedures to establish a "least-cost" unit commitment economic dispatch are typically conducted on day-ahead and real-time time-frames. In these time-frames, energy is either (a) scheduled inflexibly (self-scheduled) by the plant operator or utility owner, based on a known production schedule or a forecast, or (b) offered as dispatchable, which allows the plant's production to be optimized to minimize system costs. In the day-ahead markets, accepted energy

190

schedules or offers obtain an hourly schedule for the next operating day and are financially settled at day-ahead prices. In the real-time markets, the supplier may either operate according to the day-ahead schedule or buy-back some or all of the day-ahead position. Dispatchable energy offered into the real-time market generally has more explicit performance requirements and can be optimized on a five-minute basis by the market or system operator. The deviations from prior schedules being followed in real-time is sometimes called load-following, or "net" load following, when it also reflects deviations from variable energy resources. The present study aims to determine an optimal operation strategy that maximizes operating revenue. The formulation of the optimization problem is subject to

$$
\begin{aligned}
&0 \le t_{charge} \le t_{charge,crit} \\
&0 \le t_{discharge} \le t_{discharge,crit} \\
&E_{out} = \eta \cdot W_{turb} \cdot t_{discharge} \\
&\psi - \psi_{crit} \ge 0
\end{aligned}
\tag{15}
$$

The optimization problem utilizes a Nelder-Mead simplex search method that, given positive convexity, ensures an increase in the objective function. The simplex is defined by k-dimensional space with $k+1$ vertices, where k is the number of design parameters under study.

NUMERICAL RESULTS AND DISCUSSION

The temperature profile of the tank during the charging period is shown in Figure 4, where τ is the fractional charging or discharging time. The maximum temperature achieved for the baseline case is 400°C. The spatial gradient within the tank shows the TES tank remains colder at the outlet. The degree of spatial temperature variation will vary based on the mass flow rate: higher mass flow rates will lead to a more uniform temperature distribution.

191
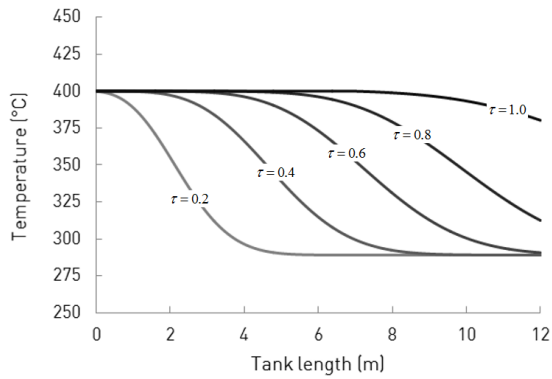
(a)
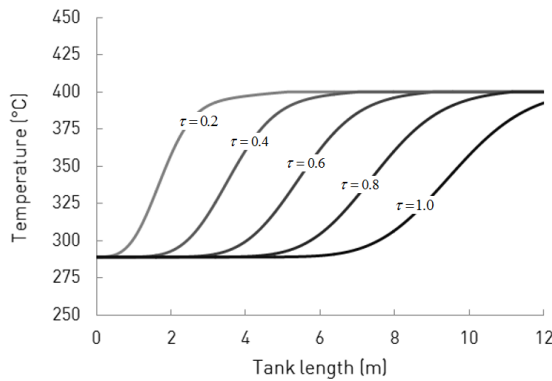
(b)

Figure 4: Temperature profile within the tank during a) charging and b) discharging.

The analysis considers the operation of a CSP plant in Daggett, CA using real-time energy price data from the CAISO market, and aims to capture operational strategies across different diurnal and seasonal load patterns. Figure 5 shows the dispatch of the CSP plant on a typical winter and summer day to capture seasonal differences in operation strategies.

192
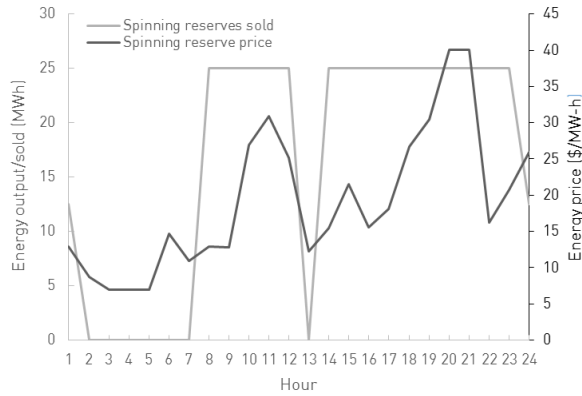
(a)
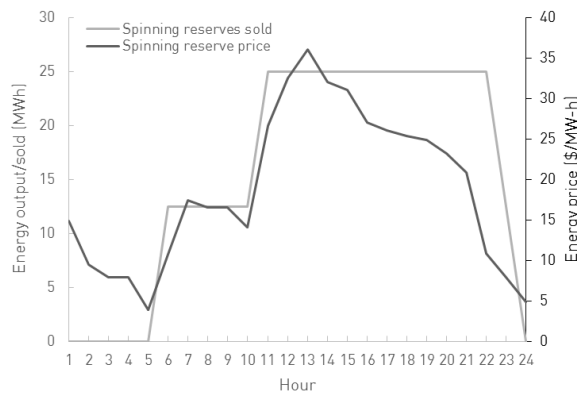
(b)

Figure 5: Simulated dispatch profile for the CSP plant during a typical day in a) winter and b) summer.

The key characteristics of each season are illustrated in Figure 5. Diurnal load patterns for each season is different, which affects operational decisions. The summer price profile reaches peak demand during midday and afternoon for cooling, while the winter price profile features a peak at the beginning and end of the day for heating. As a result, summer operation is generally more coincident, which is compounded by more daylight hours. Then, dispatch is generated from TES for these periods to be able to gather operating revenue from high energy prices. From hours 15-17, there is not enough energy in the TES so spinning reserves are not sold –and the energy from the solar field is stored in TES – in order to catch the higher prices in the evening.

Optimal operation strategy

193

In addition to optimizing plant design, the operation and control of the TES system improves plant performance and maximizes the value and flexibility that TES provides. The latter has played an increasingly important role as intermittent renewable energy sources become a higher percentage of the energy portfolio and deferred costs of plants are compounded with demand response and time-of-use electricity pricing. Some studies have studied advanced multivariate controls [185], model predictive control [186], and flexible operation for CSP plant operators [187]. Optimization can also vary based on the objective function; these can be defined based on LCOE [3, 169, 170], ROI [188], NPV [189], among others.

In terms of operating revenue, the optimal discharge strategy is extract the thermocline region for start-up energy cost of the power block, then subsequently feeding the power block for design-point generation. Then, the combination of wholesale energy prices, spinning reserve prices, and power block up/down costs will govern the optimal lengths of time to provide AS, which is typically zero to three times a day, which is easy to implement in a parabolic trough STPP.

Effect of solar multiple

As previously mentioned, the relative sizing of the system components, such as the solar field, TES, and power block, governs the overall system operation and performance. Solar multiple is defined as the ratio of the thermal power generated from the solar field and the thermal power needed by the power block at design-point operation. The solar field is nominally sized with reference to a particular day, which translates to a solar multiple (SM) of 1. For example, SM between 1.0 – 1.2 will generally not meet capacity needs of the power block year-round. As SM increases, the thermal power output coming from the solar field can exceed the allowable limit for the power block causing "spillage", or excess energy that cannot be harnessed. The inclusion of a TES system allows for larger SM to collect energy for later use, thereby increasing capacity factor and flexibility for dispatch.

Different CSP system configurations have been studied to find the optimal overall sizing of each component, and some key aspects are briefly listed in Table 14; however, other important system specifications that influence optimal values can be found at the source.

194

Table 4: Various studies of the effect of varying solar multiple on CSP plant operation.

Solar field	TES	Power block	Local optimal value(s)	Ref.
Trough	Two-tank molten salt	110 MW$_e$ steam Rankine	SM = 1.5 – 1.7 TES = 2-4 h	[145]
Trough	Thermocline molten salt	111.5 MW$_e$ steam Rankine	SM = 3 TES = 16 h	[146]
Trough	None	50 MW$_e$ steam Rankine	SM = 1.15	[145]
Tower	Two-tank molten salt	110 MW$_e$ steam Rankine	SM = 2.5 TES = 12 h	[134]

The optimization of SM configuration for the parabolic trough plant with multi-phase TES is presented in Figure 6.
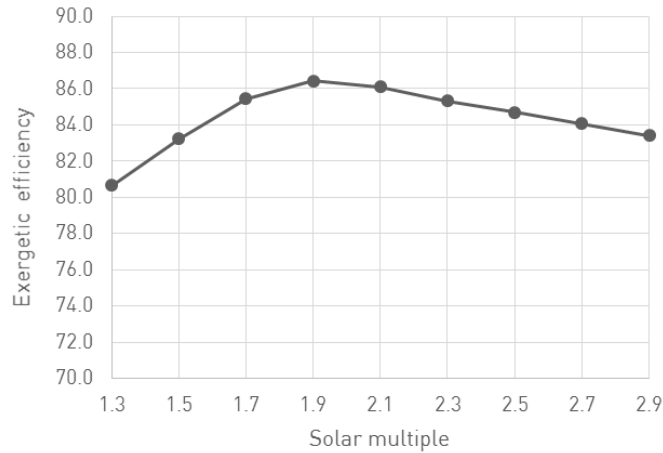
Figure 6: Exergetic efficiency as a function of solar multiple, for a fixed TES system with 6 h of storage.

As Figure 6 shows, the optimal value of SM achieves the balance of collecting and providing sufficient thermal energy to the rest of the CSP components while minimizing "spillage" of wasted energy that cannot be collected. For increased storage capacity, the optimal SM increases to take advantage of the capability to collect energy for later use [134].

CONCLUSION

CSP plants with TES provide numerous benefits to the grid, including provision of ancillary services, peak shifting and shaving capability, and reducing integration costs. This study evaluated the optimal operation strategy for a CSP plant with a multi-phase TES system. It is important to note that this analysis does not account for all the potential benefits of TES, such as decreasing integration costs, ability to serve sub-hourly dispatch, and deferred plant costs. Also, the overall economic value of the CSP plant with TES will increase if capacity value is taken into account, which has been evaluated in a couple studies by using the capital cost of a similarly sized gas combustion turbine [168, 190]. It is also clear that the valuation of CSP plants with TES will differ outside the CAISO territory [168], as well as outside the United States. This analysis does not include the sensitivity of AS costs to other ISO territories, generator constraints, and fuel prices, which must be investigated to fundamentally understand the underlying cost sensitivities. Because operational flexibility is not yet well established and economic conclusions are still emerging, a range allows an in-depth study of the various parameters that influence cost. As the energy portfolio connected to the grid becomes more diverse and the market needs evolve, the optimal operation is likely to change. Especially as other renewable energy technology capacity increases, such as PV and wind, the operation of the TES may shift to cover different portions of the diurnal load pattern. The innate flexibility of TES gives CSP more firm generation, though this warrants a more in-depth investigation for higher renewable penetration and careful forecast of fuel prices.

ACKNOWLEDGEMENTS

BIBLIOGRAPHY

[1] SunShot, U. S. D. o. E., 2012, "SunShot Vision Study," Presentation.
[2] Madaeni, S. H., Sioshansi, R., and Denholm, P., 2012, "How thermal energy storage enhances the economic viability of concentrating solar power," Proceedings of the IEEE, 100(2), pp. 335-347.
[3] Sioshansi, R., and Denholm, P., 2010, "The value of concentrating solar power and thermal energy storage," Sustainable Energy, IEEE Transactions on, 1(3), pp. 173-183.

196

[4] Sioshansi, R., Denholm, P., Jenkin, T., and Weiss, J., 2009, "Estimating the value of electricity storage in PJM: Arbitrage and some welfare effects," Energy economics, 31(2), pp. 269-277.

[5] Denholm, P., and Mehos, M., 2011, "Enabling greater penetration of solar power via the use of CSP with thermal energy storage," Contract, 303, pp. 275-3000.

[6] Jorgenson, J., Denholm, P., and Mehos, M., "Quantifying the Value of Concentrating Solar Power in a Production Cost Model," Proc. ASME 2014 8th International Conference on Energy Sustainability collocated with the ASME 2014 12th International Conference on Fuel Cell Science, Engineering and Technology, American Society of Mechanical Engineers, pp. V001T002A007-V001T002A007.

[7] Mills, A., 2013, "Changes in the economic value of variable generation at high penetration levels: A pilot case study of California."

[8] Mills, A. D., "An evaluation of solar valuation methods used in utility planning and procurement processes," Proc. American Solar Energy Society (ASES) Annual Meeting, Baltimore, MD, April 16-20, 2013.

[9] Cole, W. J., Powell, K. M., and Edgar, T. F., 2012, "Optimization and advanced control of thermal energy storage systems," Reviews in Chemical Engineering, 28(2-3).

[10] Camacho, E. F., Berenguel, M., Alvarado, I., Limon, D., and de los Descubrimientos, C., "Control of solar power systems: a survey," Proc. Proc. of the 9th Int. Symp. on Dynamics and Control of Process Systems, DYCOPS.

[11] Powell, K. M., and Edgar, T. F., 2012, "Modeling and control of a solar thermal power plant with thermal energy storage," Chemical Engineering Science, 71, pp. 138-145.

[12] Rolfsman, B., 2004, "Combined heat-and-power plants and district heating in a deregulated electricity market," Applied energy, 78(1), pp. 37-52.

[13] Tse, L. A., Lakeh, R. B., Wirz, R. E., and Lavine, A. S., "Exergy-Based Optimization of Sub- and Supercritical Thermal Energy Storage Systems," Proc. ASME 2014 8th International Conference on Energy Sustainability collocated with the ASME 2014 12th International Conference on Fuel Cell Science, Engineering and Technology, American Society of Mechanical Engineers, pp. V002T012A001-V002T012A001.

[14] Tse, L., Ganapathi, G., Wirz, R., and Lavine, A., "System Modeling for a Supercritical Thermal Energy Storage System," Proc. ASME 2012 6th International Conference on Energy Sustainability collocated with the ASME 2012 10th International Conference on Fuel Cell Science, Engineering and Technology, American Society of Mechanical Engineers, pp. 691-698.

[15] Tse, L. A., Ganapathi, G. B., Wirz, R. E., and Lavine, A. S., 2014, "Spatial and temporal modeling of sub- and supercritical thermal energy storage," Solar Energy, 103(0), pp. 402-410.

[16] Herrmann, U., Kelly, B., and Price, H., 2004, "Two-tank molten salt storage for parabolic trough solar power plants," Energy, 29(5-6), pp. 883-893.

[17] Turchi, C., 2010, "Parabolic trough reference plant for cost modeling with the solar advisor model (SAM)," National Renewable Energy Laboratory (NREL), Golden, CO.

[18] Wilcox, S., and Marion, W., 2008, Users manual for TMY3 data sets, National Renewable Energy Laboratory Golden, CO.

[19] Lippke, F., 1995, "Simulation of the part-load behavior of a 30 MWe SEGS plant," Sandia National Labs., Albuquerque, NM (United States).

[20] Peng, D.-Y., and Robinson, D. B., 1976, "A new two-constant equation of state," Industrial & Engineering Chemistry Fundamentals, 15(1), pp. 59-64.

[21] Kolb, G. J., 2011, "Evaluation of annual performance of 2-tank and thermocline thermal storage systems for trough plants," Journal of solar energy engineering, 133(3).

[22] Gunnewiek, L., Nguyen, S., and Rosen, M., 1993, "Evaluation of the optimum discharge period for closed thermal energy storages using energy and exergy analyses," Solar energy, 51(1), pp. 39-43.

[23] Krane, R. J., 1987, "A second law analysis of the optimum design and operation of thermal energy storage systems," International Journal of Heat and Mass Transfer, 30(1), pp. 43-57.

[24] Rosen, M. A., and Dincer, I., 2003, "Exergy methods for assessing and comparing thermal storage systems," International Journal of Energy Research, 27(4), pp. 415-430.

[25] Kern, D. Q., 1950, Process heat transfer, Tata McGraw-Hill Education.

[26] Bell, K. J., 1988, "Delaware method for shell-side design," Heat Transfer Equipment Design, Hemisphere Publishing, New York, p. 145.

[27] Bergman, T. L., Lavine, A. S., Incropera, F. P., and DeWitt, D. P., 2011, Fundamentals of Heat and Mass Transfer, John Wiley & Sons Incorporated.

[28] Bejan, A., 1978, "General criterion for rating heat-exchanger performance," International Journal of Heat and Mass Transfer, 21(5), pp. 655-658.

[29] Moran, M. J., Shapiro, H. N., Boettner, D. D., and Bailey, M., 2010, Fundamentals of engineering thermodynamics, Wiley. com.

[30] Rosen, M. A., 1992, "Appropriate thermodynamic performance measures for closed systems for thermal energy storage," ASME Journal of Solar Energy Engineering, 114, pp. 100-105.

[31] Kolb, G. J., 2011, "Evaluation of annual performance of 2-tank and thermocline thermal storage systems for trough plants," Journal of Solar Energy Engineering, 133(3), p. 031023.

[32] Montes, M., Abánades, A., Martinez-Val, J., and Valdés, M., 2009, "Solar multiple optimization for a solar-only thermal power plant, using oil as heat transfer fluid in the parabolic trough collectors," Solar Energy, 83(12), pp. 2165-2176.

[33] Patnode, A. M., 2006, "Simulation and performance evaluation of parabolic trough solar power plants," University of Wisconsin.

[34] Price, H., "A parabolic trough solar power plant simulation model," Proc. ASME 2003 International Solar Energy Conference, American Society of Mechanical Engineers, pp. 665-673.

[35] Barrow, G. M., and McClellan, A., 1951, "The thermodynamic properties of naphthalene," Journal of the American Chemical Society, 73(2), pp. 573-575.

[36] Pitzer, K., 1991, "Ion interaction approach: theory and data correlation," Activity coefficients in electrolyte solutions, 2, pp. 75-154.

[37] Stoddard, L., Abiecunas, J., and O'Connell, R., 2006, Economic, energy, and environmental benefits of concentrating solar power in California, National Renewable Energy Laboratory.

[38] Hummon, M., Denholm, P., Jorgenson, J., Palchak, D., Kirby, B., and Ma, O., 2013, "Fundamental Drivers of the Cost and Price of Operating Reserves," NREL, Golden, CO.

[39] Camacho, E., Rubio, F., Berenguel, M., and Valenzuela, L., 2007, "A survey on control schemes for distributed solar collector fields. Part II: Advanced control approaches," Solar Energy, 81(10), pp. 1252-1272.

[40] Rubio, F. R., Berenguel, M., and Camacho, E. F., 1995, "Fuzzy logic control of a solar power plant," Fuzzy Systems, IEEE Transactions on, 3(4), pp. 459-468.

[41] Menéndez, R. P., Martínez, J. Á., Prieto, M. J., Barcia, L. Á., and Sánchez, J. M. M., 2014, "A Novel Modeling of Molten-Salt Heat Storage Systems in Thermal Solar Power Plants," Energies, 7(10), pp. 6721-6740.

[42] Denholm, P., Jorgenson, J., Hummon, M., Jenkin, T., Palchak, D., Kirby, B., Ma, O., and O'Malley, M., 2013, "The value of energy storage for grid applications," Contract, 303, pp. 275-3000.

198

[43] Bruno, S., Lamonaca, S., La Scala, M., and Stecchi, U., "Optimal Design of Trigeneration and District Energy in the Presence of Energy Storage," Proc. International Conference on Renewable Energies and Power Quality (ICREPQ'10), Granada (Spain), 23th to 25th March.

[44] Piacentino, A., and Cardona, F., 2008, "An original multi-objective criterion for the design of small-scale polygeneration systems based on realistic operating conditions," Applied Thermal Engineering, 28(17), pp. 2391-2404.

[45] Flueckiger, S. M., Iverson, B. D., and Garimella, S. V., 2014, "Economic Optimization of a Concentrating Solar Power Plant With Molten-Salt Thermocline Storage," Journal of Solar Energy Engineering, 136(1), p. 011015.

[46] Madaeni, S. H., Sioshansi, R., and Denholm, P., 2013, "Estimating the capacity value of concentrating solar power plants with thermal energy storage: A case study of the southwestern United States," Power Systems, IEEE Transactions on, 28(2), pp. 1205-1215.

Bibliography

[1] Pardo, P., Deydier, A., Anxionnaz-Minvielle, Z., Rougé, S., Cabassud, M., and Cognet, P., 2014, "A review on high temperature thermochemical heat energy storage," Renewable and Sustainable Energy Reviews, 32, pp. 591-610.

[2] Cabeza, L. F., Martorell, I., Miró, L., Fernández, A. I., and Barreneche, C., 2015, "1 - Introduction to thermal energy storage (TES) systems," Advances in Thermal Energy Storage Systems, Woodhead Publishing, pp. 1-28.

[3] Denholm, P., Jorgenson, J., Hummon, M., Jenkin, T., Palchak, D., Kirby, B., Ma, O., and O'Malley, M., 2013, "The value of energy storage for grid applications," Contract, 303, pp. 275-3000.

[4] Dincer, I., and Rosen, M., 2002, Thermal energy storage: systems and applications, Wiley. com.

[5] Gil, A., Medrano, M., Martorell, I., Lázaro, A., Dolado, P., Zalba, B., and Cabeza, L. F., 2010, "State of the art on high temperature thermal energy storage for power generation. Part 1— Concepts, materials and modellization," Renewable and Sustainable Energy Reviews, 14(1), pp. 31-55.

[6] Hasnain, S., 1998, "Review on sustainable thermal energy storage technologies, part I: heat storage materials and techniques," Energy Conversion and Management, 39(11), pp. 1127-1138.

[7] Medrano, M., Gil, A., Martorell, I., Potau, X., and Cabeza, L. F., 2010, "State of the art on high-temperature thermal energy storage for power generation. Part 2—Case studies," Renewable and Sustainable Energy Reviews, 14(1), pp. 56-72.

[8] Pinel, P., Cruickshank, C. A., Beausoleil-Morrison, I., and Wills, A., 2011, "A review of available methods for seasonal storage of solar thermal energy in residential applications," Renewable and Sustainable Energy Reviews, 15(7), pp. 3341-3359.

[9] Zalba, B., Marín, J. M., Cabeza, L. F., and Mehling, H., 2003, "Review on thermal energy storage with phase change: materials, heat transfer analysis and applications," Applied Thermal Engineering, 23(3), pp. 251-283.

[10] Ibrahim, H., Ilinca, A., and Perron, J., 2008, "Energy storage systems—Characteristics and comparisons," Renewable and Sustainable Energy Reviews, 12(5), pp. 1221-1250.

[11] Mathur, A. K., and Kasetty, R. B., 2013, "Thermal energy storage system comprising optimal thermocline management," Google Patents.

[12] Lata, J., and Blanco, J., 2010, "Single tank thermal storage design for solar thermal power plants," Solar PACE, pp. 21-24.

[13] Agyenim, F., Hewitt, N., Eames, P., and Smyth, M., 2010, "A review of materials, heat transfer and phase change problem formulation for latent heat thermal energy storage systems (LHTESS)," Renewable and Sustainable Energy Reviews, 14(2), pp. 615-628.

[14] Verma, P., Varun, and Singal, S., 2008, "Review of mathematical modeling on latent heat thermal energy storage systems using phase-change material," Renewable and Sustainable Energy Reviews, 12(4), pp. 999-1031.

[15] Abhat, A., 1983, "Low temperature latent heat thermal energy storage: heat storage materials," Solar energy, 30(4), pp. 313-332.

[16] Arndt, P., Dunn, J., and Willix, R., 1984, "Organic compounds as candidate phase change materials in thermal energy storage," Thermochimica acta, 79, pp. 55-68.

[17] Gomez, J. C., 2011, "High-Temperature Phase Change Materials (PCM) Candidates for Thermal Energy Storage (TES) Applications," Contract, 303, pp. 275-3000.

[18] Kenisarin, M. M., 2010, "High-temperature phase change materials for thermal energy storage," Renewable and Sustainable Energy Reviews, 14(3), pp. 955-970.

[19] Steinmann, W.-D., Laing, D., and Tamme, R., 2010, "Latent Heat Storage Systems for Solar Thermal Power Plants and Process Heat Applications," Journal of Solar Energy Engineering, 132(2), p. 021003.

[20] Nithyanandam, K., and Pitchumani, R., 2014, "Optimization of an encapsulated phase change material thermal energy storage system," Solar Energy, 107(0), pp. 770-788.

[21] Jegadheeswaran, S., and Pohekar, S. D., 2009, "Performance enhancement in latent heat thermal storage system: a review," Renewable and Sustainable Energy Reviews, 13(9), pp. 2225-2244.

[22] Michels, H., and Pitz-Paal, R., 2007, "Cascaded latent heat storage for parabolic trough solar power plants," Solar Energy, 81(6), pp. 829-837.

[23] Stekli, J., Irwin, L., and Pitchumani, R., 2013, "Technical Challenges and Opportunities for Concentrating Solar Power With Thermal Energy Storage," Journal of Thermal Science and Engineering Applications, 5(2), p. 021011.

[24] Abedin, A. H., and Rosen, M. A., 2012, "Closed and open thermochemical energy storage: Energy- and exergy-based comparisons," Energy, 41(1), pp. 83-92.

[25] Abedin, A. H., and Rosen, M. A., 2011, "A Critical Review of Thermochemical Energy Storage Systems," The Open Renewable Energy Journal, 4, pp. 42-46.

[26] Lovegrove, K., Luzzi, A., Mccann, M., and Freitag, O., 1999, "Exergy analysis of ammonia-based solar thermochemical power systems," Solar energy, 66(2), pp. 103-115.

[27] Blair, N., Dobos, A. P., Freeman, J., Neises, T., Wagner, M., Ferguson, T., Gilman, P., and Janzou, S., 2014, "System Advisor Model, SAM 2014.1. 14: General Description," NREL Report No. TP-6A20-61019, National Renewable Energy Laboratory, Golden, CO.

[28] Laboratory, U. o. W.-.-M. S. E., and Klein, S. A., 1979, TRNSYS, a transient system simulation program, Solar Energy Laborataory, University of Wisconsin--Madison.

[29] Thermoflow, "THERMOFLEX: Simulation of combined cycles, cogeneration systems, and other thermal power systems."

[30] Wilding, W. V., Rowley, R. L., and Oscarson, J. L., 1998, "DIPPR® Project 801 evaluated process design data," Fluid phase equilibria, 150, pp. 413-420.

[31] Perrut, M., 2000, "Supercritical fluid applications: industrial developments and economic issues," Industrial & Engineering Chemistry Research, 39(12), pp. 4531-4535.

202

[32] Ganapathi, G. B., and Wirz, R., "High density thermal energy storage with supercritical fluids," Proc. ASME 2012 6th International Conference on Energy Sustainability collocated with the ASME 2012 10th International Conference on Fuel Cell Science, Engineering and Technology, American Society of Mechanical Engineers, pp. 699-707.

[33] van der Waals, J. D., 2004, On the continuity of the gaseous and liquid states, DoverPublications. com.

[34] Redlich, O., and Kwong, J., 1949, "On the Thermodynamics of Solutions. V. An Equation of State. Fugacities of Gaseous Solutions," Chemical Reviews, 44(1), pp. 233-244.

[35] Soave, G., 1972, "Equilibrium constants from a modified Redlich-Kwong equation of state," Chemical Engineering Science, 27(6), pp. 1197-1203.

[36] Peng, D.-Y., and Robinson, D. B., 1976, "A new two-constant equation of state," Industrial & Engineering Chemistry Fundamentals, 15(1), pp. 59-64.

[37] Pitzer, K., 1991, "Ion interaction approach: theory and data correlation," Activity coefficients in electrolyte solutions, 2, pp. 75-154.

[38] Lewis, G. N., "The law of physico-chemical change," Proc. Proceedings of the American Academy of Arts and Sciences, JSTOR, pp. 49-69.

[39] Sandler, S. I., 2006, Chemical, biochemical, and engineering thermodynamics, John Wiley & Sons Hoboken, NJ.

[40] Clark, P. D., and Dowling, N. I., 2004, "Capture of solar energy using elemental sulfur," Journal of Sulfur Chemistry, 25(1), pp. 7-11.

[41] Wirz, R. E., Stopin, A., Tse, L. A., Lavine, A. S., Kavehpour, H. P., Baghaei Lakeh, R., Furst, B., Bran-Anleu, G., and Garcia-Garibay, M. A., "High-Density, High-Temperature Thermal Energy Storage And Retrieval," Patent Application No. US 14/475479 , filed Sept 02, 2014.

[42] Vignarooban, K., Xu, X., Arvay, A., Hsu, K., and Kannan, A., 2015, "Heat transfer fluids for concentrating solar power systems–A review," Applied Energy, 146, pp. 383-396.

203

[43] Tse, L. A., Ganapathi, G. B., Wirz, R. E., and Lavine, A. S., 2013, "Spatial and temporal modling of super- and sub- critical thermal energy storage," Solar Energy Materials and Solar Cells.

[44] Poulis, J., Massen, C., and vd Leeden, P., 1962, "Magnetic susceptibility of liquid sulphur," Transactions of the Faraday Society, 58, pp. 474-479.

[45] Touro, F., and Wiewiorowski, T., 1966, "Viscosity—Chain Length Relationship in Molten Sulfur Systems," The Journal of Physical Chemistry, 70(1), pp. 239-241.

[46] Young, D. A., 1975, "Phase diagrams of the elements," No. UCRL--51902 United States10.2172/4010212Thu Mar 24 08:23:14 EDT 2011Dep. NTISLLNL; NSA-33-026618English.

[47] Meyer, B., 1976, "Elemental sulfur," Chemical Reviews, 76(3), pp. 367-388.

[48] Carden, P., 1977, "Energy corradiation using the reversible ammonia reaction," Solar Energy, 19(4), pp. 365-378.

[49] Chubb, T., 1975, "Analysis of gas dissociation solar thermal power system," Solar Energy, 17(2), pp. 129-136.

[50] Häfele, W., 1974, "Energy choices that Europe faces: a European view of energy," Science, 184(4134), pp. 360-367.

[51] Wyman, C., Castle, J., and Kreith, F., 1980, "A review of collector and energy storage technology for intermediate temperature applications," Solar Energy, 24(6), pp. 517-540.

[52] Wentworth, W., and Chen, E., 1976, "Simple thermal decomposition reactions for storage of solar thermal energy," Solar Energy, 18(3), pp. 205-214.

[53] Dowling, N., 1992, "Corrosion of materials used in storage and handling of solid elemental sulphur," Materials Performance: Sulphur and Energy, pp. 103-115.

[54] Nichita, D. V., Gomez, S., and Luna, E., 2002, "Multiphase equilibria calculation by direct minimization of Gibbs free energy with a global optimization method," Computers & chemical engineering, 26(12), pp. 1703-1724.

[55] Tuller, W. N., 1954, "The sulphur data book," The sulphur data book.

[56] Castier, M., Rasmussen, P., and Fredenslund, A., 1989, "Calculation of simultaneous chemical and phase equilibria in nonideal systems," Chemical Engineering Science, 44(2), pp. 237-248.

[57] Gautam, R., and Seider, W. D., 1979, "Computation of phase and chemical equilibrium: Part I. Local and constrained minima in Gibbs free energy," AIChE Journal, 25(6), pp. 991-999.

[58] George, B., Brown, L., Farmer, C., Buthod, P., and Manning, F., 1976, "Computation of multicomponent, multiphase equilibrium," Industrial & Engineering Chemistry Process Design and Development, 15(3), pp. 372-377.

[59] Gordon, S., and McBride, B. J., 1976, "Computer Program for Calculation of Complex Chemical Equilibrium Compositions, Rocket Performance, Incident and Reflected Shocks, and Chapman-Jouguet Detonations. Interim Revision, March 1976."

[60] Karpov, I. K., Chudnenko, K. V., Kulik, D. A., and Bychinskii, V. A., 2002, "The convex programming minimization of five thermodynamic potentials other than Gibbs energy in geochemical modeling," American Journal of Science, 302(4), pp. 281-311.

[61] ÍÑIGUEZ, J. C., "Helmholtz Free Energy Minimization for a Chemical Reaction."

[62] Stull, D. R., and Prophet, H., 1971, "JANAF thermochemical tables," DTIC Document.

[63] Rau, H., Kutty, T., and Guedes de Carvalho, J., 1973, "High temperature saturated vapour pressure of sulphur and the estimation of its critical quantities," The Journal of Chemical Thermodynamics, 5(2), pp. 291-302.

[64] Heidemann, R. A., Phoenix, A. V., Karan, K., and Behie, L. A., 2001, "A Chemical Equilibrium Equation of State Model for Elemental Sulfur and Sulfur-Containing Fluids," Industrial & Engineering Chemistry Research, 40(9), pp. 2160-2167.

[65] Karan, K., Heidemann, R. A., and Behie, L. A., 1998, "Sulfur solubility in sour gas: predictions with an equation of state model," Industrial & engineering chemistry research, 37(5), pp. 1679-1684.

[66] Shuai, X., and Meisen, A., 1995, "New correlations predict physical properties of elemental sulfur," Oil and Gas Journal, 93(42).

[67] West, E. D., 1959, "The Heat Capacity of Sulfur from 25 to 450°, the Heats and Temperatures of Transition and Fusion1,2," Journal of the American Chemical Society, 81(1), pp. 29-37.

[68] West, W. A., and Menzies, A., 1929, "The Vapor Pressures of Sulphur Between 100 and 550 with Related Thermal Data," The Journal of Physical Chemistry, 33(12), pp. 1880-1892.

[69] Lewis, G. N., and Randall, M., 1911, "THE HEAT CONTENT OF THE VARIOUS FORMS OF SULFUR," Journal of the American Chemical Society, 33(4), pp. 476-488.

[70] Linstrom, P. J., and Mallard, W., 2001, "NIST Chemistry webbook; NIST standard reference database No. 69."

[71] Lemmon, E. W., Huber, M. L., and McLinden, M. O., 2002, "NIST reference fluid thermodynamic and transport properties–REFPROP," Version.

[72] Klein, S., and Alvardo, F., 2009, "EES-Engineering equation solver: user's manual for microsoft windows operating systems, version 8.609," F-Chart Software, Madison, WI, USA.

[73] Odeh, S., Morrison, G., and Behnia, M., 1998, "Modelling of parabolic trough direct steam generation solar collectors," Solar energy, 62(6), pp. 395-406.

[74] Aceves-Saborio, S., Nakamura, H., and Reistad, G., 1994, "Optimum efficiencies and phase change temperatures in latent heat storage systems," Journal of Energy Resources Technology;(United States), 116(1).

[75] Rosen, M. A., 2001, "The exergy of stratified thermal energy storages," Solar energy, 71(3), pp. 173-185.

[76] Wagner, M. J., 2008, Simulation and predictive performance modeling of utility-scale central receiver system power plants, University of Wisconsin--Madison.

[77] Dyreby, J. J., 2014, "Modeling the Supercritical Carbon Dioxide Brayton Cycle with Recompression," THE UNIVERSITY OF WISCONSIN-MADISON.

[78] Seidel, W., 2011, "Model Development and Annual Simulation of the Supercritical Carbon Dioxide Brayton Cycle for Concentrating Solar Power Applications," University of Wisconsin--Madison.

[79] Kolb, G. J., 2011, "An evaluation of possible next-generation high-temperature molten-salt power towers," Albuquerque, NM: Sandia National Laboratories.

[80] Dudley, V. E., Kolb, G. J., Mahoney, A. R., Mancini, T. R., Matthews, C. W., Sloan, M., and Kearney, D., 1994, "Test results: SEGS LS-2 solar collector," Sandia National Labs., Albuquerque, NM (United States).

[81] Wilcox, S., and Marion, W., 2008, Users manual for TMY3 data sets, National Renewable Energy Laboratory Golden, CO.

[82] Zukauskas, A., 1987, "Heat transfer from tubes in cross-flow," advances in heat transfer, 18, p. 87.

[83] Dostal, V., 2004, "A supercritical carbon dioxide cycle for next generation nuclear reactors," Massachusetts Institute of Technology.

[84] Dostal, V., Hejzlar, P., and Driscoll, M. J., 2006, "The supercritical carbon dioxide power cycle: comparison to other advanced power cycles," Nuclear technology, 154(3), pp. 283-301.

[85] Chapman, D. J., and Arias, D. A., "An Assessment of the Supercritical Carbon Dioxide Cycle for Use in a Solar Parabolic Trough Power Plant," Proc. Proceedings of SCCO2 Power Cycle Symposium, RPI, Troy, NY, April, pp. 29-30.

[86] Ma, Z., and Turchi, C., "Advanced supercritical carbon dioxide power cycle configurations for use in concentrating solar power systems," Proc. Proceedings of Supercritical CO2 Power Cycle Symposium, pp. 24-25.

[87] Turchi, C. S., Ma, Z., and Dyreby, J., "Supercritical carbon dioxide power cycle configurations for use in concentrating solar power systems," Proc. ASME Turbo Expo 2012: Turbine Technical Conference and Exposition, American Society of Mechanical Engineers, pp. 967-973.

[88] Neises, T. W., Klein, S. A., and Reindl, D. T., 2012, "Development of a Thermal Model for Photovoltaic Modules and Analysis of NOCT Guidelines," Journal of Solar Energy Engineering, 134(1), p. 011009.

[89] Wagner, M. J., and Gilman, P., 2011, "Technical manual for the SAM physical trough model," Contract, 303, pp. 275-3000.

[90] Patnode, A. M., 2006, "Simulation and performance evaluation of parabolic trough solar power plants," University of Wisconsin.

[91] Lippke, F., 1995, "Simulation of the part-load behavior of a 30 MWe SEGS plant," Sandia National Labs., Albuquerque, NM (United States).

[92] Biencinto, M., Bayón, R., Rojas, E., and González, L., 2014, "Simulation and assessment of operation strategies for solar thermal power plants with a thermocline storage tank," Solar Energy, 103, pp. 456-472.

[93] Bjurström, H., and Carlsson, B., 1985, "An exergy analysis of sensible and latent heat storage," Journal of Heat Recovery Systems, 5(3), pp. 233-250.

[94] Domański, R., and Fellah, G., 1996, "Exergy analysis for the evaluation of a thermal storage system employing PCMs with different melting temperatures," Applied thermal engineering, 16(11), pp. 907-919.

[95] Domański, R., and Fellah, G., 1995, "Exergy as a tool for designing and operating thermal storage units," Biuletyn Instytutu Technik Cieplnej Politechniki Warszawskiej, 81, pp. 24-45.

[96] Erek, A., and Dincer, I., 2009, "A New Approach to Energy and Exergy Analyses of Latent Heat Storage Unit," Heat Transfer Engineering, 30(6), pp. 506-515.

[97] Jegadheeswaran, S., and Pohekar, S. D., 2010, "Exergy analysis of particle dispersed latent heat thermal storage system for solar water heaters," Journal of Renewable and Sustainable Energy, 2(2), p. 023105.

[98] Jegadheeswaran, S., Pohekar, S. D., and Kousksou, T., 2010, "Exergy based performance evaluation of latent heat thermal storage system: A review," Renewable and Sustainable Energy Reviews, 14(9), pp. 2580-2595.

208

[99] Koca, A., Oztop, H. F., Koyun, T., and Varol, Y., 2008, "Energy and exergy analysis of a latent heat storage system with phase change material for a solar collector," Renewable Energy, 33(4), pp. 567-574.

[100] Kousksou, T., Strub, F., Castainglasvignottes, J., Jamil, A., and Bedecarrats, J., 2007, "Second law analysis of latent thermal storage for solar system," Solar Energy Materials and Solar Cells, 91(14), pp. 1275-1281.

[101] Ramayya, A. V., and Ramesh, K., 1998, "Exergy analysis of latent heat storage systems with sensible heating and subcooling of PCM," International journal of energy research, 22(5), pp. 411-426.

[102] Shabgard, H., Robak, C. W., Bergman, T. L., and Faghri, A., 2012, "Heat transfer and exergy analysis of cascaded latent heat storage with gravity-assisted heat pipes for concentrating solar power applications," Solar Energy, 86(3), pp. 816-830.

[103] Mawire, A., McPherson, M., and Vandenheetkamp, R., 2008, "Simulated energy and exergy analyses of the charging of an oil–pebble bed thermal energy storage system for a solar cooker," Solar Energy Materials and Solar Cells, 92(12), pp. 1668-1676.

[104] Rosen, M., Hooper, F., and Barbaris, L., 1988, "Exergy analysis for the evaluation of the performance of closed thermal energy storage systems," J. Sol. Energy Eng.;(United States), 110(4).

[105] Dincer, I., 2002, "Technical, environmental and exergetic aspects of hydrogen energy systems," International Journal of Hydrogen Energy, 27(3), pp. 265-285.

[106] Kreetz, H., and Lovegrove, K., 2002, "Exergy analysis of an ammonia synthesis reactor in a solar thermochemical power system," Solar energy, 73(3), pp. 187-194.

[107] Gunerhan, H., and Hepbasli, A., 2007, "Exergetic modeling and performance evaluation of solar water heating systems for building applications," Energy and Buildings, 39(5), pp. 509-516.

[108] Gupta, M. K., and Kaushik, S. C., 2008, "Exergetic performance evaluation and parametric studies of solar air heater," Energy, 33(11), pp. 1691-1702.

209

[109] Hepbasli, A., and Akdemir, O., 2004, "Energy and exergy analysis of a ground source (geothermal) heat pump system," Energy Conversion and Management, 45(5), pp. 737-753.

[110] Xiaowu, W., and Ben, H., 2005, "Exergy analysis of domestic-scale solar water heaters," Renewable and Sustainable Energy Reviews, 9(6), pp. 638-645.

[111] Rosen, M. A., 1992, "Appropriate thermodynamic performance measures for closed systems for thermal energy storage," ASME Journal of Solar Energy Engineering, 114, pp. 100-105.

[112] Rosen, M. A., and Dincer, I., 2003, "Exergy methods for assessing and comparing thermal storage systems," International Journal of Energy Research, 27(4), pp. 415-430.

[113] Bejan, A., 2002, "Fundamentals of exergy analysis, entropy generation minimization, and the generation of flow architecture," International Journal of Energy Research, 26(7), pp. 0-43.

[114] Gunnewiek, L., Nguyen, S., and Rosen, M., 1993, "Evaluation of the optimum discharge period for closed thermal energy storages using energy and exergy analyses," Solar energy, 51(1), pp. 39-43.

[115] Krane, R. J., 1987, "A second law analysis of the optimum design and operation of thermal energy storage systems," International Journal of Heat and Mass Transfer, 30(1), pp. 43-57.

[116] Kern, D. Q., 1950, Process heat transfer, Tata McGraw-Hill Education.

[117] Bell, K. J., 1988, "Delaware method for shell-side design," Heat Transfer Equipment Design, Hemisphere Publishing, New York, p. 145.

[118] Hewitt, G. F., 1998, "Heat exchanger design handbook," Begelle House Inc., New York.

[119] Incropera, F. P., Lavine, A. S., and DeWitt, D. P., 2011, Fundamentals of heat and mass transfer, John Wiley & Sons Incorporated.

[120] Bejan, A., 1978, "General criterion for rating heat-exchanger performance," International Journal of Heat and Mass Transfer, 21(5), pp. 655-658.

[121] Moran, M. J., Shapiro, H. N., Boettner, D. D., and Bailey, M., 2010, Fundamentals of engineering thermodynamics, Wiley. com.

[122] Rosen, M., Hooper, F., and Barbaris, L., "Efficiency Definitions for Closed Thermal Energy Storages," Proc. Proceedings of Jigastock: International Conference on Applied Geothermal Energy and Thermal Energy Storage, pp. 18-21.

[123] Watanabe, T., and Kanzawa, A., 1995, "Second law optimization of a latent heat storage system with PCMS having different melting points," Heat Recovery Systems and CHP, 15(7), pp. 641-653.

[124] Kaygusuz, K., and Ayhan, T., 1993, "Exergy analysis of solar-assisted heat-pump systems for domestic heating," Energy, 18(10), pp. 1077-1085.

[125] Öztürk, H. H., 2005, "Experimental evaluation of energy and exergy efficiency of a seasonal latent heat storage system for greenhouse heating," Energy Conversion and Management, 46(9), pp. 1523-1542.

[126] Gong, Z.-X., and Mujumdar, A. S., 1997, "Thermodynamic optimization of the thermal process in energy storage using multiple phase change materials," Applied Thermal Engineering, 17(11), pp. 1067-1083.

[127] Demirel, Y., and Öztürk, H. H., 2006, "Thermoeconomics of seasonal latent heat storage system," International journal of energy research, 30(12), pp. 1001-1012.

[128] Kaygusuz, A. S., Kamil, 2000, "Energy and exergy calculations of latent heat energy storage systems," Energy sources, 22(2), pp. 117-126.

[129] Sari, A., and Kaygusuz, K., 2004, "First and second laws analyses of a closed latent heat thermal energy storage system," Chinese Journal of Chemical Engineering, 12(2), pp. 290-293.

[130] El-Dessouky, H., and Al-Juwayhel, F., 1997, "Effectiveness of a thermal energy storage system using phase-change materials," Energy conversion and management, 38(6), pp. 601-617.

[131] Erek, A., and Dincer, I., 2008, "An approach to entropy analysis of a latent heat storage module," International Journal of Thermal Sciences, 47(8), pp. 1077-1085.

[132] Bejan, A., 1977, "Concept of irreversibility in heat exchanger design: Counterflow heat exchangers for gas-to-gas applications," J. Heat Transfer;(United States), 99(3).

[133] Turchi, C. S., Ma, Z., Neises, T. W., and Wagner, M. J., 2013, "Thermodynamic study of advanced supercritical carbon dioxide power cycles for concentrating solar power systems," Journal of Solar Energy Engineering, 135(4), p. 041007.

[134] Jorgenson, J., Denholm, P., and Mehos, M., "Quantifying the Value of Concentrating Solar Power in a Production Cost Model," Proc. ASME 2014 8th International Conference on Energy Sustainability collocated with the ASME 2014 12th International Conference on Fuel Cell Science, Engineering and Technology, American Society of Mechanical Engineers, pp. V001T002A007-V001T002A007.

[135] Forristall, R. E., 2003, Heat transfer analysis and modeling of a parabolic trough solar receiver implemented in engineering equation solver, National Renewable Energy Laboratory.

[136] Newbery, D., 2004, "Issues and options for restructuring electricity supply industries."

[137] Price, H., "A parabolic trough solar power plant simulation model," Proc. ASME 2003 International Solar Energy Conference, American Society of Mechanical Engineers, pp. 665-673.

[138] Bejan, A., 1980, "Second law analysis in heat transfer," Energy, 5(8), pp. 720-732.

[139] Bejan, A., 1978, "Two thermodynamic optima in the design of sensible heat units for energy storage," ASME Transactions Journal of Heat Transfer, 100, pp. 708-712.

[140] Bejan, A., 1988, "Advanced engineering thermodynamics."

[141] Domański, R., and Fellah, G., 1998, "Thermoeconomic analysis of sensible heat, thermal energy storage systems," Applied thermal engineering, 18(8), pp. 693-704.

[142] Dincer, I., Dost, S., and Li, X., 1997, "Performance analyses of sensible heat storage systems for thermal applications," International Journal of Energy Research, 21(12), pp. 1157-1171.

[143] Erek, A., and Akif Ezan, M., 2007, "Experimental and numerical study on charging processes of an ice-on-coil thermal energy storage system," International journal of energy research, 31(2), pp. 158-176.

212

[144] Smith, W. R., and Missen, R. W., 1982, Chemical reaction equilibrium analysis: theory and algorithms, Wiley New York.

[145] Madaeni, S. H., Sioshansi, R., and Denholm, P., 2012, "How thermal energy storage enhances the economic viability of concentrating solar power," Proceedings of the IEEE, 100(2), pp. 335-347.

[146] Flueckiger, S. M., Iverson, B. D., and Garimella, S. V., 2014, "Economic Optimization of a Concentrating Solar Power Plant With Molten-Salt Thermocline Storage," Journal of Solar Energy Engineering, 136(1), p. 011015.

[147] Tse, L. A., Ganapathi, G. B., Wirz, R. E., and Lavine, A. S., 2014, "Spatial and temporal modeling of sub- and supercritical thermal energy storage," Solar Energy, 103(0), pp. 402-410.

[148] Libby, C., Golden, J., Bedilion, R., and Turchi, C., 2014, "Assessment of Direct Steam Generation Technologies for Solar Thermal Augmented Steam Cycle Applications," Energy Procedia, 49, pp. 1420-1428.

[149] Garg, P., Kumar, P., and Srinivasan, K., 2013, "Supercritical carbon dioxide Brayton cycle for concentrated solar power," The Journal of Supercritical Fluids, 76, pp. 54-60.

[150] Cabello, J., Cejudo, J., Luque, M., Ruiz, F., Deb, K., and Tewari, R., 2011, "Optimization of the size of a solar thermal electricity plant by means of genetic algorithms," Renewable Energy, 36(11), pp. 3146-3153.

[151] Chow, T., Zhang, G., Lin, Z., and Song, C., 2002, "Global optimization of absorption chiller system by genetic algorithm and neural network," Energy and buildings, 34(1), pp. 103-109.

[152] SunShot, U. S. D. o. E., 2012, "SunShot Vision Study," Presentation.

[153] International Renewable Energy Agency, "Renewable Power Generation Costs in 2014."

[154] Rosen, M., 1992, "Appropriate thermodynamic performance measures for closed systems for thermal energy storage," Journal of solar energy engineering, 114(2), pp. 100-105.

[155] Ma, Z., Glatzmaier, G. C., Wagner, M., and Neises, T., "General Performance Metrics and Applications to Evaluate Various Thermal Energy Storage Technologies," Proc. ASME 2012 6th
213

International Conference on Energy Sustainability collocated with the ASME 2012 10th International Conference on Fuel Cell Science, Engineering and Technology, American Society of Mechanical Engineers, pp. 345-351.

[156] Casati, E., Casella, F., and Colonna, P., 2015, "Design of CSP plants with optimally operated thermal storage," Solar Energy, 116(0), pp. 371-387.

[157] Hummon, M., Denholm, P., Jorgenson, J., Palchak, D., Kirby, B., and Ma, O., 2013, "Fundamental Drivers of the Cost and Price of Operating Reserves," NREL, Golden, CO.

[158] Burkhardt III, J. J., Heath, G. A., and Turchi, C. S., 2011, "Life cycle assessment of a parabolic trough concentrating solar power plant and the impacts of key design alternatives," Environmental science & technology, 45(6), pp. 2457-2464.

[159] Cohen, G. E., Kearney, D. W., and Kolb, G. J., 1999, "Final report on the operation and maintenance improvement program for concentrating solar power plants," Usage listed is raw water usage and assumed to be withdrawal rate. Consumption rate approximated from, 90, pp. 30-31.

[160] Allani, Y., Favrat, D., and Von Spakovsky, M., 1997, "CO 2 mitigation through the use of hybrid solar-combined cycles," Energy conversion and management, 38, pp. S661-S667.

[161] Turchi, C., 2010, "Parabolic trough reference plant for cost modeling with the solar advisor model (SAM)," National Renewable Energy Laboratory (NREL), Golden, CO.

[162] "Price quotes for elemental sulfur," www.alibaba.com.

[163] Chao, J., Hall, K. R., Marsh, K. N., and Wilhoit, R. C., 1986, "Thermodynamic properties of key organic oxygen compounds in the carbon range C1 to C4. Part 2. Ideal gas properties," Journal of physical and chemical reference data, 15(4), pp. 1369-1436.

[164] Barrow, G. M., and McClellan, A., 1951, "The thermodynamic properties of naphthalene," Journal of the American Chemical Society, 73(2), pp. 573-575.

[165] Gazzo, A., Kost, C., and Ragwitz, M., 2011, "Middle East and North Africa Region Assessment of the Local Manufacturing Potential for Concentrated Solar Power (CSP) Projects," The World Bank.

214

[166] Zhu, G., Wendelin, T., Wagner, M. J., and Kutscher, C., 2014, "History, current state, and future of linear Fresnel concentrating solar collectors," Solar Energy, 103, pp. 639-652.

[167] Neises, T., and Turchi, C., 2014, "A comparison of supercritical carbon dioxide power cycle configurations with an emphasis on CSP applications," Energy Procedia, 49, pp. 1187-1196.

[168] Sioshansi, R., and Denholm, P., 2010, "The value of concentrating solar power and thermal energy storage," Sustainable Energy, IEEE Transactions on, 1(3), pp. 173-183.

[169] Sioshansi, R., Denholm, P., Jenkin, T., and Weiss, J., 2009, "Estimating the value of electricity storage in PJM: Arbitrage and some welfare effects," Energy economics, 31(2), pp. 269-277.

[170] Denholm, P., and Mehos, M., 2011, "Enabling greater penetration of solar power via the use of CSP with thermal energy storage," Contract, 303, pp. 275-3000.

[171] Mills, A., 2013, "Changes in the economic value of variable generation at high penetration levels: A pilot case study of California."

[172] Mills, A. D., "An evaluation of solar valuation methods used in utility planning and procurement processes," Proc. American Solar Energy Society (ASES) Annual Meeting, Baltimore, MD, April 16-20, 2013.

[173] Cole, W. J., Powell, K. M., and Edgar, T. F., 2012, "Optimization and advanced control of thermal energy storage systems," Reviews in Chemical Engineering, 28(2-3).

[174] Camacho, E. F., Berenguel, M., Alvarado, I., Limon, D., and de los Descubrimientos, C., "Control of solar power systems: a survey," Proc. Proc. of the 9th Int. Symp. on Dynamics and Control of Process Systems, DYCOPS.

[175] Powell, K. M., and Edgar, T. F., 2012, "Modeling and control of a solar thermal power plant with thermal energy storage," Chemical Engineering Science, 71, pp. 138-145.

[176] Rolfsman, B., 2004, "Combined heat-and-power plants and district heating in a deregulated electricity market," Applied energy, 78(1), pp. 37-52.

[177] Tse, L. A., Lakeh, R. B., Wirz, R. E., and Lavine, A. S., "Exergy-Based Optimization of Sub- and Supercritical Thermal Energy Storage Systems," Proc. ASME 2014 8th International Conference on Energy Sustainability collocated with the ASME 2014 12th International Conference on Fuel Cell Science, Engineering and Technology, American Society of Mechanical Engineers, pp. V002T012A001-V002T012A001.

[178] Tse, L., Ganapathi, G., Wirz, R., and Lavine, A., "System Modeling for a Supercritical Thermal Energy Storage System," Proc. ASME 2012 6th International Conference on Energy Sustainability collocated with the ASME 2012 10th International Conference on Fuel Cell Science, Engineering and Technology, American Society of Mechanical Engineers, pp. 691-698.

[179] Herrmann, U., Kelly, B., and Price, H., 2004, "Two-tank molten salt storage for parabolic trough solar power plants," Energy, 29(5-6), pp. 883-893.

[180] Kolb, G. J., 2011, "Evaluation of annual performance of 2-tank and thermocline thermal storage systems for trough plants," Journal of solar energy engineering, 133(3).

[181] Bergman, T. L., Lavine, A. S., Incropera, F. P., and DeWitt, D. P., 2011, Fundamentals of Heat and Mass Transfer, John Wiley & Sons Incorporated.

[182] Kolb, G. J., 2011, "Evaluation of annual performance of 2-tank and thermocline thermal storage systems for trough plants," Journal of Solar Energy Engineering, 133(3), p. 031023.

[183] Montes, M., Abánades, A., Martinez-Val, J., and Valdés, M., 2009, "Solar multiple optimization for a solar-only thermal power plant, using oil as heat transfer fluid in the parabolic trough collectors," Solar Energy, 83(12), pp. 2165-2176.

[184] Stoddard, L., Abiecunas, J., and O'Connell, R., 2006, Economic, energy, and environmental benefits of concentrating solar power in California, National Renewable Energy Laboratory.

[185] Camacho, E., Rubio, F., Berenguel, M., and Valenzuela, L., 2007, "A survey on control schemes for distributed solar collector fields. Part II: Advanced control approaches," Solar Energy, 81(10), pp. 1252-1272.

[186] Rubio, F. R., Berenguel, M., and Camacho, E. F., 1995, "Fuzzy logic control of a solar power plant," Fuzzy Systems, IEEE Transactions on, 3(4), pp. 459-468.

216

[187] Menéndez, R. P., Martínez, J. Á., Prieto, M. J., Barcia, L. Á., and Sánchez, J. M. M., 2014, "A Novel Modeling of Molten-Salt Heat Storage Systems in Thermal Solar Power Plants," Energies, 7(10), pp. 6721-6740.

[188] Bruno, S., Lamonaca, S., La Scala, M., and Stecchi, U., "Optimal Design of Trigeneration and District Energy in the Presence of Energy Storage," Proc. International Conference on Renewable Energies and Power Quality (ICREPQ'10), Granada (Spain), 23th to 25th March.

[189] Piacentino, A., and Cardona, F., 2008, "An original multi-objective criterion for the design of small-scale polygeneration systems based on realistic operating conditions," Applied Thermal Engineering, 28(17), pp. 2391-2404.

[190] Madaeni, S. H., Sioshansi, R., and Denholm, P., 2013, "Estimating the capacity value of concentrating solar power plants with thermal energy storage: A case study of the southwestern United States," Power Systems, IEEE Transactions on, 28(2), pp. 1205-1215.

217